

# POLITECNICO DI TORINO

Master's Degree in Electronic Engineering



**Politecnico  
di Torino**

Master's Degree Thesis

## Optimization strategies for metasurface antenna design

**Advisor**

Prof. Giuseppe Vecchi

**Co-advisors**

Dott. Marcello Zucchi

Dott. Giorgio Giordanengo

**Candidate**

Amedeo Guida

301098

ACADEMIC YEAR 2022-2023

# Abstract

The automated design of metasurface (MTS) antennas has been a subject of extensive research, encompassing both theoretical and practical aspects. The inherent complexity of these antennas, made by sub-wavelength scattering elements organized in a periodic lattice over large areas, has forced researchers to devise more efficient methods for addressing this challenge. Recent strategies have shifted towards fully numerical modelling, with solutions attained through either direct methods or optimization algorithms. Among the latter, recently the current-based approach has emerged as a promising avenue for tackling the design of large antennas. Nonetheless, like all non-linear and non-convex optimization problems, it encounters common issues such as slow convergence and the occurrence of local minima. In this work, a novel adaptive weighting scheme for the current-based optimization of MTS antennas is proposed. The design of MTS antennas is a multi-objective optimization problem, i.e., a set of constraints must be concurrently met, including passivity, losslessness, pattern masks, and more. In order to reduce its numerical complexity, the problem is formulated as a single objective minimization with the weighted sum method. The weights assigned to each objective function reflect the relative significance of specific objectives, nonetheless, it is generally a complex task to definitively determine the hierarchy of importance. It is possible to demonstrate that an a priori choice of a set of weights leads to suboptimal solutions or to the convergence to a local minimum. Therefore, a scheme capable of adaptively modifying the weights of individual objective functions is valuable for exploring the Pareto front. The algorithm proposed in this work is based on the geometrical interpretation of the weights: anchor points can be identified on the Pareto front, then, a hyperplane is constructed from these points. The components of the normal unit vector to the hyperplane, which points in the direction of the knee point, can be used as weights for the objective function. To assess the performance of the proposed algorithm, its results have been compared to those achieved by a conventional minimization algorithm performed over an equal number of iterations for various antenna size and pattern masks. The proposed solution is able to achieve satisfactory results within a limited number of iterations, whereas the conventional solution is still far from convergence. In conclusion, the algorithm

proposed in this study allows the design process to be freed from the selection of an accurate initial set of weights. Moreover, the numerical results demonstrate an enhancement in the achieved performance and an increase in the convergence speed compared to standard algorithms.

# Table of Contents

<b>List of Tables</b>	v
<b>List of Figures</b>	vi
<b>1 Introduction</b>	1
1.1 Metasurface antennas . . . . .	1
1.2 Aim of the thesis . . . . .	3
1.3 Thesis outline . . . . .	4
<b>2 Electromagnetic formulation</b>	6
2.1 EM radiation from sources . . . . .	6
2.1.1 Auxiliary potentials method . . . . .	6
2.1.2 Solution with the Green's function . . . . .	7
2.2 Scattering formulation . . . . .	9
2.2.1 Boundary conditions . . . . .	9
2.2.2 Equivalence theorem . . . . .	10
2.3 Method of moments . . . . .	12
<b>3 Current-based optimization algorithm</b>	16
3.1 Electromagnetic problem formulation . . . . .	16
3.2 Constraints definition . . . . .	18
3.3 Algorithm formulation . . . . .	20
<b>4 Optimization strategies</b>	26
4.1 Slack variables . . . . .	26
4.1.1 Objective function formulation . . . . .	27
4.1.2 Gradient and linesearch . . . . .	28
4.1.3 Convergence . . . . .	29
4.2 Multi-objective optimization problem: the weighted sum method . .	30
4.3 Meaning of the weights . . . . .	33
4.4 Adaptive weight scheme . . . . .	35

4.4.1	Concept of hyperplane . . . . .	36
4.4.2	Algorithm formulation . . . . .	37
4.4.3	Example . . . . .	40
4.5	Hyperplane Adaptive Weighting scheme . . . . .	42
<b>5</b>	<b>Numerical results</b>	<b>46</b>
5.1	Optimization setup . . . . .	46
5.2	Medium sized antenna . . . . .	47
5.2.1	Circular polarization . . . . .	48
5.2.2	Linear polarization . . . . .	53
5.2.3	Full-wave solution . . . . .	54
5.3	Large sized antenna . . . . .	55
5.3.1	Circular polarization . . . . .	56
5.3.2	Linear polarization . . . . .	57
5.3.3	Full-wave solution . . . . .	59
5.4	Small sized antenna . . . . .	60
5.4.1	Circular polarization . . . . .	60
5.4.2	Linear polarization . . . . .	61
5.4.3	Full-wave solution . . . . .	62
5.5	Medium sized, squinted beam . . . . .	64
<b>6</b>	<b>Conclusions</b>	<b>66</b>
<b>A</b>	<b>Antenna generalities</b>	<b>68</b>
A.1	Field polarization . . . . .	68
A.2	Directivity, gain and efficiency . . . . .	70
<b>B</b>	<b>Source field for circular metasurface</b>	<b>72</b>
<b>C</b>	<b>Linear and non-linear conjugate gradient algorithms</b>	<b>76</b>
	<b>Bibliography</b>	<b>81</b>

# List of Tables

3.1	Summary of all possible combinations of $\mathbf{J}$ and $\mathbf{E}$ . . . . .	25
5.1	Design parameters for a medium sized antenna with pencil beam radiation pattern. . . . .	48
5.2	$10\lambda_0$ - pencil beam - circular polarization: functionals values during the optimization performed with 4 weight updates. . . . .	49
5.3	$10\lambda_0$ - pencil beam - circular polarization: assigned weights during the optimization performed with 4 weight updates. . . . .	49
5.4	Design parameters for a large sized antenna with pencil beam radiation pattern. . . . .	56
5.5	Design parameters for a small sized antenna with pencil beam radiation pattern. . . . .	60
5.6	Design parameters for a medium sized antenna with squinted beam radiation pattern. . . . .	64

# List of Figures

1.1	Different technologies for MTS realization: (a) metallic square patches with variable size , (b) circular patches with variable radius, (c) metal pillars with variable height, (d) circular slots with variable radius. . . . .	2
1.2	Realization of a $20\lambda$ -diameter antenna: (a) overall struture ( <i>macroscale</i> ), (b) periodic pattern ( <i>mesoscale</i> ), (c) scattering elements ( <i>microscale</i> ). . . . .	3
1.3	(a) Actual metasurface and (b) homogenized metasurface with the surface impedance distribution. . . . .	3
2.1	Surface equivalence theorem illustration: (a) actual and (b) equivalent problem. . . . .	11
2.2	Surface equivalence theorem in presence of an actual obstacle: (a) actual and (b) equivalent problems. . . . .	13
2.3	Graphical representation of RWG basis function. . . . .	15
3.1	Graphical application of the Equivalence theorem. The dashed line represents the volume containing the sources. . . . .	17
3.2	Graphical representation of the radiated field masks: $M_0$ and $F_{ref}$ are respectively the objective level and the reference level for the main lobe. Relative levels for cross-pol and side lobes are represented by vertical arrows. . . . .	20
3.3	Triangular mesh of a $10\lambda_0$ diameter circular metasurface antenna. The hole in the centre has a $\lambda_0/2$ diameter and hosts the feed. . . . .	21
3.4	Comparison between (a) ramp function and (b) squared ramp function. . . . .	23
4.1	Convergence plot of the optimization performed over 200 iterations: optimization function expressed with ramp function versus slack variables. . . . .	30
4.2	Mapping between the decision space ( $\mathbb{R}^3$ ) and objective space ( $\mathbb{R}^2$ ). . . . .	31
4.3	[15] Representation of the Pareto front (blue line), optimal (red dots) and non-optimal (black dots) solutions. . . . .	32

4.4	Graphical interpretation of the weights in a $2d$ -space: black solid line are the $U$ -function contour tangent to the Pareto front (red dashed curve). The direction of decreasing $U$ pointed by the arrow is dictated by the weights. . . . .	35
4.5	The knee point on the Pareto front (blue dots) minimizes the distance from the utopia point. . . . .	35
4.6	Hyperplane in 2-dimensional space constructed from two anchor points (previous solutions): the normal unit vector to the hyperplane points towards the knee point (new solution). . . . .	37
4.7	Graphical representation of the HAW algorithm: sky-blue dots represent the Pareto front while the direction of the blue arrow is dictated by the weights computed using (4.37-4.38). . . . .	41
4.8	Pareto front in 2-dimensional space (solid line): dashed lines separate convex from non convex parts. . . . .	44
5.1	Starting current for circular MTS antennas: magnitude and direction.	47
5.2	$10\lambda_0$ - pencil beam - circular polarization: optimized surface current using (a) NLCG and (b) NLCG-HAW. . . . .	50
5.3	$10\lambda_0$ - pencil beam - circular polarization: regularized surface impedance distribution using (a) NLCG and (b) NLCG-HAW. . . . .	50
5.4	$10\lambda_0$ - pencil beam - circular polarization: co- and cross- pol., cut for $\phi = 0$ . (a) NLCG result, (b) NLCG-HAW result. . . . .	51
5.5	$10\lambda_0$ - pencil beam - circular polarization: co- and cross- pol., cut for $\phi = 90$ . (a) NLCG result, (b) NLCG-HAW result. . . . .	51
5.6	$d = 10\lambda_0$ - pencil beam - circular polarized field - NLCG only: (a) optimized surface current and (b) regularized surface impedance distribution. . . . .	52
5.7	$d = 10\lambda_0$ - pencil beam - circular polarized field - NLCG only: co- and cross-pol., (a) cut for $\phi = 0$ and (b) $\phi = 90$ . . . . .	52
5.8	$d = 10\lambda_0$ - pencil beam - linear polarized field: (a) optimized surface current and (b) regularized surface impedance distribution. . . . .	53
5.9	$d = 10\lambda_0$ . Pencil beam - linear polarized field: co- and cross-polarization. Cut for (a) $\phi = 0^\circ$ and (b) $\phi = 90^\circ$ . . . . .	54
5.10	$d = 10\lambda_0$ - pencil beam - circular polarized field: (a) unit cells and (b) current distribution over unit cells. . . . .	55
5.11	$d = 10\lambda_0$ - pencil beam - circular polarized field: co- and cross-polarization. Cut for $\phi = 0$ , comparison between the optimized radiated pattern and the realized one. . . . .	55
5.12	$d = 20\lambda_0$ . Pencil beam - circular polarized field: (a) optimized surface current and (b) regularized surface impedance distribution. . . . .	57

5.13	$d = 20\lambda_0$ . Pencil beam - circular polarized field. Cuts for (a) $\phi = 0^\circ$ and (b) $\phi = 90^\circ$ . . . . .	57
5.14	$d = 20\lambda_0$ . Pencil beam - linear polarized field: (a) optimized surface current and (b) impedance after regularization. . . . .	58
5.15	$d = 20\lambda_0$ . Pencil beam - linear polarized field: co- and cross-polarization. Cuts for (a) $\phi = 0^\circ$ and (b) $\phi = 90^\circ$ . . . . .	58
5.16	$d = 20\lambda_0$ - pencil beam - circular polarization: (a) unit cells and (b) current distribution over unit cells. . . . .	59
5.17	$d = 20\lambda_0$ - pencil beam - linear polarization: co- and cross- polarization. Cut for $\phi = 0$ , comparison between the optimized radiated pattern and the realized one. . . . .	59
5.18	$d = 6\lambda_0$ . Pencil beam - circular polarized field: (a) optimized surface current and (b) regularized surface impedance distribution. . . . .	61
5.19	$d = 6\lambda_0$ . Pencil beam - circular polarized field: co- and cross-polarization. Cuts for (a) $\phi = 0^\circ$ and (b) $\phi = 90^\circ$ . . . . .	61
5.20	$d = 6\lambda_0$ . Pencil beam - linear polarized field: (a) optimized surface current and (b) regularized surface impedance distribution. . . . .	62
5.21	$d = 6\lambda_0$ . Pencil beam - linear polarized field: co- and cross- polarization. Cuts for (a) $\phi = 0^\circ$ and (b) $\phi = 90^\circ$ . . . . .	62
5.22	$d = 6\lambda_0$ - pencil beam - circular polarized field: (a) unit cells and (b) current distribution over unit cells. . . . .	63
5.23	$d = 6\lambda_0$ - pencil beam - circular polarized field: co- and cross-polarization. Cuts for $\phi = 0$ , comparison between the optimized radiated pattern and the realized one. . . . .	63
5.24	$d = 12\lambda_0$ . Squinted beam - circular polarized field: (a) optimized surface current and (b) regularized surface impedance distribution. . . . .	65
5.25	$d = 12\lambda_0$ . Squinted beam - circular polarized field: (a) directivity in the plane cut $\phi = 0$ and (b) top view of the pattern in the $u - v$ plane. . . . .	65
B.1	Slab geometry. . . . .	72



# Chapter 1

## Introduction

### 1.1 Metasurface antennas

Nearly the totality of applications related to radar surveillance, satellite communications and the construction of radio telescopes rely on the use of systems based on high-directive antennas. In general, high-directive antennas designed for microwave or millimetre-wave applications employ reflectors to manipulate the radiated field based on their geometric properties. However, this conventional method often leads to the creation of bulky and expensive structures, as their performance are basically related on the size of the reflector. An alternative to reflector antennas is represented by phased arrays, which enable the design of high-gain antennas and, among other advantages, including being low-profile, allow for electronically steering the main lobe towards virtually any directions [1]. Unfortunately, phased arrays, aside from being an inherently expensive solution, require the presence of a feeding network, which not only complicates the design, but also makes the entire structure energy-intensive and affected by losses. Recently, scientific progress concerning metasurfaces has established a new frontier for antenna design, as they promise to be used for the construction of low-losses, low-cost, low-profile and high-directive radiating systems.

Metasurfaces (MTS) are artificial surfaces composed of a lattice, typically periodic, of sub-wavelength scattering elements placed on a dielectric supporting layer: they can be engineered as desired to achieve electromagnetic properties not found in nature. In particular, metasurfaces-based antennas, more commonly known as metasurface antennas, - in presence of an incident field - allow for the generation of a radiated field with desired characteristics by controlling the sub-wavelength pattern in dimension and shape. Although the most popular MTS antennas are made by printed conductive patches, they can be realized employing

several technologies (see Figure 1.1 for some examples). Moreover, MTS can be single layer or multi layer depending on the application and can be further categorized in terms of incident field, which can be embedded in the MTS (e.g. using a vertical dipole) and the resulting surface wave confined in the dielectric excites the scattering elements or can be an external field illuminating the MTS.

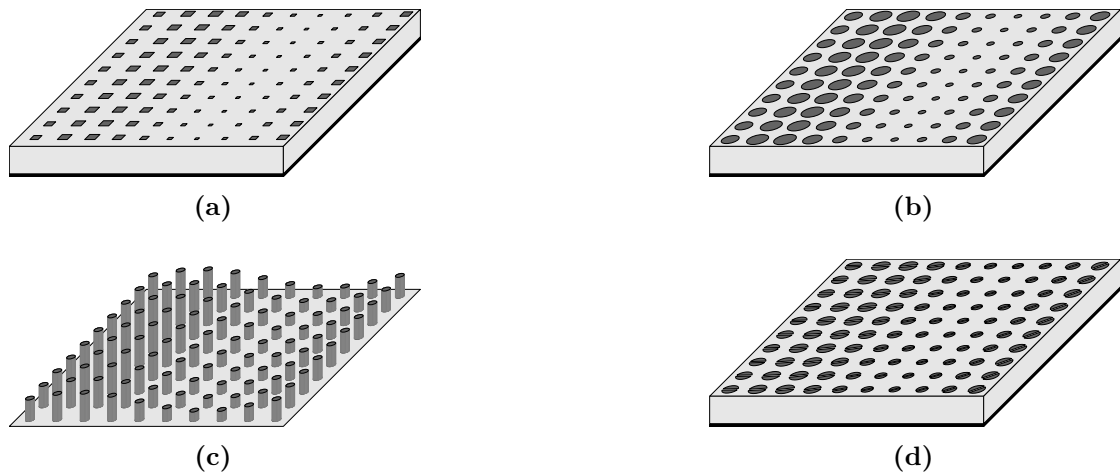


**Figure 1.1:** Different technologies for MTS realization: (a) metallic square patches with variable size, (b) circular patches with variable radius, (c) metal pillars with variable height, (d) circular slots with variable radius.

The analysis of such kind of structures is usually carried out with full-wave solvers. A generic full-wave solver solves the Maxwell's equations with the *natural* boundary conditions, i.e. vanishing tangential electric field on a perfect electric conductor, field continuity at material interfaces and radiation condition at infinity. The synthesis of a MTS antenna using the full-wave approach is unfeasible due to the inherent multiscale nature of the problem. Indeed, considering the square patch realization of a MTS antenna in Figure 1.2, the scattering elements are placed over a large area ( $\gg \lambda$ ), so one can talk about *macroscale*, the periodicity of the pattern is proportional to the wavelength ( $\sim \lambda$ ), i.e. *mesoscale*, while patches and their details are smaller compared to the wavelength ( $\ll \lambda$ ), i.e. *microscale*. This aspect forces the research towards different approaches to deal with the large computational effort of the problem and with its geometrical complexity.

In the last 20 years, the analysis of MTS has been revolutionized thanks to the introduction of the *surface impedance distribution*, which can be used to describe the electromagnetic behaviour of MTSs from a macroscopic standpoint. This parameter derives from an appropriate boundary condition [2], which relates the average tangential electric field to the jump of the tangential magnetic field over

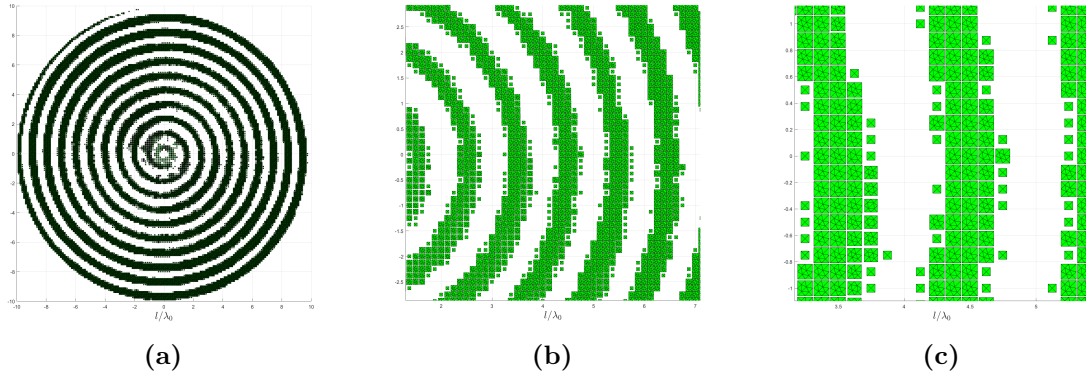


**Figure 1.2:** Realization of a  $20\lambda$ -diameter antenna: (a) overall structure (*macroscale*), (b) periodic pattern (*mesoscale*), (c) scattering elements (*microscale*).

the surface allowing for the homogenization of the MTS (see Figure 1.3). This approach not only allows for the analysis of the MTS, but also enables a more efficient design, as the number of unknowns is by far reduced. Indeed, recently developed MTS antenna design procedures consist in two distinct stages: the first one aims to derive the sought impedance distribution which complies with the desired specifications and then the profile can be synthesized using unit cells (e.g. Figure 1.2). Certainly, the very final step of the design is made by the validation of the geometry through a full-wave solver, as it represents the best possible approximation for the electromagnetic behaviour of such structures.



**Figure 1.3:** (a) Actual metasurface and (b) homogenized metasurface with the surface impedance distribution.

## 1.2 Aim of the thesis

The design approach described in the previous section aims to find the impedance distribution by solving the integral equation associated with the electromagnetic problem of scattering by a metasurface. Finding the solution of this direct problem, which in general is carried out with an iterative approach, becomes pretty

computational inefficient when dealing with large sized antennas. Therefore, recent developments in MTS antenna design have shifted towards a current-based approach, where the impedance distribution is obtained from a current that satisfies the requirements of passivity, losslessness and radiated field pattern, which can be obtained by solving a multi-objective optimization problem. Unfortunately, the nature of such kind of problem, where the objective function to be minimized is the weighted sum of several functionals, is non-convex and slow convergent. Therefore, a first attempt to improve the algorithm performance has been made introducing slack variables, which are able to transform inequality constraints into equality constraints. Then, focusing on the optimization problem in its original form, other aspects were analyzed. The assigned weights plays a primary role in finding the optimal solution. Given the difficulty in assigning optimal weights to the objective functions a priori, this thesis proposes a novel re-weighting scheme capable of adaptively determining the weights during the minimization algorithm without altering the algebraic nature of the problem.

### **1.3 Thesis outline**

The thesis is composed of five main chapters organized as follows:

- Chapter 1 introduces metasurfaces, together with their potentialities, and the design approach is explained. Then, the aim of thesis is stated.
- Chapter 2 contains a review of the fundamentals needed to understand the electromagnetic radiation principle of metasurface antennas. A brief description of the Method of Moments is also reported, as it represents the basis for the optimization techniques described in following chapters.
- Chapter 3 gives a description of the recently developed current-based approach highlighting its distinctive aspects that formed the basis for subsequent discussion.
- In Chapter 4, the objective function modification employing slack variables is presented. Then, the proposed technique for adaptively modify the weights in a multi-objective optimization problem is described from a mathematical and algorithmic standpoint. The impact of the method on the final solution is discussed, as well as possible limitations.
- Chapter 5 collects a series of numerical results using the proposed method, for different antenna size and radiated field requirements. Results have been also compared with those obtained by the standard algorithm and presented in literature.

- In Chapter 6, a summary of the described work is given, as well as possible future developments and improvements.

# Chapter 2

## Electromagnetic formulation

This chapter describes the key ingredients needed to understand the radiation mechanism of the metasurface antenna and its properties from a physical standpoint.

### 2.1 EM radiation from sources

#### 2.1.1 Auxiliary potentials method

Maxwell's equations can be written in the frequency domain for an homogeneous, isotropic, non-dispersive medium as:

$$\nabla \times \mathbf{E} = -j\omega\mu\mathbf{H} - \mathbf{M}, \quad (2.1)$$

$$\nabla \times \mathbf{H} = j\omega\epsilon\mathbf{E} + \mathbf{J}, \quad (2.2)$$

$$\nabla \cdot \mathbf{E} = \frac{\rho_e}{\epsilon}, \quad (2.3)$$

$$\nabla \cdot \mathbf{H} = \frac{\rho_m}{\mu}, \quad (2.4)$$

where  $\epsilon = \epsilon_0\epsilon_r$  and  $\mu = \mu_0\mu_r$ . The magnetic current density  $\mathbf{M}$  and magnetic charge density  $\rho_m$  are fictitious quantities introduced to make Maxwell's equations symmetric and their presence will be justified later with the formulation of the Equivalence theorem. Maxwell's equations are completed by the continuity equations:

$$\nabla \cdot \mathbf{J} = -j\omega\rho_e \quad (2.5)$$

$$\nabla \cdot \mathbf{M} = -j\omega\rho_m. \quad (2.6)$$

A very common procedure to solve an electromagnetic problem is to introduce auxiliary functions, known as *vector potentials*, which can be related to the sources, and then find the radiated electromagnetic field  $\mathbf{E}$  and  $\mathbf{H}$ .

Let us suppose the absence of magnetic sources, i.e.  $\mathbf{M} = 0$ , which implies from (2.4) that  $\nabla \cdot \mathbf{H} = 0$ . Therefore, one can define:

$$\mathbf{H} = \nabla \times \mathbf{A}, \quad (2.7)$$

as  $\nabla \cdot \nabla \times \mathbf{A} = 0$ , where  $\mathbf{A}$  is the *magnetic vector potential*. It is worth mentioning that the choice of  $\mathbf{A}$  is not unique, since a generic vector is uniquely defined once assigned its curl and its divergence. From (2.1), in absence of magnetic sources,  $\nabla \times (\mathbf{E} + j\omega\mu\mathbf{A}) = 0$ , so then one can also define:

$$\mathbf{E} + j\omega\mu\mathbf{A} = -\nabla\Phi, \quad (2.8)$$

as  $\nabla \times \nabla\Phi = 0$ , where  $\Phi$  is the *magnetic scalar potential*. By considering the  $\nabla \times \nabla \times \mathbf{A}$  and substituting the (2.8), the following expression is obtained:

$$\nabla^2 \mathbf{A} + k^2 \mathbf{A} - \nabla(\nabla \cdot \mathbf{A} + j\omega\epsilon\Phi) = -\mathbf{J}, \quad (2.9)$$

where  $k = \omega\sqrt{\epsilon\mu}$ , which can be simplified thanks to the Lorentz gauge

$$\nabla \cdot \mathbf{A} + j\omega\epsilon\Phi = 0. \quad (2.10)$$

In this way, it can be appreciated that the magnetic vector potential satisfies the wave equation

$$\nabla^2 \mathbf{A} + k^2 \mathbf{A} = -\mathbf{J}. \quad (2.11)$$

The great advantage of this approach is that once determined the vector  $\mathbf{A}$  by solving (2.11), the electromagnetic field can be easily evaluated using:

$$\mathbf{H} = \nabla \times \mathbf{A}, \quad (2.12)$$

$$\mathbf{E} = -j\omega\mu\mathbf{A} + \frac{\nabla\nabla \cdot \mathbf{A}}{j\omega\epsilon}. \quad (2.13)$$

Eqs. (2.12)-(2.13) have been derived considering only electric sources. Similar expressions can be derived in terms of magnetic current density only by introducing auxiliary potentials  $\mathbf{F}$  and  $\Psi$ . Therefore, in presence of both electric and magnetic sources, the electromagnetic field can be computed simply by superposition of both sources terms.

The (2.11) can be solved with different approaches, one of the most common is by means of the Green's function.

### 2.1.2 Solution with the Green's function

Let us suppose that  $\mathbf{M} = 0$ , the equation to be solved (2.11) assumes the form of

$$\mathcal{L}\mathbf{f} = \mathbf{h}, \quad (2.14)$$

where  $\mathcal{L}$  is the linear operator  $-(\nabla^2 + k^2)$ ,  $\mathbf{f} = \mathbf{A}$  and  $\mathbf{h} = \mathbf{J}$ . The solution of the problem, for which  $\mathbf{f}$  and  $\mathbf{h}$  are generic functions, is found by means of the Green's function, defined as

$$\mathcal{L}G(\mathbf{r}, \mathbf{r}') = \delta(\mathbf{r}, \mathbf{r}'), \quad (2.15)$$

where  $\mathbf{r}$  and  $\mathbf{r}'$  are respectively the source point and the observation point,  $\delta(\mathbf{r}, \mathbf{r}')$  is the Dirac delta.

The solution of the scalar deterministic problem assumes the form:

$$f(\mathbf{r}) = \int_V G(\mathbf{r}, \mathbf{r}')h(\mathbf{r}')dV', \quad (2.16)$$

where  $V$  is a volume containing  $\mathbf{r}'$ . The expression of the Green's function can be computed for the free space, since it is the region of interest when radiation from antennas is considered. For the sake of simplicity, let us consider that the source point  $\mathbf{r}'$  coincides with the origin of the coordinates system, moreover let us employ a spherical coordinates systems (suitable for analyze the free space radiation). Exploiting the symmetries with respect to the coordinates  $\theta$  and  $\phi$ , the Green's function simplifies:

$$G(\mathbf{r}) \longrightarrow G(r). \quad (2.17)$$

The equation to be solved is therefore:

$$-(\nabla^2 + k^2)G(r) = \delta(r), \quad (2.18)$$

expliciting the  $\nabla^2$  operator, using the simplifying assumptions (related to the spherical coordinates) and integrating on a spherical volume  $V$ , the result is

$$G(r) = \frac{e^{-jkr}}{4\pi r}, \quad (2.19)$$

which can be generalized in:

$$G(\mathbf{r}, \mathbf{r}') = \frac{e^{-jk|\mathbf{r}-\mathbf{r}'|}}{4\pi|\mathbf{r}-\mathbf{r}'|}. \quad (2.20)$$

At last, the magnetic vector potential is found to be:

$$\mathbf{A}(\mathbf{r}) = \int_V \frac{e^{-jk|\mathbf{r}-\mathbf{r}'|}}{4\pi|\mathbf{r}-\mathbf{r}'|} \mathbf{J}(\mathbf{r}')dV', \quad (2.21)$$

which can be used together with (2.12)-(2.13) to obtain the following expression for the EM field

$$\mathbf{H}(\mathbf{r}) = \int_V \nabla \times [G(\mathbf{r}, \mathbf{r}')\mathbf{J}(\mathbf{r}')]dV' = \int_V \nabla G(\mathbf{r}, \mathbf{r}') \times \mathbf{J}(\mathbf{r}')dV', \quad (2.22)$$

$$\begin{aligned}
 \mathbf{E}(\mathbf{r}) &= -j\omega\mu \int_V G(\mathbf{r}, \mathbf{r}') \mathbf{J}(\mathbf{r}') dV' + \frac{1}{j\omega\epsilon} \int_V \nabla \nabla \cdot [G(\mathbf{r}, \mathbf{r}') \mathbf{J}(\mathbf{r}')] dV' \\
 &= -j\omega\mu \int_V G(\mathbf{r}, \mathbf{r}') \mathbf{J}(\mathbf{r}') dV' + \frac{1}{j\omega\epsilon} \int_V [\mathbf{J}(\mathbf{r}') \cdot \nabla] \nabla G(\mathbf{r}, \mathbf{r}') dV'.
 \end{aligned} \tag{2.23}$$

It is worth mentioning that all the computations above are referred to an isotropic medium. When the sources are placed in anisotropic media, the dyadic Green's function  $\overline{\overline{G}}(\mathbf{r}, \mathbf{r}')$  must be employed:

$$\overline{\overline{G}}(\mathbf{r}, \mathbf{r}') = \begin{bmatrix} G_{xx} & G_{xy} & G_{xz} \\ G_{yx} & G_{yy} & G_{yz} \\ G_{zx} & G_{zy} & G_{zz} \end{bmatrix} \tag{2.24}$$

which takes into account the effect of the sources on  $\mathbf{E}(\mathbf{r})$ ,  $\mathbf{H}(\mathbf{r})$  [3, p. 117].

## 2.2 Scattering formulation

### 2.2.1 Boundary conditions

Let us consider two media with different characteristics  $(\epsilon_1, \mu_1)$  and  $(\epsilon_2, \mu_2)$  separated by a surface  $S$ .  $\mathbf{E}_1, \mathbf{H}_1$  and  $\mathbf{E}_2, \mathbf{H}_2$  are solutions of Maxwell's equations in medium 1 and in medium 2 respectively.  $\hat{\mathbf{n}}$  is the unit vector normal to the surface (oriented from medium 1 to medium 2). From Maxwell's equations, if both electric and magnetic sources are present on the interface between the two media, it can be shown that:

$$(\mathbf{E}_2 - \mathbf{E}_1) \times \hat{\mathbf{n}} = \mathbf{M}_S, \tag{2.25}$$

$$\hat{\mathbf{n}} \times (\mathbf{H}_2 - \mathbf{H}_1) = \mathbf{J}_S. \tag{2.26}$$

Eqs. (2.25)-(2.26) tell us that the tangential components of the fields are discontinuous and the amount of discontinuity is given by equations above. The same can be said about the normal components, since:

$$\hat{\mathbf{n}} \cdot (\epsilon_2 \mathbf{E}_2 - \epsilon_1 \mathbf{E}_1) = \rho_{m_S} \tag{2.27}$$

$$\hat{\mathbf{n}} \cdot (\mu_2 \mathbf{H}_2 - \mu_1 \mathbf{H}_1) = \rho_{e_S}. \tag{2.28}$$

When no sources are present on the boundary, i.e. the discontinuity is between two dielectric, eqs. (2.25-2.26) and (2.27-2.28) becomes:

$$(\mathbf{E}_2 - \mathbf{E}_1) \times \hat{\mathbf{n}} = 0 \longrightarrow \mathbf{E}_2^t = \mathbf{E}_1^t \tag{2.29}$$

$$\hat{\mathbf{n}} \times (\mathbf{H}_2 - \mathbf{H}_1) = 0 \longrightarrow \mathbf{H}_2^t = \mathbf{H}_1^t \tag{2.30}$$

$$\hat{\mathbf{n}} \cdot (\epsilon_2 \mathbf{E}_2 - \epsilon_1 \mathbf{E}_1) = 0 \longrightarrow \epsilon_2 E_2^n = \epsilon_1 E_1^n \tag{2.31}$$

$$\hat{\mathbf{n}} \cdot (\mu_2 \mathbf{H}_2 - \mu_1 \mathbf{H}_1) = 0 \longrightarrow \mu_2 H_2^n = \mu_1 H_1^n \quad (2.32)$$

which tell that the tangential components are continuous, while the normal components are discontinuous.

In the case of a perfect electric conductor (PEC), for which  $\sigma \rightarrow \infty$ ,  $\mathbf{E}_1 = \mathbf{H}_1 = 0$  and no magnetic sources are present. Since on the surface of a PEC a flow of electric current density is present, it can be shown that:

$$\mathbf{E}_2 \times \hat{\mathbf{n}} = 0 \longrightarrow \mathbf{E}_2^t = 0, \quad (2.33)$$

$$\hat{\mathbf{n}} \times \mathbf{H}_2 = \mathbf{J}_s \longrightarrow \mathbf{H}_2^t = \mathbf{J}_s \quad (2.34)$$

$$\hat{\mathbf{n}} \cdot \epsilon_2 \mathbf{E}_2 = \rho_{es} \longrightarrow E_2^n = \frac{\rho_{es}}{\epsilon_2} \quad (2.35)$$

$$\hat{\mathbf{n}} \cdot \mu_2 \mathbf{H}_2 = 0 \longrightarrow H_2^n = 0. \quad (2.36)$$

One can conclude that: the tangential component of the electric field and the normal component of the magnetic field vanish, while the tangential magnetic field and the normal magnetic field are discontinuous next to a PEC.

### 2.2.2 Equivalence theorem

The *uniqueness theorem* states that the solution of an electromagnetic problem, created by sources placed in a region, is unique when the tangential component of the field (electric or magnetic) is specified over the boundary of the region. From this result, another important theorem can be formulated, the *surface equivalence theorem* [4]. Let us consider an homogeneous medium and a closed surface S which contains the sources ( $\mathbf{J}$  and  $\mathbf{M}$ ). The surface S can be an actual surface or a fictitious one, introduced only to separate conceptually the volume in which the sources are present  $V_1$ , with the rest of the space  $V_2$ . These electric and magnetic current densities radiate an EM field  $\mathbf{E}_1, \mathbf{H}_1$  everywhere: the surface equivalence theorem tells us that an equivalent problem can be formulated if in place of the sources, one considers  $\mathbf{E}, \mathbf{H}$  as arbitrary solution of Maxwell's equations inside  $V_1$  and  $\mathbf{E}_1, \mathbf{H}_1$  outside  $V_1$ . In order to this field to exist, it must satisfy the boundary conditions across the surface S, which means that surface equivalent electric and magnetic sources must exist, i.e.

$$\hat{\mathbf{n}} \times (\mathbf{H}_1 - \mathbf{H}) = \mathbf{J}_{Seq} \quad (2.37)$$

$$(\mathbf{E}_1 - \mathbf{E}) \times \hat{\mathbf{n}} = \mathbf{M}_{Seq} \quad (2.38)$$

which radiate into an unbounded homogeneous space, therefore radiated field can be computed through (2.22)-(2.23). Since only the radiation in  $V_2$  is of interest,

the field inside  $V_1$  can be anything: one of the most common choice is to take  $\mathbf{E} = \mathbf{H} = 0$ , for which (2.37)-(2.38) become

$$\hat{\mathbf{n}} \times \mathbf{H}_1 = \mathbf{J}_{Seq} \quad (2.39)$$

$$\mathbf{E}_1 \times \hat{\mathbf{n}} = \mathbf{M}_{Seq} \quad (2.40)$$

which can be used, together with (2.22)-(2.23) (and the dual formulas in terms of  $\mathbf{M}$ ), to solve the electromagnetic problem.

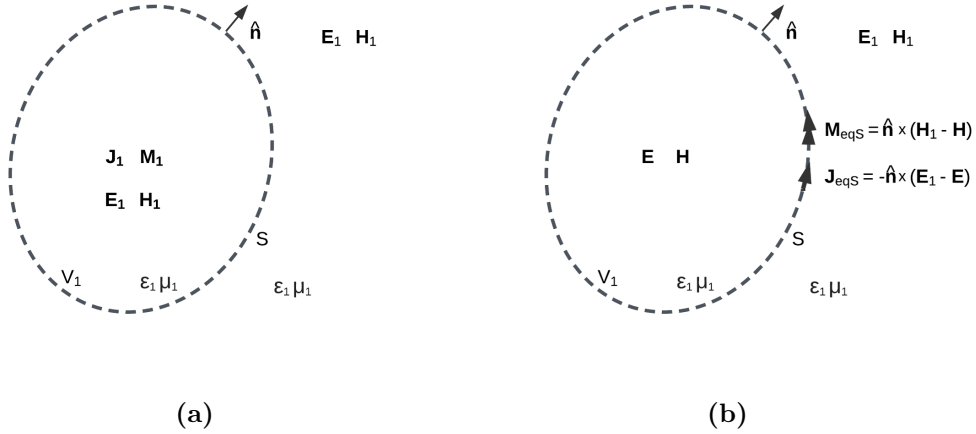


**Figure 2.1:** Surface equivalence theorem illustration: (a) actual and (b) equivalent problem.

The equivalence theorem can be applied also if  $S$  is an actual closed surface separating two media. Let us consider two volume,  $V_1$  and  $V_2$ , filled with different materials,  $\epsilon_1, \mu_1$  and  $\epsilon_2, \mu_2$ ; in the unbounded medium  $V_2$ , an electromagnetic field is present, which can be due to either sources placed in  $V_2$ , or can be a generic incident field (e.g. a plane wave) generated by the sources placed in the unbounded medium in absence of the obstacle. The total electromagnetic field radiated in the unbounded medium will be given by the incident field, plus a perturbation due to the obstacle in  $V_1$ , called scattered field.

$$\mathbf{E}_{tot} = \mathbf{E}_{inc} + \mathbf{E}_s \quad (2.41)$$

$$\mathbf{H}_{tot} = \mathbf{H}_{inc} + \mathbf{H}_s. \quad (2.42)$$

By using the surface equivalence theorem, one can impose zero field inside  $V_1$  and replace the characteristics of medium 2 with those of the background medium (i.e. the unbounded space). The problem does not change if equivalent sources are placed on the  $S$  such that:

$$\hat{\mathbf{n}} \times \mathbf{H}_{tot} = \mathbf{J}_{Seq}, \quad (2.43)$$

$$\mathbf{E}_{tot} \times \hat{\mathbf{n}} = \mathbf{M}_{Seq}, \quad (2.44)$$

which are now allowed to radiate into an homogeneous unbounded space. Therefore, the scattered field,  $\mathbf{E}_s(\mathbf{J}_{Seq}, \mathbf{M}_{Seq})$  and  $\mathbf{H}_s(\mathbf{J}_{Seq}, \mathbf{M}_{Seq})$ , which are function of the equivalent sources, can be computed through (2.22)-(2.23) (and the dual formulas in terms of  $\mathbf{M}$ ), supposing that one is able to express the Green's function of the background medium.

Let us suppose that the boundary condition of the tangential component of the electric field on  $S$  preserves its continuity, so then  $\mathbf{M}_{Seq} = 0$ . This allows to write a set of equations

$$\begin{cases} \mathbf{E}_{tot}^t = \mathcal{BC}(\mathbf{J}_{Seq}) \\ \mathbf{E}_s = \mathcal{L}(\mathbf{J}_{Seq}) \\ \mathbf{E}_{tot}^t = \mathbf{E}_{inc}^t + \mathbf{E}_s^t \end{cases} \quad (2.45)$$

which can be used to write the *electric field integral equation* (EFIE):

$$\mathcal{BC}(\mathbf{J}_{Seq}) = \mathcal{L}(\mathbf{J}_{Seq})|_t + \mathbf{E}_{inc}^t. \quad (2.46)$$

When dealing with scattering problems in presence of a infinitely extended PEC plane, the LHS of the (2.46) is equal to zero, while in the case of metasurface, an appropriate boundary condition must be applied, as will be detailed in the next chapter.

Since  $\mathbf{E}_{inc}$  is a known quantity, the Equation 2.46 can be solved in terms of the equivalent current only and therefore it lends itself to numerical solutions.

## 2.3 Method of moments

The electromagnetic problem described in the previous section can be numerically solved using the *Method of Moments* (MoM) [5]. The general problem in (2.46) has the following form:

$$\mathcal{L}(\mathbf{f}) = \mathbf{g}, \quad (2.47)$$

where  $\mathcal{L}$  is a linear integral-differential operator (e.g. the one extrapolated from (2.22)-(2.23)),  $\mathbf{g}$  is the forcing known term (e.g. the incident field) and  $\mathbf{f}$  is the unknown function (the equivalent current density). In order to solve numerically the (2.47),  $\mathbf{f}$  must be expanded into a sum of  $N$  basis functions:

$$\mathbf{f} = \sum_{n=1}^N I_n \mathbf{f}_n, \quad (2.48)$$

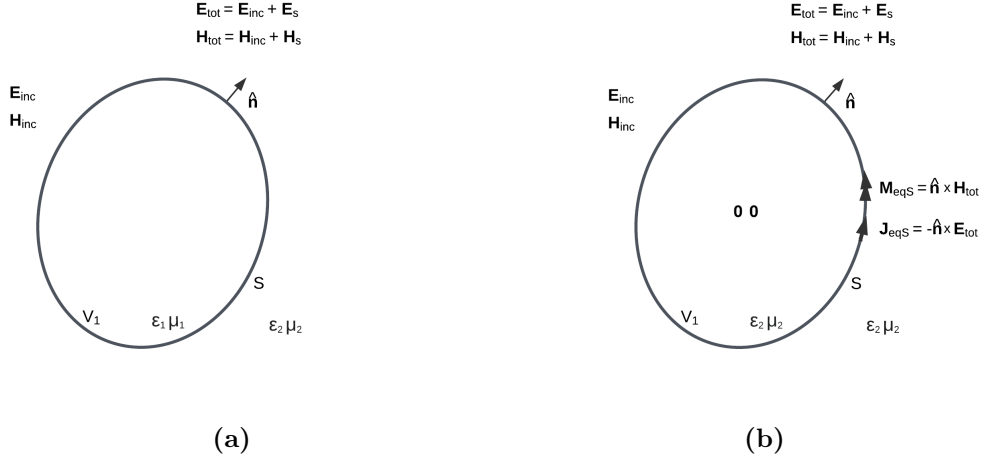


**Figure 2.2:** Surface equivalence theorem in presence of an actual obstacle: (a) actual and (b) equivalent problems.

where  $I_n$  is the unknown coefficient and  $\mathbf{f}_n$  is a basis function chosen such that it reflects the behaviour of the unknown function within its domain in order to obtain a good approximation. Substituting the (2.48) into (2.47) and exploiting the linearity of the operator  $\mathcal{L}$ ,

$$\sum_{n=1}^N I_n \mathcal{L}(\mathbf{f}_n) \approx \mathbf{g}, \quad (2.49)$$

therefore, the residual of the approximation is simply given by

$$\mathbf{R} = \mathbf{g} - \sum_{n=1}^N I_n \mathcal{L}(\mathbf{f}_n) \quad (2.50)$$

and one must find the coefficients  $I_n$  such that the residual  $\mathbf{R}$  is minimized. To do so, the inner product is introduced

$$\langle \mathbf{w}_m, \mathbf{f}_n \rangle = \iint_{\mathcal{D}} \mathbf{w}_m(\mathbf{r}) \cdot \mathbf{f}_n(\mathbf{r}) d\mathcal{D}, \quad (2.51)$$

where  $\mathbf{w}_m$  is the *testing* (or *weighting*) basis function and  $\mathcal{D}$  is the intersection of the definition domain of the actual basis functions  $\mathcal{D}_f$  and of those used as testing  $\mathcal{D}_w$ .

Enforcing that the residual is outside the subspace defined by the testing function, i.e.

$$\langle \mathbf{w}_m, \mathbf{R} \rangle = 0 \quad \forall m = 1, \dots, N \quad (2.52)$$

and substituting it inside the (2.50), one gets

$$\sum_{n=1}^N I_n \langle \mathbf{w}_m, \mathcal{L}(\mathbf{f}_n) \rangle = \langle \mathbf{w}_m, \mathbf{g} \rangle. \quad (2.53)$$

The previous equation can be written in compact form as

$$\mathbf{Z} \mathbf{l} = \mathbf{V}, \quad (2.54)$$

thus, the generic EFIE can be discretized. In (2.54)

$$\mathbf{Z} = \begin{bmatrix} \langle \mathbf{w}_1, \mathcal{L}(\mathbf{f}_1) \rangle & \langle \mathbf{w}_1, \mathcal{L}(\mathbf{f}_2) \rangle & \dots & \langle \mathbf{w}_1, \mathcal{L}(\mathbf{f}_N) \rangle \\ \langle \mathbf{w}_2, \mathcal{L}(\mathbf{f}_1) \rangle & \langle \mathbf{w}_2, \mathcal{L}(\mathbf{f}_2) \rangle & \dots & \langle \mathbf{w}_2, \mathcal{L}(\mathbf{f}_N) \rangle \\ \vdots & \vdots & \ddots & \vdots \\ \langle \mathbf{w}_N, \mathcal{L}(\mathbf{f}_1) \rangle & \langle \mathbf{w}_N, \mathcal{L}(\mathbf{f}_2) \rangle & \dots & \langle \mathbf{w}_N, \mathcal{L}(\mathbf{f}_N) \rangle \end{bmatrix}$$

$$\mathbf{l} = \begin{bmatrix} I_1 \\ I_2 \\ \vdots \\ I_N \end{bmatrix} \quad \mathbf{V} = \begin{bmatrix} \langle \mathbf{w}_1, \mathbf{g} \rangle \\ \langle \mathbf{w}_2, \mathbf{g} \rangle \\ \vdots \\ \langle \mathbf{w}_N, \mathbf{g} \rangle \end{bmatrix}$$

The linear system (2.54) must be solved with respect to  $\mathbf{l}$  and then the unknown function  $\mathbf{f}$  can be reconstructed through (2.48). Iterative methods, such as linear conjugate gradient algorithms, as well as direct solvers that alter the original system, such as Gaussian Elimination or LU decomposition, can be used to obtain the solution.

The choice of the testing function can be done following the *Galerkin method*, where the same basis function are chosen for both the discretization of the  $\mathbf{f}$  and for the testing, i.e.  $\mathbf{w}_n = \mathbf{f}_n$ .

When dealing with scattering or radiation problems in three-dimensional space, it is a very common practice to discretize the surface by dividing it into triangular cells. In this way, it is possible to model surfaces of arbitrary shape and size. In this scenario, one of the most common choices for addressing the problem is to use RWG basis functions, which are local basis functions defined on pairs of triangles that share an edge [6]. Considering two adjacent triangles  $T_n^+$  and  $T_n^-$ , the basis function  $\mathbf{f}_n$  associated with the common edge  $e_n$  is defined as

$$\mathbf{f}_n(\mathbf{r}) = \begin{cases} \frac{l_n}{A_n^+} \boldsymbol{\rho}_n^+(\mathbf{r}) & \mathbf{r} \in T_n^+ \\ \frac{l_n}{A_n^-} \boldsymbol{\rho}_n^-(\mathbf{r}) & \mathbf{r} \in T_n^- \\ 0 & \text{otherwise} \end{cases} \quad (2.55)$$

where  $l_n$  is the edge length and  $A_n^\pm$  is the area of the  $T_n^\pm$  triangle. The vector  $\boldsymbol{\rho}_n^+$  points in the opposite direction of the free vertex  $\mathbf{v}^+$  of  $T_n^+$  and is defined as

$$\boldsymbol{\rho}_n^+ = \mathbf{r} - \mathbf{v}^+ \quad \mathbf{r} \in T_n^+, \quad (2.56)$$

while  $\boldsymbol{\rho}_n^-$  points in the opposite direction of the free vertex  $\mathbf{v}^-$  of  $T_n^-$  (see Figure 2.3)

$$\boldsymbol{\rho}_n^- = \mathbf{v}^- - \mathbf{r} \quad \mathbf{r} \in T_n^-. \quad (2.57)$$

By their definition, RWG basis functions are assigned only to internal edges, therefore, each internal triangular cell has three basis function assigned to. These

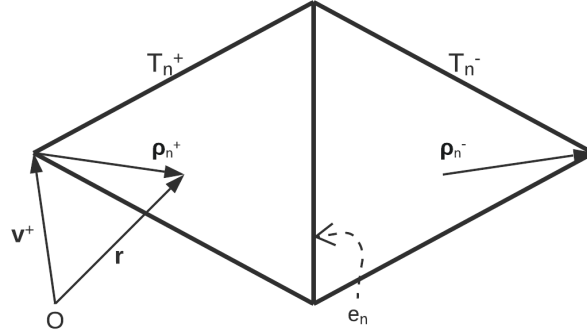


**Figure 2.3:** Graphical representation of RWG basis function.

basis functions are the most commonly used when dealing with 3D electromagnetic problems thanks to their properties here summarized:

- The current has no component normal to boundary edges, i.e. those which are not common to any triangles.
- The normal component to internal edges is continuous across the edge.
- The parallel component to internal edges is discontinuous.
- The surface divergence of  $\mathbf{f}_n$  is

$$\nabla_s \cdot \mathbf{f}_n = \begin{cases} \frac{l_n}{A_n^+} & \mathbf{r} \in T_n^+ \\ -\frac{l_n}{A_n^-} & \mathbf{r} \in T_n^- \\ 0 & \text{otherwise} \end{cases} \quad (2.58)$$

This makes the charge density constant within each triangle, while the net charge density of the pair of adjacent triangles  $T_n^+$  and  $T_n^-$  is null.

## Chapter 3

# Current-based optimization algorithm

The development framework for the work carried out is the *Current-Based Optimization Algorithm* [7]. In this chapter, a brief description of the algorithm is provided, highlighting its distinctive aspects that formed the basis for subsequent discussions. This algorithm is capable to obtain an equivalent current distribution, and then an impedance distribution, satisfying the requirements on the radiated field and the constraints on the realizability of the metasurface antenna.

### 3.1 Electromagnetic problem formulation

Concerning metasurfaces, the discontinuity of the tangential magnetic field is related to the tangential electric field through the surface impedance  $\overline{\mathbf{Z}}(\mathbf{r})$ , which is in general a space-varying tensor. The resulting relation is called *Impedance Boundary Condition* (IBC) [2]:

$$\mathbf{E}_{tan} = \overline{\mathbf{Z}} \cdot [\hat{\mathbf{n}} \times (\mathbf{H}^+ - \mathbf{H}^-)]. \quad (3.1)$$

The surface equivalence theorem states that the electromagnetic field outside a closed surface  $S$ , that bounds a volume containing the sources, can be expressed in terms of equivalent sources, determined from the knowledge of the tangential components of the fields on  $S$ :

$$\begin{aligned} \mathbf{J}_{eq} &= \hat{\mathbf{n}} \times \mathbf{H}, \\ \mathbf{M}_{eq} &= -\hat{\mathbf{n}} \times \mathbf{E}. \end{aligned} \quad (3.2)$$

Considering the Figure 3.1, by making the volume that bounds the MTS collapsing to the  $S_{IBC}$  from both sides, the total equivalent electric and magnetic



**Figure 3.1:** Graphical application of the Equivalence theorem. The dashed line represents the volume containing the sources.

currents are given by:

$$\begin{aligned} \mathbf{J}_{eq} &= \hat{\mathbf{n}} \times (\mathbf{H}^+ - \mathbf{H}^-), \\ \mathbf{M}_{eq} &= -\hat{\mathbf{n}} \times (\mathbf{E}^+ - \mathbf{E}^-). \end{aligned} \quad (3.3)$$

Typically, a metasurface is made by printed metallic patches, therefore it does not introduce any electric field discontinuity: as consequence,  $\mathbf{M}_{eq} = 0$ . With (3.3), (3.1) can be written as:

$$\mathbf{E}_{tan} = \overline{\overline{\mathbf{Z}}} \cdot \mathbf{J}_{eq}. \quad (3.4)$$

The tangential electric field can be written as:

$$\mathbf{E}_{tan} = [\mathbf{E}_{inc} + \mathbf{E}_s]_{tan}, \quad (3.5)$$

where  $\mathbf{E}_s = \mathcal{L}\mathbf{J}_{eq}$  is the electric field radiated by the equivalent currents and  $\mathcal{L}$  is the *electric field integral operator* (EFIO). In this way, the (3.4) becomes:

$$[\mathbf{E}_{inc}(\mathbf{r}) + \mathcal{L}\mathbf{J}_{eq}(\mathbf{r})]_{tan} = Z(\mathbf{r})\mathbf{J}_{eq}(\mathbf{r}) \quad \forall \mathbf{r} \in S_{IBC}, \quad (3.6)$$

which is the electric field integral equation defined in (2.46) when the IBC is employed (EFIE-IBC). The EFIO in (3.6) is defined as:

$$\mathcal{L}\mathbf{J}(\mathbf{r}) = \iint_{S_{IBC}} \overline{\overline{\mathbf{G}}}^{EJ}(\mathbf{r}, \mathbf{r}') \cdot \mathbf{J}(\mathbf{r}') dS(\mathbf{r}'), \quad (3.7)$$

where  $\overline{\overline{\mathbf{G}}}^{EJ}$  is the multilayer dyadic Green's function [8].

Since the specifications on the radiated fields are in the far-field region (FF), the *radiation operator* is employed:

$$\mathcal{R}\mathbf{J}(\mathbf{r}) = \frac{jk_0}{2\pi} \overline{\overline{\mathbf{G}}}^{FF}(\hat{\mathbf{r}}) \cdot \iint_{S_{IBC}} \mathbf{J}(\mathbf{r}') e^{jk_0 \hat{\mathbf{r}} \cdot \mathbf{r}'} dS(\mathbf{r}'), \quad (3.8)$$

where  $\overline{\overline{\mathbf{G}}}^{FF}$  is the multi-layer far field tensor,

$$\overline{\overline{\mathbf{G}}}^{FF} = -g^{TM}(\hat{\mathbf{r}})\hat{\boldsymbol{\theta}}\hat{\boldsymbol{\rho}} - \cos\theta g^{TE}(\hat{\mathbf{r}})\hat{\boldsymbol{\phi}}\hat{\boldsymbol{\phi}}. \quad (3.9)$$

In (3.9),  $\hat{\boldsymbol{\rho}}$ ,  $\hat{\boldsymbol{\theta}}$ ,  $\hat{\boldsymbol{\phi}}$  are the unit vectors for the spherical coordinates system, while  $g^{TE}$  and  $g^{TM}$  are the transmission line transfer functions for the TE and TM components.

The (3.6) requires the employing of numerical methods in order to find its solution, therefore it must be discretized using the Method of Moments approach, in which the metasurface is represented as a triangular mesh and the current  $\mathbf{J}$  is approximated as a linear combination of the RWG basis functions  $\boldsymbol{\Lambda}_n$ :

$$\mathbf{J}(\mathbf{r}) = \sum_{n=1}^N I_n \boldsymbol{\Lambda}_n, \quad (3.10)$$

where  $N$  is the number of internal mesh edges. By testing the integral equation with the Galerkin's method, as detailed in the previous chapter, the (3.6) becomes the linear system:

$$\mathbf{V}_{inc} + \mathbf{L}\mathbf{l} = \mathbf{Z}\mathbf{l}, \quad (3.11)$$

where  $\mathbf{l}$  contains the RWG basis coefficients and

$$\begin{aligned} (\mathbf{V}_{inc})_m &= \langle \boldsymbol{\Lambda}_m, \mathbf{E}_{inc} \rangle \\ (\mathbf{L})_{mn} &= \langle \boldsymbol{\Lambda}_m, \mathcal{L}\boldsymbol{\Lambda}_n \rangle \\ (\mathbf{Z})_{mn} &= \langle \boldsymbol{\Lambda}_m, \mathcal{Z}\boldsymbol{\Lambda}_n \rangle \end{aligned} \quad (3.12)$$

The previous expression allows both the evaluation of the equivalent electric current coefficients  $\mathbf{l}$  from the impedance  $\mathbf{Z}$ , solving the linear system

$$(\mathbf{Z} - \mathbf{L})\mathbf{l} = \mathbf{V}_{inc}, \quad (3.13)$$

as well as the impedance computation from the found  $\mathbf{l}$ . The latter approach is the one employed in [7].

## 3.2 Constraints definition

The design of a metasurface antenna aims to achieve the desired radiated field using a structure that is feasible. Therefore, first and foremost, the feasibility condition must be enforced, which translates into a structure that overall neither dissipates nor provides active power. The expression of the complex power density absorbed by a metasurface, computed from the Poynting Theorem, is:

$$\tilde{p} = \mathbf{E}_{tan} \cdot [\hat{\mathbf{n}} \times (\mathbf{H}^+ - \mathbf{H}^-)]^*. \quad (3.14)$$

If the considered impedance is scalar, i.e.

$$\overline{\mathbf{Z}} = Z\overline{\mathbf{I}}, \quad (3.15)$$

where  $\overline{\mathbf{I}}$  is the identity tensor, the (3.14) becomes:

$$\tilde{p} = \mathbf{E}_{tan} \cdot \mathbf{J}_{eq}^* = Z(\mathbf{J}_{eq} \cdot \mathbf{J}_{eq}^*) = Z|\mathbf{J}_{eq}|^2. \quad (3.16)$$

By imposing  $Re\{\tilde{p}\} = 0$ , which guarantees a passive and lossless structure, the only one solution is:

$$Re\{Z(\mathbf{r})\} = 0 \quad \forall \mathbf{r} \in S_{IBC}. \quad (3.17)$$

Furthermore, to ensure that the structure can be realizable with metallic patches, the reactance must be capacitive and must adhere to technological bounds,

$$X_L \leq Im\{Z(\mathbf{r})\} \leq X_U \quad \forall \mathbf{r} \in S_{IBC}. \quad (3.18)$$

About the specifications on the radiated field, they are typically expressed in terms of field amplitude  $F(\hat{\mathbf{r}}, \mathbf{l}) \propto |\mathbf{E}(\hat{\mathbf{r}}, \mathbf{l})|^2$  - where  $\hat{\mathbf{r}}$  is the far field direction - and refer to the total amplitude and to the co- and cross-polarization components. The result of the design must be an antenna radiating a field whose amplitude is bounded, i.e.

$$M_L(\hat{\mathbf{r}}, \mathbf{l}) \leq F(\hat{\mathbf{r}}, \mathbf{l}) \leq M_U(\hat{\mathbf{r}}, \mathbf{l}), \quad (3.19)$$

for each far field direction. The requirement on the main lobe (co-polarization) can be defined in terms of absolute value, while the amplitude of the side lobes and the cross-polarizations levels must refer to the main beam effective level. Therefore, it is convenient to define a reference main lobe level as follows,

$$F_{ref}(\mathbf{l}) = \frac{1}{\Omega_0} \iint_{\Omega_0} F^{co}(\hat{\mathbf{r}}, \mathbf{l}) d\Omega(\hat{\mathbf{r}}), \quad (3.20)$$

which represents an average on an angular region  $\Omega_0$  around the maximum radiation direction  $\hat{\mathbf{r}}_0$ . In this way, the side lobes and the cross-pol level will always comply the specification even if the the main lobe does not. The value of  $F_{ref}(\mathbf{l})$  is only lower bounded, i.e.,

$$F_{ref}(\mathbf{l}) \geq M_0, \quad (3.21)$$

and all the other requirements can be stated relatively to it:

$$\mu_L^{co}(\hat{\mathbf{r}})F_{ref}(\mathbf{l}) \leq F^{co}(\hat{\mathbf{r}}, \mathbf{l}) \leq \mu_U^{co}(\hat{\mathbf{r}})F_{ref}(\mathbf{l}) \quad \forall \hat{\mathbf{r}} \in \Omega_{ML}, \quad (3.22)$$

where  $\mu_L^{co}$  and  $\mu_U^{co}$  represent the lower and the upper relative level associated to the main beam and  $\Omega_{ML}$  is the main lobe region.

For the cross-polarization and the total amplitude:

$$F^{cx}(\hat{\mathbf{r}}, \mathbf{l}) \leq \sigma^{cx}(\hat{\mathbf{r}})F_{ref}(\mathbf{l}) \quad \forall \hat{\mathbf{r}} \in \Omega_{ML}, \quad (3.23)$$

$$F^{tot}(\hat{\mathbf{r}}, l) \leq \sigma^{SL}(\hat{\mathbf{r}})F_{ref}(l) \quad \forall \hat{\mathbf{r}} \in \Omega_{SL}, \quad (3.24)$$

where  $\sigma^{cx}$  and  $\sigma^{SL}$  defines respectively the desired relative level for the cross-pol and the side lobes.  $\Omega_{SL}$  is the side lobe region.

A graphical example of the masks defined above is described in Figure 3.2.

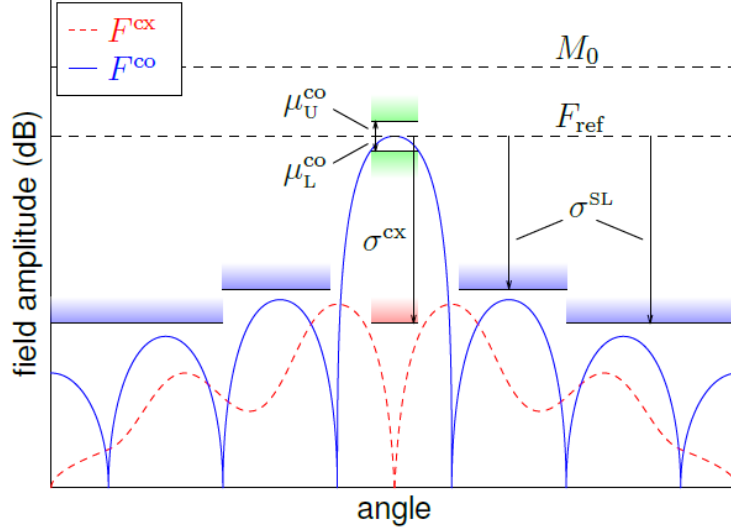


**Figure 3.2:** Graphical representation of the radiated field masks:  $M_0$  and  $F_{ref}$  are respectively the objective level and the reference level for the main lobe. Relative levels for cross-pol and side lobes are represented by vertical arrows.

### 3.3 Algorithm formulation

As explained in section 3.1, the design of MTS antennas is done by means of numerical methods in order to solve (3.11). In order to do so, the metasurface  $S_{IBC}$  must be meshed considering a lattice of  $N_c$  triangular cells  $S_i$ . An example of the triangular mesh is shown in Figure 3.3. The most straightforward approach to obtaining the spatial distribution of impedance is starting from an initial guess for  $Z$  - computed as the ratio of the power absorbed to the magnitude square of the current - and then evaluating the current coefficient  $l$  solving (3.11). From the current, the radiated field can be evaluated and the value of  $l$  for the next iteration is found computing the one that best approximates the radiated field.

Since this approach requires the solution of the linear system (3.11) at each iteration, it is unfeasible, from a computational standpoint, for solving large-sized antennas.

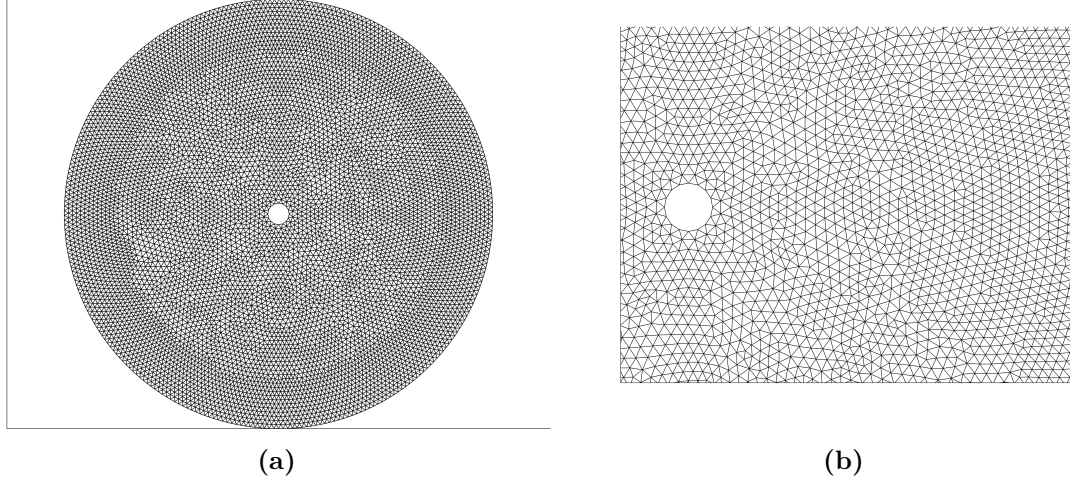


**Figure 3.3:** Triangular mesh of a  $10\lambda_0$  diameter circular metasurface antenna. The hole in the centre has a  $\lambda_0/2$  diameter and hosts the feed.

Therefore, the algorithm in [7] has been formulated such that only the current is involved in the optimization process, while the impedance will be evaluated at the end.

The optimal current is computed solving the unconstrained optimization problem,

$$\mathbf{l}^* = \arg \min_{\mathbf{l} \in \mathbb{C}^N} f(\mathbf{l}), \quad (3.25)$$

where the function  $f$  is formulated such that from  $\mathbf{l}^*$ , the resulting metasurface antenna adheres to all the constraints defined in section 3.1. In particular,

$$f(\mathbf{l}) = f_{rlz}(\mathbf{l}) + f_{rad}(\mathbf{l}). \quad (3.26)$$

The first term in (3.26),

$$f_{rlz}(\mathbf{l}) = w_{act} \sum_{i=1}^{Nc} \rho_i^{act}(\mathbf{l}) + w_{rct} \sum_{i=1}^{Nc} \rho_i^{rct}(\mathbf{l}) + w_{scal} \sum_{i=1}^{Nc} \rho_i^{scal}(\mathbf{l}), \quad (3.27)$$

is formulated such that the resulting current from (3.35) leads to a scalar impedance (*scal*), a passive and lossless structure (*act*) with a resulting reactance (*rct*) limited by technological bounds. The second term in (3.26) is

$$f_{rad}(\mathbf{l}) = \rho_{ref}(\mathbf{l}) + w_{ML} \sum_{j \in \Omega_{ML}} (\rho_j^{co}(\mathbf{l}) + \rho_j^{cx}(\mathbf{l})) + w_{SL} \sum_{j \in \Omega_{SL}} \rho_j^{tot}(\mathbf{l}), \quad (3.28)$$

which guarantees that the radiated field is inside the masks (see Figure 3.2).

By using (3.27) and (3.28), the  $f(\mathbf{l})$  is a scalar function made by the weighted sum

of several objective functions: each  $w$  is a scalar positive quantity to be assigned a-priori.

The constraints defined in section 3.1, on the contrary to traditional optimization problems, are employed as objective functions, therefore it is important to express each of them as function of the current  $\mathbf{l}$  only. It is worth mentioning how the term related to the scalarity must be enforced. A scalar impedance relates the electric field and the current density in such a way that they have the same orientation, i.e.  $\mathbf{E} = Z\mathbf{J}^*$ , as two vectors related by a scalar quantity are parallel the each other. Therefore, this condition can be enforced by using

$$|\mathbf{E} \cdot \mathbf{J}^*| = |\mathbf{E}||\mathbf{J}^*|. \quad (3.29)$$

About the other constraints, those definite via inequality, like reactance bounds and radiated field levels, they have been defined in the overall objective function using the ramp function

$$\text{ramp}(x) = \max(x, 0), \quad (3.30)$$

which means that any inequality can be written as:

$$a \leq x \leq b \rightarrow \begin{cases} \text{ramp}(a - x) = 0 \\ \text{ramp}(x - b) = 0. \end{cases} \quad (3.31)$$

Actually, the ramp function does not have a continuous derivative, so this problem has been solved by using the squared ramp function  $\text{ramp}^2(x) = \max(x, 0)^2$  (see Figure 3.4).

The function  $f(\mathbf{l})$  has been organized into functionals of the current  $\mathbf{l}$  only which are, for practical reasons, fourth-degree polynomials. Let us consider as example the terms associated with the active power, i.e.  $\rho_i^{act}(\mathbf{l}) = \mathcal{P}_i$  with  $i = 1, \dots, N_c$ : the sought current must guarantee that the power over each cell is equal to zero. Since the power is proportional to the square of the current, it is natural to represent its functional as a second-degree polynomial of the current. In this way, the sum of the active power over each mesh cell can be zero, but it is not guarantee that each cell does not dissipate, nor provide active power, as positive and negative terms can be summed together. Therefore, since the sum of positive terms is zero if and only if all terms are zero, the functional has been organized as squared second-degree polynomial. In this way, a pure zero of the functional guarantee both passivity and losslessness. The general algebraic expression of the objective function is

$$f(\mathbf{l}) = \sum_i q_i(\mathbf{l})s_i(\mathbf{l}) + \sum_i \text{ramp}^2(t_i(\mathbf{l})), \quad (3.32)$$

where  $q_i$ ,  $s_i$  and  $t_i$  are multivariable quadratic function of the current coefficient in the form:

$$q_i(\mathbf{l}) = \text{Re}\{\mathbf{l}^H \mathbf{A}_i \mathbf{l} + \mathbf{l}^H \mathbf{b}_i + c_i\} \quad (3.33)$$

and  $\mathbf{A} \in \mathbb{C}^{N \times N}$  and symmetric,  $\mathbf{b} \in \mathbb{C}^N$ ,  $c \in \mathbb{C}$  and  $\mathbf{l} \in \mathbb{C}^N$ . The objective function

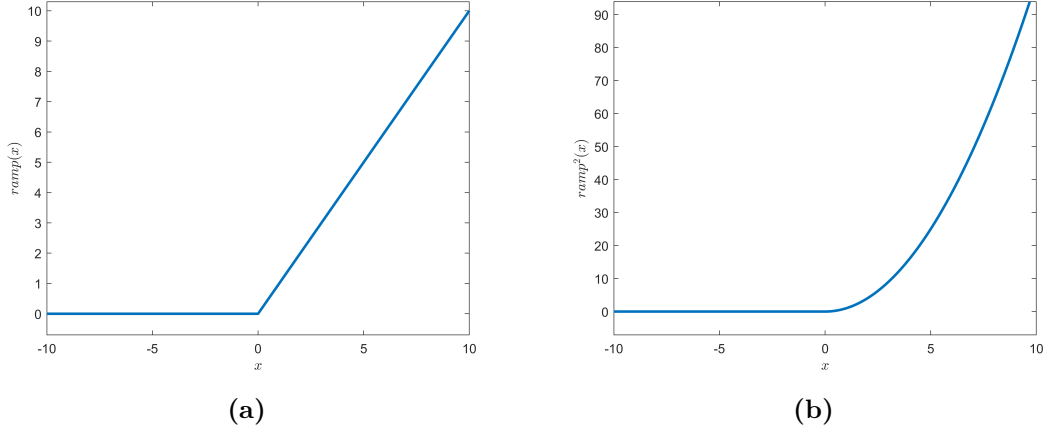


**Figure 3.4:** Comparison between (a) ramp function and (b) squared ramp function.

(3.26) is minimized using the *Non Linear Conjugate Gradient* algorithm [9] (see App C): the update value of the current coefficient array is computed through

$$\mathbf{l}_{k+1} = \mathbf{l}_k + \alpha_k \mathbf{p}_k, \quad (3.34)$$

where  $\mathbf{l}_k$  is the current value of the current,  $\mathbf{p}_k$  is the update direction and  $\alpha_k$  is the coefficient to be found.

The value  $\alpha$  is computed using the *linesearch* procedure [7, p. 4896], which consists in a one dimensional minimization of the objective function along the search direction:

$$\alpha^* = \arg \min_{\alpha \in \mathbb{R}} f(\mathbf{l} + \alpha \mathbf{p}). \quad (3.35)$$

The linesearch is a relatively simple task, provided that the objective function is written as function of the only  $\alpha$ , because it would require to find a minimum of a piece-wise (due to the presence of the ramp functions) fourth-degree polynomial. As a matter of fact, the derivative of the functional is a third-degree polynomial with two maxima and one minimum, which can be easily found by inspection. Although the choice of using fourth-order polynomials is advantageous from a computational perspective, it makes the optimization problem inherently non-convex. This can be confirmed by fixing an initial value of  $\mathbf{l}$  and a search direction  $\mathbf{p}$ : the objective function will then be a sum of fourth-order polynomials, so generally non-convex. This aspect will be discussed in more details in the following chapter.

At last, solving the (3.11) with the optimum  $\mathbf{l}^*$  the surface distribution  $Z(\mathbf{r})$  can be obtained [7, p. 4897].

In order to do so, one must start formulating an expression of the impedance distribution in terms of  $L$  basis functions  $\Phi_i(\mathbf{r})$

$$Z(\mathbf{r}) = \sum_{i=1}^L z_i \Phi_i(\mathbf{r}). \quad (3.36)$$

Then,  $\mathbf{Z}_{mn}$  can be found by its definition in (3.12) and the (3.11) can be solved with respect to  $\mathbf{z}$  (which collects the coefficients  $z_i$ ) as a linear least-square optimization problem. The choice of the basis functions used to expand the impedance distribution in (3.36) is arbitrarily, as well as the testing functions for computing the IBC matrix  $\mathbf{Z}$ . In particular, one can choose

$$\Phi_i(\mathbf{r}) = \Pi_i(\mathbf{r}) = \begin{cases} 1 & \text{for } \mathbf{r} \in S_i \\ 0 & \text{elsewhere} \end{cases} \quad (3.37)$$

with  $L = N_c$  and  $S_i$  is the domain spanned by the basis function. Then, by choosing as testing functions the complex conjugate of the optimized current over the mesh cell, i.e.

$$\Psi_j(\mathbf{r}) = \Pi_j(\mathbf{r}) \mathbf{J}^*(\mathbf{r}) = \begin{cases} \mathbf{J}^*(\mathbf{r}) & \text{for } \mathbf{r} \in S_j \\ 0 & \text{elsewhere} \end{cases} \quad (3.38)$$

where  $S_j$  is the area of the mesh cell and  $j = 1, \dots, N_c$ , the EFIE-IBC results as a diagonal and square system, therefore it can be solved in closed form.

Since the impedance is basically computed involving the ratio of the electric field  $\mathbf{E}$  and current density  $\mathbf{J}$ , indeterminate forms may arise, which are the reason why a regularization is needed. There are four possible combinations of values: when both  $\mathbf{E}$  and  $\mathbf{J}$  are non-zero the impedance is computed solving the EFIE-IBC. When the current is null and the field is not it represents an open circuit ( $Z = \infty$ ), while when the electric field is null and the current is not, it represents a short circuit ( $Z = 0$ ), corresponding to a PEC boundary condition. At last, when both current and electric field are null, the impedance is undefined and therefore it is computed by interpolating values of the neighboring cells.

The above mentioned conditions are summarized in Table 3.1.

Practically speaking, the regularization of the impedance is done employing two thresholds  $\tau_v$  and  $\tau_i$ , respectively for the electric field and the current density, in order to handle numerical tolerances.

The very last step of the optimization consists of solving the EFIE-IBC in (3.13) with respect to the current with the previously obtained impedance, the result is then used to compute the radiated field. This last stage is not really mandatory, but since the direct problem is the most studied and has well-established properties, the convergence of the solution of (3.13) is sign of a good-quality result.

	$ \mathbf{J}  = 0$	$ \mathbf{J}  \neq 0$
$ \mathbf{E}  = 0$	$Z$ undefined	$Z = 0$
$ \mathbf{E}  \neq 0$	$Z = \infty$	$Z =  \mathbf{E} / \mathbf{J} $

**Table 3.1:** Summary of all possible combinations of  $\mathbf{J}$  and  $\mathbf{E}$ .

# Chapter 4

## Optimization strategies

As detailed in chapter 3, the Current-Based Optimization Algorithm [7] minimizes the function (3.26), which is the weighted sum of several optimization functions. First of all, problem formulation based on slack variables is described. Then, the meaning and the impact of the weights in a multi-objective optimization problem will be discussed. A new method to adaptively determine and modify the weights during the algorithmic process is finally proposed.

### 4.1 Slack variables

Within the scope of optimization problems, slack variables are introduced to transform inequality constraints into equality constraints. Let us consider a simple linear programming problem:

$$\begin{aligned} \min_{\mathbf{x}} \quad & \mathbf{c}^T \mathbf{x} \\ \text{s.t.} \quad & \mathbf{A} \mathbf{x} \geq \mathbf{b}, \end{aligned} \tag{4.1}$$

where  $\mathbf{x} \in \mathbb{R}^N$  collects the unknown coefficients and  $\mathbf{c}, \mathbf{b} \in \mathbb{R}^N$  and  $\mathbf{A} \in \mathbb{R}^{N \times N}$  are known terms. The inequality constraint in (4.1) can be written as:

$$\mathbf{s} = \mathbf{A} \mathbf{x} - \mathbf{b} \geq 0, \tag{4.2}$$

where  $\mathbf{s} \in \mathbb{R}^N$  collects the slack variables. Therefore, the optimization problem becomes

$$\begin{aligned} \min_{\mathbf{x}} \quad & \mathbf{c}^T \mathbf{x} \\ \text{s.t.} \quad & \mathbf{s} - (\mathbf{A} \mathbf{x} - \mathbf{b}) = 0 \\ & \mathbf{s} \geq 0, \end{aligned} \tag{4.3}$$

so the inequality constraint has been transformed to an equality constraint at the expense of guarantee that  $\mathbf{s} \geq 0$ .

### 4.1.1 Objective function formulation

The current-based optimization problem described in the previous chapter aims to minimize a function containing several (local) inequality constraints, which are managed through the ramp function. This makes the objective function piecewise fourth-degree polynomial and therefore the linesearch, i.e. the minimization of the function along the direction dictated by  $\mathbf{p}$  (see App. C), is performed iteratively. To overcome this problem, an attempt was made by introducing slack variables to address the inequality constraints.

Let us consider, for the sake of brevity, the objective function related to the realizability of the MTS antenna:

$$f(\mathbf{l}) = w_{act} \sum_{i=1}^{N_c} \rho_i^{act}(\mathbf{l}) + w_L^{imp} \sum_{i=1}^{N_c} \rho_{Li}^{imp}(\mathbf{l}) + w_U^{imp} \sum_{i=1}^{N_c} \rho_{Ui}^{imp}(\mathbf{l}) + w_{scal} \sum_{i=1}^{N_c} \rho_i^{scal}(\mathbf{l}). \quad (4.4)$$

Active power and scalarity terms are expressed as equality constraints, while reactance bounds are employed with the ramp functions. In this particular case, impedance constraints are expressed in terms of power density as function of the RWG current coefficients  $\mathbf{l}$ :

$$X_{Li} \mathcal{J}_i(\mathbf{l}) \leq \mathcal{Q}_i(\mathbf{l}) \quad (4.5)$$

$$X_{Ui} \mathcal{J}_i(\mathbf{l}) \geq \mathcal{Q}_i(\mathbf{l}), \quad (4.6)$$

where  $\mathcal{J}_i(\mathbf{l})$ ,  $\mathcal{Q}_i(\mathbf{l})$  are power densities averaged over the area  $A_i$  of the  $i$ -th mesh cell  $S_i$

$$\mathcal{J}_i(\mathbf{l}) = \frac{1}{A_i} \iint_{S_i} |\mathbf{J}(\mathbf{l})|^2 dS \quad (4.7)$$

$$\mathcal{Q}_i(\mathbf{l}) = \frac{1}{A_i} \text{Im} \left\{ \iint_{S_i} \mathbf{E} \cdot \mathbf{J}^*(\mathbf{l}) dS \right\}. \quad (4.8)$$

Quantities in (4.7)-(4.8) are functions of the current coefficients through the local Gram matrix computed with RWG basis and testing functions. Conditions outlined in (4.5)-(4.6) can be restated by introducing  $N_c$  slack variables for the lower reactance bounds and  $N_c$  slack variables for the upper bounds as:

$$|s_{Li}^{imp}|^2 + X_{Li} \mathcal{J}_i(\mathbf{l}) - \mathcal{Q}_i(\mathbf{l}) = 0, \quad (4.9)$$

$$|s_{Ui}^{imp}|^2 + \mathcal{Q}_i(\mathbf{l}) - X_{Ui} \mathcal{J}_i(\mathbf{l}) = 0, \quad (4.10)$$

where  $s_i \in \mathbb{C}$ . The impedance functionals of (4.4) becomes:

$$\rho_{Li}^{imp}(\mathbf{l}, s_{Li}^{imp}) = (|s_{Li}^{imp}|^2 + X_{Li} \mathcal{J}_i(\mathbf{l}) - \mathcal{Q}_i(\mathbf{l}))^2 = (|s_{Li}^{imp}|^2 + \Psi_{Li}^{imp}(\mathbf{l}))^2, \quad (4.11)$$

$$\rho_{Ui}^{imp}(\mathbf{l}, s_{Ui}^{imp}) = (|s_{Ui}^{imp}|^2 + \mathcal{Q}_i(\mathbf{l}) - X_{Ui} \mathcal{J}_i(\mathbf{l}))^2 = (|s_{Ui}^{imp}|^2 + \Psi_{Ui}^{imp}(\mathbf{l}))^2, \quad (4.12)$$

where  $s_i$  will act as extra optimization variables.

### 4.1.2 Gradient and linesearch

Now that the objective function is formulated, the gradient must be computed with respect to the current and to the extra slack variables.

$$\begin{aligned}\tilde{\nabla}_1 \rho_{U_i}^{imp} &= 2(|s_{L_i}^{imp}|^2 + \Psi_{L_i}^{imp}(\mathbf{l})) \tilde{\nabla} \Psi_{L_i}^{imp}(\mathbf{l}), \\ \tilde{\nabla}_1 \rho_{U_i}^{imp} &= 2(|s_{U_i}^{imp}|^2 + \Psi_{U_i}^{imp}(\mathbf{l})) \tilde{\nabla} \Psi_{U_i}^{imp}(\mathbf{l}),\end{aligned}\tag{4.13}$$

where  $\tilde{\nabla} \Psi_{L_i}^{imp}(\mathbf{l})$  and  $\tilde{\nabla} \Psi_{U_i}^{imp}(\mathbf{l})$  are already computed for the gradient of the original objective function. About the complex gradient with respect to the slack variable, one can notice that  $i$ -th variable  $s_i$ , counts only for the  $i$ -th functional, i.e. one must compute the complex derivative of  $\rho_i$  only with respect to its counterpart:

$$\frac{\tilde{\partial} \rho_i}{\partial s_i} = 2(|s_i|^2 + \Psi_i) \frac{\tilde{\partial} |s_i|^2}{\partial s_i}.\tag{4.14}$$

Here, one must consider that for a given function  $h(z) : \mathbb{C} \rightarrow \mathbb{C}$ , with  $z = z' + jz''$ , the partial derivative of  $h$  with respect to  $z$  is:

$$\frac{\tilde{\partial} h}{\partial z} = \frac{1}{2} \left( \frac{\partial h}{\partial z'} + j \frac{\partial h}{\partial z''} \right),\tag{4.15}$$

which can be generalized into the definition of the complex gradient:

$$\tilde{\nabla} h(\mathbf{z}) = \frac{1}{2} (\nabla' h(\mathbf{z}', \mathbf{z}'') + j \nabla'' h(\mathbf{z}', \mathbf{z}'')), \tag{4.16}$$

where  $\nabla'$  and  $\nabla''$  are gradients with respect to the real and to the imaginary part of  $\mathbf{z}$  respectively.

Therefore, (4.14) becomes:

$$\frac{\tilde{\partial} \rho_i}{\partial s_i} = 2(|s_i|^2 + \Psi_i) s_i \tag{4.17}$$

and the gradient of the objective function with respect to the slack variables can be computed with:

$$\tilde{\nabla}_s f = 2w \begin{bmatrix} |s_1|^2 + \Psi_1 \\ |s_2|^2 + \Psi_2 \\ \vdots \\ |s_{N_c}|^2 + \Psi_{N_c} \end{bmatrix} \odot \begin{bmatrix} s_1 \\ s_2 \\ \vdots \\ s_{N_c} \end{bmatrix} \tag{4.18}$$

where the previous expression, for the sake of brevity, only considers one single set of slack variables (e.g those introduced for the lower reactance bounds). It is worth

mentioning that, since the array  $(|s_1|^2 + \Psi_1, \dots, |s_{N_c}|^2 + \Psi_{N_c})^\top$  in (4.18) is already stored in memory, as it is used for the gradient computation with respect to  $\mathbf{l}$  (see (4.13)), the gradient with respect to the slack variables can be computed without a significant computational effort.

In order to perform the linesearch procedure, the objective function must be written in terms of the step length  $\alpha$  as:

$$f(\alpha) = f(\mathbf{l}_0 + \alpha \mathbf{p}, \mathbf{s}_0 + \alpha \mathbf{s}_p). \quad (4.19)$$

This is still a simple task, because slack variables show in the functionals in the form of the magnitude squared, indeed:

$$|s_i|^2 = s_i s_i^* = (s_i^0 + \alpha s_i^p)(s_i^0 + \alpha s_i^p)^* = |s_i^0|^2 + \alpha 2\text{Re}\{s_i^0 s_i^p\} + \alpha^2 |s_i^p|^2, \quad (4.20)$$

therefore, collecting also the current coefficients, the minimum of the polynomial can be computed in closed form.

### 4.1.3 Convergence

As demonstrated, the introduction of slack variables allows to avoid the use of ramp functions for satisfying inequality constraints. However, the number of optimization variables grows significantly due to the local nature of the constraints. To verify the performance of the proposed modification, a metasurface antenna with diameter equal to  $6\lambda_0$  has been used as test and the design has been carried out minimizing both the original objective function (with ramp functions) and the one employing slack variables, with the same initial conditions and over an equal number of iterations. The proposed structure has been meshed with  $N_c = 2047$  triangular cells and the sought current has been expanded with  $N = 4812$  RWG basis functions. Just considering the inequality constraints associated with reactance bounds,  $2N_c$  slack variables must be employed to properly express the objective function. This aspect, while not computationally penalizing as observed, results in a slowdown of the convergence of the minimization algorithm, as evident from Figure 4.1.

For this reason, the optimization strategy proposed in the following will refer to the problem in its original form, namely where the inequality constraints are managed through ramp functions.

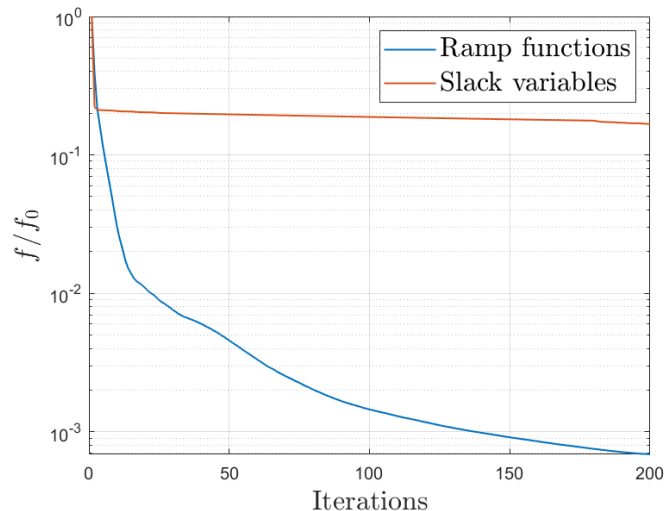


**Figure 4.1:** Convergence plot of the optimization performed over 200 iterations: optimization function expressed with ramp function versus slack variables.

## 4.2 Multi-objective optimization problem: the weighted sum method

The standard form of a multi-objective optimization problem can be simply derived from the single-objective one considering the function to minimize as an array of several optimization functions:

$$\begin{aligned}
 \min_{\mathbf{x}} \quad & \mathbf{F}(\mathbf{x}) = [f_1(\mathbf{x}), f_2(\mathbf{x}), \dots, f_K(\mathbf{x})]^T \\
 \text{s.t.} \quad & g_j(\mathbf{x}) \leq 0 && j = 1, \dots, m \\
 \text{s.t.} \quad & h_i(\mathbf{x}) = 0 && i = 1, \dots, p,
 \end{aligned} \tag{4.21}$$

where  $\mathbf{x} \in \mathbb{R}^N$  is the design (or decision) array,  $K$  is the number of optimization functions,  $m$  the number of inequality constraints and  $p$  the number of equality constraints.

From (4.21) it is clear that  $\mathbf{x}$  and  $\mathbf{F}$  have different dimension space and in particular, each solution of the decision space ( $\mathbb{R}^N$ ) maps a single value in the objective space ( $\mathbb{R}^K$ ), while the inverse mapping is not unique [10]. Furthermore, it is trivial to understand that except for the case  $K = 1$ , which collapses in the single-objective optimization problem, values in the decision space that minimize a single function will conflict with others, so an improvement of one function may lead to a deterioration of the others. Therefore, there is no a single optimal solution, but a set of solutions which represents a trade-off among all the objective functions.

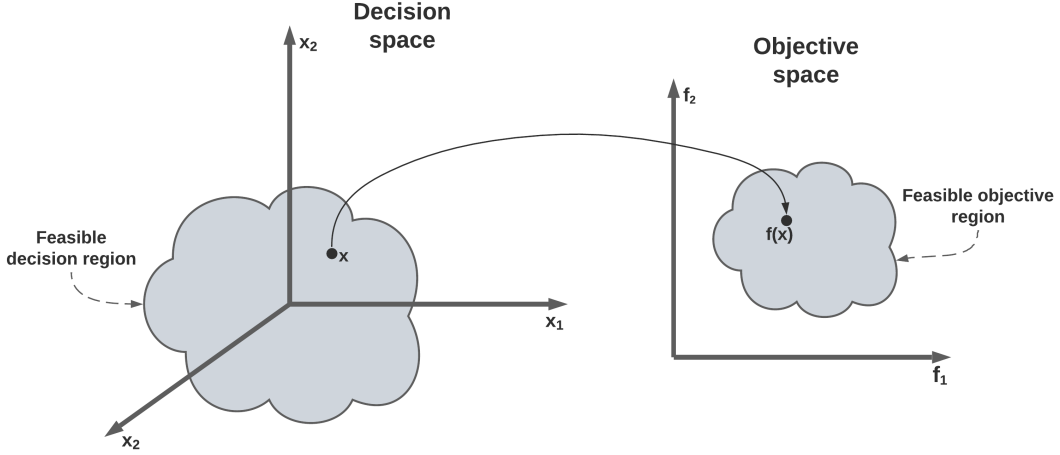


**Figure 4.2:** Mapping between the decision space ( $\mathbb{R}^3$ ) and objective space ( $\mathbb{R}^2$ ).

Figure 4.2 shows the mapping between the decision space and the objective space: the portion of the objective space in grey represents the values obtained in the objective space considering the *feasible* solutions, i.e., those that satisfy the constraints in (4.21), taking into account the possible trade-offs among the objective function values. The feasible region, however, is populated by non-optimal values of the objective function  $F$ , meaning values that are neither optimal for  $f_1$  nor for  $f_2$ . On the other hand, outside the feasible region, particularly near the origin of the reference system for the objective space, it is possible to distinguish a region known as the unfeasible region, which is therefore unreachable by any set of design variables [11]. The boundary between the objective feasible region and the objective unfeasible region is called Pareto front and it is made by a set of non-dominated solutions, meaning that no solution is dominated by another, yet at the same time they are better than any other solutions in the feasible region [12].

In accordance with the explanation presented above, the strict definition of Pareto front is given [13]:

**Definition 4.2.1** A solution  $x^* \in X_f$ , where  $X_f$  is the feasible solutions set, is a Pareto-optimal solution if:

$$\nexists x \in X_f : x \succ x^*. \quad (4.22)$$

With the notation  $x \succ x^*$  it is customary to indicate that  $x$  *dominates*  $x^*$ , that is to say  $x$  is equal or superior to  $x^*$  among all objective function values and it is better than  $x^*$  for at least one objective function value [14].

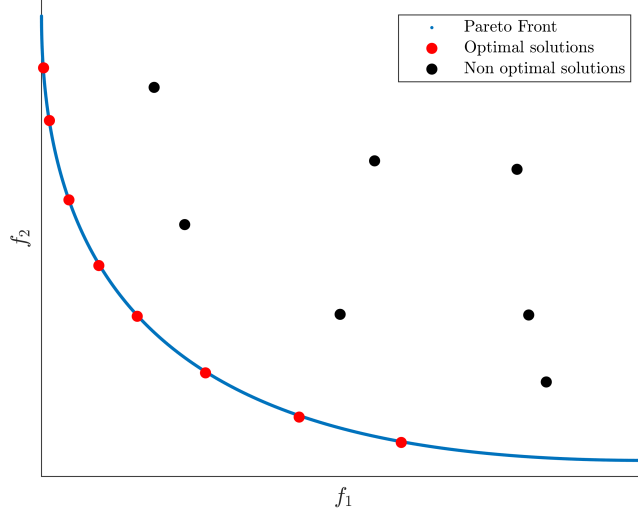


**Figure 4.3:** [15] Representation of the Pareto front (blue line), optimal (red dots) and non-optimal (black dots) solutions.

**Definition 4.2.2** All Pareto-optimal solutions constitute the Pareto-optimal set  $P^*$ :

$$P^* \triangleq \{ \mathbf{x}^* \mid \nexists \mathbf{x} \in X_f : \mathbf{x} \succ \mathbf{x}^* \}. \quad (4.23)$$

**Definition 4.2.3** The surface obtained by combining all the objective functions corresponding to the set  $P^*$  is called Pareto front  $PF^*$ :

$$PF^* \triangleq \{ \mathbf{F}(\mathbf{x}^*) = [f_1(\mathbf{x}^*), f_2(\mathbf{x}^*), \dots, f_K(\mathbf{x}^*)]^T \mid \mathbf{x}^* \in P^* \}. \quad (4.24)$$

One of the most common ways to deal with multi-objective optimization problems is by using the weighted sum method. The array of objective functions  $\mathbf{F}(\mathbf{x})$  in (4.21) can be substituted by a scalar objective function made by a weighted sum of all the components of  $\mathbf{F}(\mathbf{x})$ :

$$U(\mathbf{x}) = \sum_{k=1}^K w_k f_k(\mathbf{x}). \quad (4.25)$$

$U(\mathbf{x})$  is usually called *utility function*. With this approach the (4.21) is organized into a simpler single-objective problem, with the possibility of inheriting the same optimization techniques.

The reason why the optimization problem described in 3 has been organized using a single scalar function as (4.25) is that in the design of a metasurface antenna there are not many functions one would optimize in the literal sense, while the

number of constraints is in general huge, since each of them must refer to a single mesh-cell. Typically, the structure constituting the antenna must be lossless, hence one can address the problem minimizing the the real part of the active power, but, for the aforementioned reasons, it would be impractical. Moreover, the real part of the active power is not something one wants to *minimize*, but a quantity that must be equal to zero for each cell. Therefore, since one would keep the surface reactance and the radiated field (co- and cross- polarization) between given boundaries and obtain a lossless structure, the *optimal* design of a metasurface antenna allows every possible solutions, provided that the above mentioned constraints are satisfied. For these reasons, the problems entailed by the design of these kinds of antennas are more *feasibility problems* rather than optimization ones.

### 4.3 Meaning of the weights

Considering the (4.25),  $w_k$  with  $k = 1, \dots, K$  represents the weight to be assigned to each objective function. As explained in the previous section, the weighted sum method allows to restate the multi-objective optimization problem as a single objective function. The first problem that arises while employing this method is that the scalar utility function  $U(\mathbf{x})$  is not necessarily equivalent to the  $F(\mathbf{x})$  of (4.21), because, intuitively, since the choice of the weights can be arbitrary, also the solution  $\mathbf{x}$  can be different [16].

In this section, the conceptual meaning of weights and their impact on the solution of an optimization problem will be addressed.

As the name suggests, the weights to assign to each objective function can reflect the importance of a specific goal. In many commercial CAD softwares for electronic design one can set a multi-objective optimization choosing the weights so that one goal will be reached sooner than the others. However, not all design problems have priority goals than others that can be overlooked, but quite the opposite: generally it is not possible to distinguish a preference. As suggested by [17], let us consider as an example the optimization of two functions:

$$\begin{aligned} \min_{\mathbf{x}} \quad & f_1(\mathbf{x}) = 10(x_1 - 1)^2 + (3x_2 - 2)^2 \\ & f_2(\mathbf{x}) = (x_1 - 3)^2 + (x_2 - 2.5)^2 \end{aligned} \tag{4.26}$$

with the design array  $\mathbf{x} = [x_1, x_2] \in \mathbb{R}^2$  and  $x_{1,2} \in [0,4]$ .

Moreover, let us consider that the designer cannot distinguish any priority: both functions must be minimized in the same way. When  $f_1$  is minimized,  $f_2 = 7.36$ , while when  $f_2$  is minimized,  $f_1 = 70.25$ . These two functions can be shrunk into one to be minimized using the weighting sum method: let us assign  $w_1 = w_2 = 1$ , the result, computed with one of the function in the Matlab suite, is  $[1.18, 0.85] \rightarrow [0.63, 6.03]$ .

Evaluating both functions for each possible value of  $\mathbf{x}$  in the criterion space, one can appreciate that  $f_1$  has a range between zero and 190,  $f_2$  between 0 and 15.25. Since the range of  $f_1$  is much larger to the range of  $f_2$ , it can be natural to assign  $w_1 = 1$  and  $w_2 = 2$ , in order to compensate their magnitude. The result is:  $[1.334, 1] \rightarrow [2.11, 5.03]$ , so this solution does not dominate the previous one, as only  $f_2$  assumes a lower value. Even if the weights are assigned trying to equalize the magnitudes of  $f_1$  and  $f_2$ , so  $w_1 = 0.08$  and  $w_2 = 0.92$ , the result is  $[2.07, 1.69] \rightarrow [36.67, 0.22]$ .

From this example, it is possible to conclude that assigning weights in such a way that reflects the magnitudes of single functionals, as also experimented for the Current-Based Optimization algorithm, does not lead to improvements, or at least not always. It is also worth mentioning that very often weights are chosen a-posteriori, based on repeated optimization: this approach can be inefficient for the user aiming to pursue the optimization, especially when dealing with complex scenarios, i.e. when many functions and unknowns are involved. It is worth to analyze the meaning of the weights from a mathematical standpoint.

Considering the (4.25), weights represent the gradient of the function  $U$  with respect to  $\mathbf{F}$ . In fact, if one simplifies the expressions in the case of only two objective functions, so that  $\mathbf{F}(\mathbf{x}) = [f_1(\mathbf{x}), f_2(\mathbf{x})]$  and  $U(\mathbf{x}) = w_1 f_1(\mathbf{x}) + w_2 f_2(\mathbf{x})$ :

$$\nabla_{\mathbf{F}} U = \begin{Bmatrix} \frac{\partial U}{\partial f_1} \\ \frac{\partial U}{\partial f_2} \end{Bmatrix} = \begin{Bmatrix} w_1 \\ w_2 \end{Bmatrix} \quad (4.27)$$

The previous expression means that by choosing a set of weights one gets the direction of decreasing  $U$  values, represented by  $-\nabla_{\mathbf{F}} U$ , which allows to find a the  $U$ -function contours tangent to the pareto optimal set [17]. The figure 4.4 offers a graphical representation of the gradient and of the  $U$ -function contours in the case of two objective functions.

For the reason explained above, the choice of the weights is a critical operation due to the fact that with different set of weights it is possible to "explore" the entire feasibility space, and especially because with a specific set, it is possible to point towards any solution on the Pareto front. Moreover, among all possible solutions on the Pareto front, often the designer chooses the so-called *knee point* (shown in Figure 4.5), that is the one which minimizes the distance between the Pareto curve and the *utopia point*, for which all objective functions are minimized and in general not feasible [18].

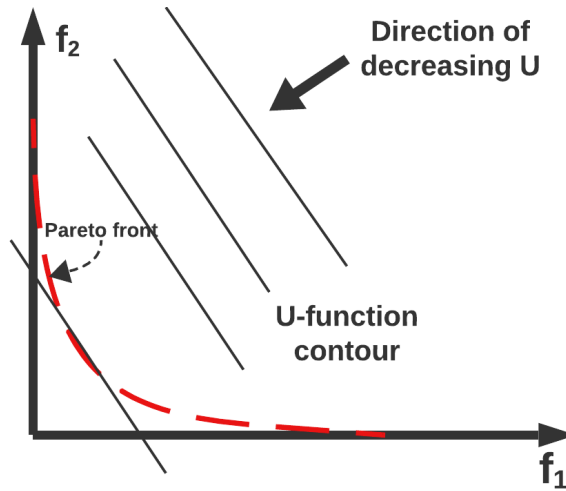


**Figure 4.4:** Graphical interpretation of the weights in a  $2d$ -space: black solid line are the  $U$ -function contour tangent to the Pareto front (red dashed curve). The direction of decreasing  $U$  pointed by the arrow is dictated by the weights.

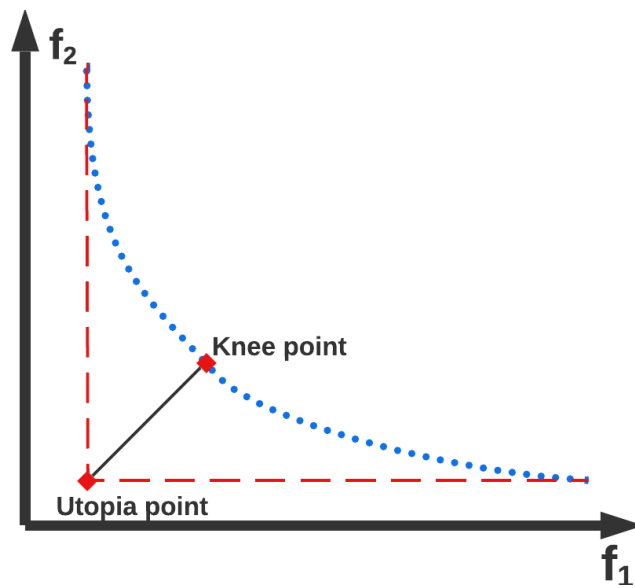


**Figure 4.5:** The knee point on the Pareto front (blue dots) minimizes the distance from the utopia point.

## 4.4 Adaptive weight scheme

In this section, the basic algorithm for determining the optimal set of weights will be formulated, specifically tailored to the case of the Current-Based Optimization

Algorithm described in chapter 3 and it is presented as a way to tackle the non-convexity of the objective function. Although this re-weighting algorithm is described quantitatively and mathematically for the specific case, it is conceptually feasible for any multiobjective optimization problem dealt with through the weighted sum method.

#### 4.4.1 Concept of hyperplane

The  $U$ -function contours described in the previous section (see Figure 4.4), for the specific case of only two objective functions, are lines oriented in the orthogonal direction of the gradient of  $U$  with respect to  $\mathbf{F}$  and tangent to the Pareto front. The  $n$ -dimension generalization of that lines can be obtained through the concept of hyperplane.

An hyperplane is a subspace of one dimension less than its ambient space: for a 2-dimensional space, the hyperplane is a 1-dimensional line (see Figure 4.4), for a 3-dimensional space, the hyperplane is a 2-dimensional plane. The hyperplane can be described in Cartesian coordinates with the following linear equation:

$$a_1x_1 + a_2x_2 + \dots + a_nx_n = 1, \tag{4.28}$$

in which  $a_i$  is the hyperplane coefficient. By comparison with the previous equation, it is possible to write the expression of the  $U$ -function in the form of hyperplane equation as follows:

$$w_1f_1 + w_2f_2 + \dots + w_nf_n = 1, \tag{4.29}$$

where  $(w_1, \dots, w_n)$  corresponds to the normal to the hyperplane.

The mathematical analogy between the hyperplane equation and the utility function can be used to describe the re-weighting procedure. The goal of the algorithm is to set the weights in such a way the  $U$ -function contour points towards the knee point of the Pareto front. To do so, let us suppose that during the minimization of the objective functions, two Pareto optimal solutions are obtained (in the case of only two objective functions): from them it is possible to construct the hyperplane and find the new set of weights evaluating the normal. Then, minimizing the functions with new weights, a new solution on the Pareto front is obtained (see Figure 4.6) [19]. This type of procedure that updates the weights to find new solutions on the Pareto front can be applied iteratively in order to obtain a minimum.

Figure 4.6 shows an example case and, in fact, the solutions for which the line is constructed determine a normal, thus a set of weights, which points toward the knee point as desired. By the way, the chance to head towards that point is strongly dependent on the solutions used and this aspect will be addressed in the following.

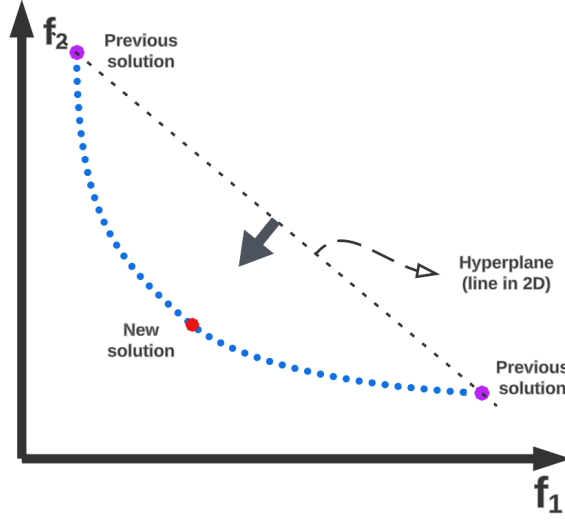


**Figure 4.6:** Hyperplane in 2-dimensional space constructed from two anchor points (previous solutions): the normal unit vector to the hyperplane points towards the knee point (new solution).

#### 4.4.2 Algorithm formulation

In order for the re-weighting algorithm to be perfectly integrated, and without computational efficiency losses, with the Current-Based Optimization Algorithm, it is necessary to start from how the latter has been algebraically formulated.

The generic expression of one single objective function is:

$$f_i(\mathbf{x}) = (\mathbf{x}^H \mathbf{A}_i \mathbf{x} + \mathbf{x}^H \mathbf{b}_i + c_i)^2 \quad (4.30)$$

with  $\mathbf{A} \in \mathbb{C}^{N \times N}$  and symmetric,  $\mathbf{b} \in \mathbb{C}^N$ ,  $c \in \mathbb{C}$  and  $\mathbf{x} \in \mathbb{C}^N$ , in which  $N$  is the number of unknowns. The index  $i \in [0, K]$ , where  $K$  is the number of objective functions.

As explained in 3, the minimization of the entire objective function is carried out with the non-linear conjugate gradient algorithm, which involves the linesearch procedure. The linesearch process implies the minimization of the function  $f(\mathbf{x}) = f(\mathbf{x}_0 + \alpha \mathbf{p})$ , where  $\mathbf{x}_0$  is the solution at the starting point of the iterative method,  $\mathbf{p}$  is the update direction and  $\alpha$  is the coefficient to be found. Therefore, each  $f_i$  in 4.30 must be made explicit with respect to  $\alpha$ :

$$f_i(\mathbf{x}_0 + \alpha \mathbf{p}) = (Q_i^0 + \alpha Q_i^1 + \alpha^2 Q_i^2)^2, \quad (4.31)$$

where:

$$Q_i^0 = \mathbf{x}_0^H \mathbf{A}_i \mathbf{x}_0 + \mathbf{x}_0^H \mathbf{b}_i + c_i \quad (4.32)$$

$$Q_i^1 = \mathbf{x}_0^H \mathbf{A}_i \mathbf{p} + \mathbf{p}^H \mathbf{A}_i \mathbf{x}_0 + \mathbf{p}^H \mathbf{b}_i \quad (4.33)$$

$$Q_i^2 = \mathbf{p}^H \mathbf{A}_i \mathbf{p}. \quad (4.34)$$

In the previous expressions, the apex refers to the order of the coefficient, which can be assembled as:

$$\begin{aligned} \mathbf{Q}^0 &= [\dots, Q_i^0, \dots]^T, \\ \mathbf{Q}^1 &= [\dots, Q_i^1, \dots]^T, \\ \mathbf{Q}^2 &= [\dots, Q_i^2, \dots]^T, \end{aligned} \quad (4.35)$$

At this point, the Pareto front with respect to the coefficient  $\alpha$  can be obtained. Now, one needs to search the solutions on the Pareto front that can be used as points to construct the hyperplane. Since all objective functions are made by a 4<sup>th</sup> order polynomial expression, a relatively simple task is to apply the derivative to each objective functions and find  $\alpha_i^*$  by imposing them equal to zero.

$$f'_i(\alpha_i^*) = \left. \frac{df_i(\alpha)}{d\alpha} \right|_{\alpha_i^*} = 0$$

The linesearch algorithm has already a procedure which finds the stationary point of fourth-degree polynomials starting from the coefficients, therefore no additional procedures are needed to perform this task.

In this way, a  $K$ -by- $K$  matrix can be constructed:

$$\mathbf{P} = \begin{bmatrix} f_1(\alpha_1^*) & f_2(\alpha_1^*) & \dots & f_K(\alpha_1^*) \\ f_1(\alpha_2^*) & f_2(\alpha_2^*) & \dots & f_K(\alpha_2^*) \\ \vdots & \vdots & \ddots & \vdots \\ f_1(\alpha_K^*) & \dots & \dots & f_K(\alpha_K^*) \end{bmatrix} \quad (4.36)$$

which is made by points known in the literature as *anchor points*. An example of anchor points in the case of  $K = 2$  is shown in Figure 4.6.

These points, in addition to being computationally straightforward to calculate - since, as previously mentioned, they only involve the derivative of a fourth order polynomial - ensure that the knee point is located between them if the Pareto front has a convex shape. Therefore, the normal to the hyperplane constructed from anchor points will head towards the knee point, or very close to it.

Defining the coefficients of the hyperplane as an array:

$$\mathbf{n} = [n_1, n_2, \dots, n_K]^T$$

The normal to the hyperplane can be obtained solving with respect to  $\mathbf{n}$  the following linear systems which involves the matrix  $\mathbf{P}$  in (4.44):

$$\mathbf{P} \mathbf{n} = [1, 1, \dots, 1]^T \quad (4.37)$$

The set of weights is obtained by normalizing  $\mathbf{n}$ :

$$\mathbf{w} = \frac{\mathbf{n}}{\|\mathbf{n}\|} \quad (4.38)$$

Then with the set of weights in the form of an array  $\mathbf{w} = (w_1, w_2, \dots, w_K)^\top$ , the new objective function is obtained by:

$$\begin{aligned} \mathbf{w} \odot \mathbf{Q}^0 \\ \mathbf{w} \odot \mathbf{Q}^1 \\ \mathbf{w} \odot \mathbf{Q}^2 \end{aligned} \quad (4.39)$$

Now, by using the linesearch procedure with this set of weight, a new stationary point can be computed: with the resulting coefficient  $\alpha^{new}$ , a new point on the Pareto front is obtained, that is  $(f_1(\alpha^{new}), f_2(\alpha^{new}), \dots, f_K(\alpha^{new}))$ . From this point on, the optimization proceeds like gradient descent algorithms, therefore, the new starting point and the update direction must be computed:

$$\mathbf{x}_0^{new} = \mathbf{x}_0 + \alpha^{new} \mathbf{p} \quad (4.40)$$

$$\mathbf{p}^{new} = -\tilde{\nabla}_{\mathbf{x}} U \quad (4.41)$$

The complex gradient can be computed considering that:

$$U(\mathbf{x}) = \sum_{i=1}^K w_i f_i(\mathbf{x})$$

And taking into account the 4.30:

$$\tilde{\nabla}_{\mathbf{x}} U = \sum_{i=1}^K 2w_i (\mathbf{x}^H \mathbf{A}_i \mathbf{x} + \mathbf{x}^H \mathbf{b}_i + c_i) \tilde{\nabla}_{\mathbf{x}} (\mathbf{x}^H \mathbf{A}_i \mathbf{x} + \mathbf{x}^H \mathbf{b}_i + c_i)$$

Which becomes:

$$\tilde{\nabla}_{\mathbf{x}} U = \sum_{i=1}^K 2w_i (\mathbf{x}^H \mathbf{A}_i \mathbf{x} + \mathbf{x}^H \mathbf{b}_i + c_i) (\mathbf{A}_i \mathbf{x} + \mathbf{b}_i) \quad (4.42)$$

The complete algorithm is outlined in the pseudo-code Alg. 1.

---

**Algorithm 1** Hyperplane Adaptive Weight (HAW) scheme

---

**Input:**  $\mathbf{x}_0, \mathbf{p}, \mathbf{A}, \mathbf{b}, c, N_{times}$   
**Output:**  $\mathbf{x}^*$   
**for**  $i = 0 : N_{times} - 1$  **do**  
    **Compute**  $\mathbf{Q}^0, \mathbf{Q}^1, \mathbf{Q}^2$  ▷ with (4.32),(4.33),(4.34)  
    **Compute**  $\alpha_k^*$  ▷ Using the *linesearch* procedure  
    **Compute**  $\mathbf{P}$  ▷ with (4.44)  
    **Compute**  $\mathbf{w}$  ▷ with (4.37),(4.38)  
     $\mathbf{Q}^0 \leftarrow \mathbf{w} \odot \mathbf{Q}^0$   
     $\mathbf{Q}^1 \leftarrow \mathbf{w} \odot \mathbf{Q}^1$   
     $\mathbf{Q}^2 \leftarrow \mathbf{w} \odot \mathbf{Q}^2$   
    **Compute**  $\alpha^{new}$  ▷ Using the *linesearch* procedure  
     $\mathbf{x}_{i+1} \leftarrow \mathbf{x}_i + \alpha^{new} \mathbf{p}_i$   
    **Compute**  $\tilde{\nabla}_{\mathbf{x}_i} U$  ▷ with (4.42)  
     $\mathbf{p}_{i+1} \leftarrow -\tilde{\nabla}_{\mathbf{x}_i} U$   
**end for**  
 $\mathbf{x}^* \leftarrow \mathbf{x}_{N_{times}}$

---

In the next section, a minimization example is proposed, which shows graphically how the algorithm works.

### 4.4.3 Example

In this section, a simple example made by 2 objective functions (for graphical reasons) and 10 unknowns is proposed.

For the sake of simplicity,  $\mathbf{A}, \mathbf{b}, c, \mathbf{x}_0, \mathbf{p}$  are real quantities and randomly generated. As detailed in the previous section, the minimization proceeds in the direction pointed by the arrow, which is computed from the norm to the straight line passing through the two anchor points (see Figure 4.7). Stopping the optimization at the sixth iteration (Figure 4.7f), one can appreciate how the function has been minimized by considering the value of the Euclidean norm in a K-dimension space:

$$d = \sqrt{\sum_{i=1}^K (f_i(\mathbf{x}^*))^2} \quad (4.43)$$

In this way, if the value of  $d$  is close to zero, it means that all the functions are minimized. On the other hand, since the the Euclidean norm is influenced by the highest term in (4.43), it is enough that just one objective function is not minimized to ensure that  $d$  assumes high values. When dealing with a small number of unknowns ( $< 100$ ) and few objective functions ( $< 5$ ) the performance of this algorithm is comparable, in most cases, to those already available in the Matlab

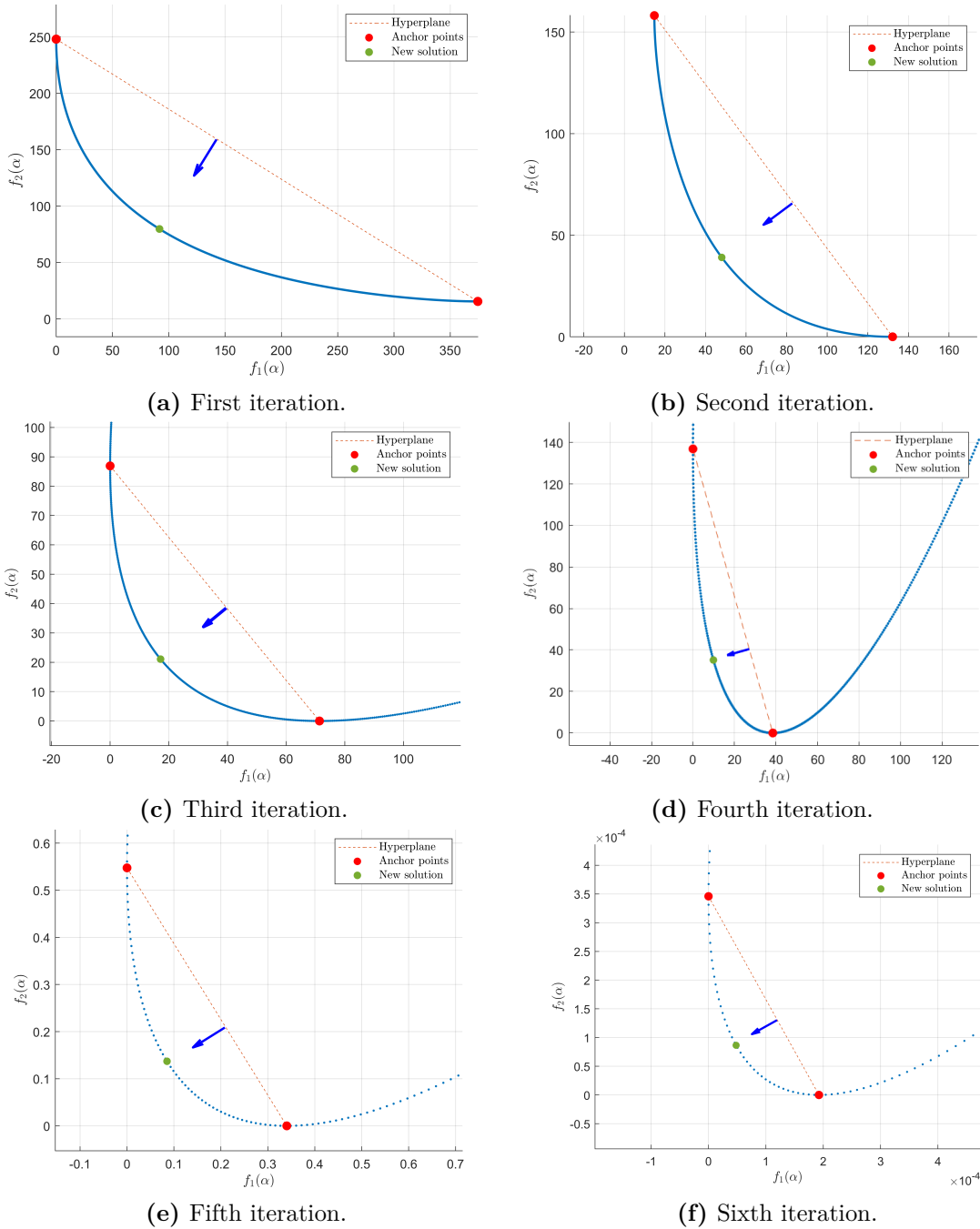


**Figure 4.7:** Graphical representation of the HAW algorithm: sky-blue dots represent the Pareto front while the direction of the blue arrow is dictated by the weights computed using (4.37-4.38).

suite. However, when the comparison is made using a realistic example, involving thousands of variables and about ten objective functions, the existing algorithms, which of course are general purpose, become unusable. Instead, the proposed algorithm is able to achieve good results in reasonable time even under particularly heavy workloads.

## 4.5 Hyperplane Adaptive Weighting scheme

Once the re-weighting scheme based on the concept of the hyperplane has been defined, one just needs to integrate it in the Current-Based Optimization Algorithm. The algorithm outlined in Alg. 1, as shown, can minimize an arbitrary number of objective functions with an arbitrary number of unknowns.

It is worth mentioning that when the optimization of MTS antennas is considered, the Euclidian norm cannot be considered a consistent metric in the understanding of the quality of the result. The reason is that objective functions like those associated with the losses of the MTS will never be equal to zero, as a residual amount of power dissipation, in general, will always be present. Therefore, a lower value of the Euclidian norm is not always an index of good quality of the design

As principle, Alg. 1 can theoretically substitute the non-linear conjugate gradient algorithm 4, but, for several reasons, the final algorithm that optimizes a metasurface antenna is made by an hybrid version of the NLCG and the HAW.

These reasons are basically three:

- Null determinant of  $\mathbf{P}$ : the matrix definite in (4.44) can be made by column of all elements equal to zero; since the determinant is null, the matrix is not invertible and the the linear systems in (4.37) cannot be solved. These columns of all zeros are generally a result of objective functions associated with constraints defined via ramp functions. For instance, if the impedance value evaluated in a certain iteration adheres to the constraint set by the designer, then the value of the objective function associated with impedance will be equal to zero, and consequently, so will its derivative.

A way to overcome this problem is to remove the null columns (and their corresponding rows) from the matrix, resulting in a  $K' \times K'$  square matrix.

$$\begin{bmatrix} f_1^1 & f_2^1 & \dots & f_K^1 \\ f_1^2 & f_2^2 & \dots & f_K^2 \\ \vdots & \vdots & \ddots & \vdots \\ f_1^K & \dots & \dots & f_K^K \end{bmatrix} \rightarrow \begin{bmatrix} f_1^1 & f_2^1 & \dots & f_{K'}^1 \\ f_1^2 & f_2^2 & \dots & f_{K'}^2 \\ \vdots & \vdots & \ddots & \vdots \\ f_1^{K'} & \dots & \dots & f_{K'}^{K'} \end{bmatrix} \quad (4.44)$$

Where  $f_k^k$  is a compact form for  $f_k(\alpha_k^*)$  and the index  $k = [1, \dots, K'] \subseteq$

$[1, \dots, K]$ .

The resulting matrix has no more null determinant, therefore it can be used to compute the normal and then the new set of weights.

Regarding the removed objective functions, the weight assigned to them in the weighted sum can be chosen either equal to 1 or can be set to the value from the previous iteration. There is not a strong theoretical reason for choosing one path over the other, but it has been observed that the latter yields better and more stable results.

- Near singular matrix: although one can easily remove the zero-elements columns and avoid the determinant to be exactly equal to zero, the matrix  $\mathbf{P}$  can still be near singular. In the present case, it may happen that two or more rows of  $\mathbf{P}$  are coincident within a certain tolerance value. This aspect ensures that the norm to the hyperplane, evaluated from the solution of a linear system, is not unique, but numerically inaccurate and the resulting error can lead to non-exact results or even to the divergence of the solution.
- Non convex Pareto front: as detailed in the previous section, the anchor points ensure that the knee point is in between them, provided that the Pareto front has a convex shape. In some cases, the Pareto front could be non convex, as shown in Figure 4.8 with two objective functions, therefore the knee point is not found anymore in the direction dictated by the norm. When more than two objective functions are involved it is not simple to understand the shape of the Pareto front, therefore, understanding its convexity (or concavity) requires further studying.

Although the problem of the null determinant can be numerically solved as explained above, the same cannot be done, under the present conditions, with the other two.

The optimization starts by choosing a number of iterations  $N_i$  for the NLCG and a number of weight update  $N_w$ , in this way, the total number of iterations for the overall optimization algorithm becomes  $N_i \times N_w$ . The NLCG performs the minimization with a default set of weights, then the HAW performs the update and the NLCG starts over again. Alternatively, one can compute the first set of weights by running the proposed method with the starting coefficient  $\mathbf{x}_0$  and then performs the minimization with the NLCG. As shown in Alg. 2, the optimal set of weights is obtained by Alg. 1, while the computation of  $\alpha_{new}$  and the solution update is computed by the NLCG (Alg. 4) .

The chosen number  $N_w$  should be not too large to avoid potential singularities of matrix  $\mathbf{P}$  leading to errors or divergences, nor too small, otherwise, the effect of re-weighting would not be as effective in optimization. Moreover, the selection of  $N_i$  should take into consideration the total number of iterations intended to

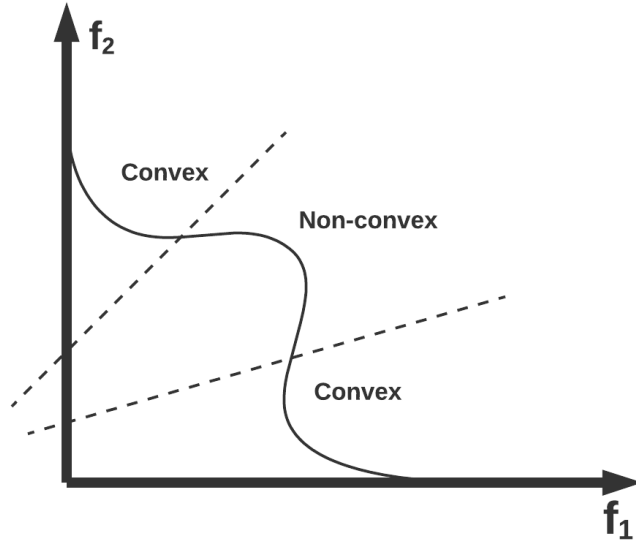


**Figure 4.8:** Pareto front in 2-dimensional space (solid line): dashed lines separate convex from non convex parts.

be performed, as well as the type and the antenna into account. Undoubtedly, a minimum of empirical investigation is required to obtain the optimum value for  $N_w$ .

In order to make this method adaptive also during the minimization of the objective function, one can monitor the value of the objective function  $U(\mathbf{x})$  during the NLCG iterations. This monitoring results to be not too heavy from a computational standpoint: the  $U$ -function is made by the weighted sum of several functions; in each of them the heaviest term is the discretization of the linear operator  $\mathbf{L}$  or  $\mathbf{R}$  (near field or far field), which can be computed only once. Therefore, if the value  $U(\mathbf{x}_i)/U(\mathbf{x}_0)$ , where  $i = 1, \dots, N_i$ , with a certain set of weights, is not varying during the algorithm, it probably means that a local minimum is almost reached and a new set of weights must be computed in order to keep exploring the solution space.

In practice, this approach can be implemented by fixing a tolerance  $\tau$  such that if:

$$\left| \frac{U(\mathbf{x}_{i+1}) - U(\mathbf{x}_i)}{U(\mathbf{x}_0)} \right| < \tau \quad (4.45)$$

for more than a certain number of iterations, the NLCG quits and a new set of weights is associated to the objective function.

---

**Algorithm 2** NLCG-HAW algorithm

---

**Input:**  $x_0$   
**Output:**  $x^*$   
**for**  $i = 0 : N_w - 1$  **do**  
    **Compute**  $U(x_i)$   
    **Compute**  $\tilde{\nabla}U$   
     $p \leftarrow -\tilde{\nabla}U$   
    **Compute**  $w_i$  ▷ with HAW (Alg. 1.)  
    **Assign**  $w_i$  to  $U$   
    **Compute**  $x_{i+1}$  ▷ with NLCG (Alg. 4),  $x_i$  as input current.  
**end for**  
 $x^* \leftarrow x_{N_w}$

---

# Chapter 5

## Numerical results

In this chapter several numerical results of optimization of metasurface antennas with different background media, dimensions, impedance constraints and radiated field specifications are reported.

### 5.1 Optimization setup

In all cases, the supporting structure of the printed metallic patches constituting the metasurface is made by a single dielectric layer and a ground plane, both infinitely extended in the  $(x-y)$  plane.

The feeding for the MTS antenna is provided through a vertical dipole placed in the centre of the structure. Its radiated field is approximated as a  $TM_0$  surface wave, whose tangential expression in cylindrical coordinates is

$$\mathbf{E} = E_0 H_1^{(2)}(\beta_{sw} \rho) \hat{\boldsymbol{\rho}}, \quad (5.1)$$

where  $E_0$  is the amplitude constant, chosen such that the power is normalized to 1W,  $H_1^{(2)}$  is the Hankel function of the second kind of order 1 and  $\beta_{sw}$  is the propagation constant of the surface wave (see App. B).

The initial current for the optimization is made by a  $\hat{\boldsymbol{x}}$ -oriented surface current constant in magnitude (see Figure 5.1). It can be shown that this current radiates broadside with linear polarization, therefore, as principle, it should not be used to create a circular polarized radiated field. It is anyway employed in order to test the robustness of the algorithm.

As explained in section 3.2, the impedance must be capacitive-only, so the optimization process requires the specification of reactance bounds. Depending on the type of substrate considered (dielectric thickness  $h$  and dielectric constant  $\epsilon_r$ , and on the desired central frequency), the reactance bounds can be different, in order to make the metasurface realizable with printed metallic patches.

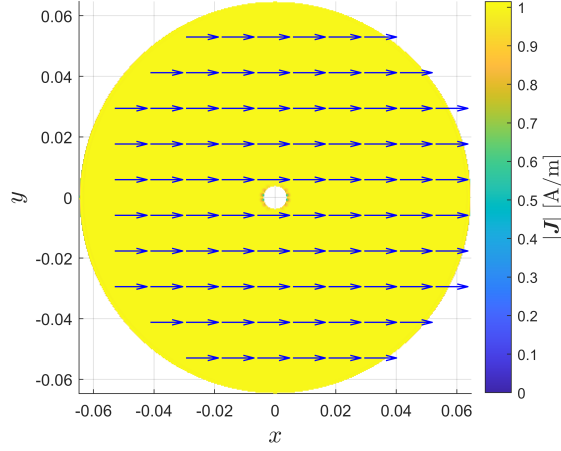


**Figure 5.1:** Starting current for circular MTS antennas: magnitude and direction.

About the radiation performance of the antenna, the target is to maximize the field magnitude ( $|\mathbf{E}|^2 = \mathbf{E} \cdot \mathbf{E}^*$ ) in the main beam, so the objective level  $M_0$  can be chosen equal to the magnitude the antenna will radiated with 100% efficiency (physical limit), but in general is set to be one or two order of magnitude lower.

The other field specifications are relative to  $F_{ref}$ , which is, for the sake of simplicity, equal to the field magnitude in the maximum angular direction.  $\Omega_{ML}$  defines the main lobe region and  $\mu_L^{co}$  is the lower relative bound for the co-polarization, i.e. the main lobe must be higher than  $(F_{ref}|_{dB} + \mu_L^{co})$  in the region  $\Omega_{ML}$ . Also the polarization of the radiated field (linear or circular) is a requirement.

The validation of the design quality passes through the evaluation of metrics such as the directivity  $D$  and the aperture efficiency  $\eta_{ap}$  (see App. A), as well as checking if the resulting radiation pattern complies with the field masks (see Figure 3.2).

## 5.2 Medium sized antenna

The first proposed numerical result is a the design of a medium sized antenna with diameter equal to  $10\lambda_0$ : this kind of geometry involves a number of cell  $N_c = 15428$  and  $N = 22991$  RWG basis function. About the realizability specifications, the chosen substrate is made by a dielectric thickness  $h$  equal to 0.508 mm, a relative dielectric constant  $\epsilon_r$  equal to 3.34 and no magnetic property ( $\mu_r = 1$ ); it allows, together with the desired frequency  $f_0 = 23$  GHz, the realization of a surface reactance bounded between  $-1000 \Omega$  and  $-100 \Omega$ . The radiated field specific in terms of radiation pattern is a pencil beam broadside shape (i.e. the main lobe must be oriented orthogonally to the aperture plane) with circular polarization.

The region of the main lobe  $\Omega_{ML}$  has been chosen equal to  $6^\circ$  (so the parameter  $\theta_{ML}$  is chosen equal to  $3^\circ$ , as it represent half of the width), while the side lobes region  $\Omega_{SL}$  starts from  $10^\circ$ . The reference level, as detailed above, will always be referred to the magnitude of the field in the main lobe, i.e.  $F_{ref} = F(\theta = 0^\circ)$ : the relative upper level for the main lobe  $\mu_U^{co}$  is trivially equal to 0 dB, while the lower bound  $\mu_L^{co} = -3$  dB. Side lobes,  $\sigma_{SL}$ , and cross-polarization,  $\sigma_{cx}$ , are respectively equal to -20 dB and -15 dB. All the simulation parameters are listed in Table 5.1

$f_0$	23 GHz
Size	$d = 10\lambda_0$
$\text{Im}\{Z\}[\Omega]$	$-1000 \div -100$
$\theta_{ML}$	$3^\circ$
$\theta_{SL}$	$10^\circ$
$\mu_L^{co}$	-3 dB
$\sigma_{SL}$	-20 dB
$\sigma_{cx}$	-15 dB

**Table 5.1:** Design parameters for a medium sized antenna with pencil beam radiation pattern.

### 5.2.1 Circular polarization

The optimization has been carried out with the standard NLCG algorithm referred in chapter 3, and the NLCG-HAW described in chapter 4. For both simulations, the starting conditions are the same and so it is for the iterations, whose number has been chosen equal to 400. Actually, for the latter implementation the number of re-weighting has been chosen equal to 4, so 100 iterations are performed with each set of weights.

The aim of this first optimization is to see how the method proposed in chapter 4 makes the design process insensible to the choice of the starting weights. As a matter of fact, the same naively choice of starting weights has been done for both methods.

It can be interesting to see numerically how the re-weighting has been performed during the optimization. In the following, the values of the functionals and the

assigned weights are reported. In Table 5.2 the generic term  $f$  has been extrapolated from (3.27)-(3.28), e.g:

$$f_{act} = \sum_{i=1}^{N_c} \rho_i^{act}(I),$$

and the first row refers to the values computed with the starting current. As can be seen, the starting current guarantees that the radiated field pattern specifications are satisfied at the expense of the dissipated active power. In Table 5.3 the first row refers to the weights computed with the starting current, while the symbol  $\times$  means that the default weight has been chosen, as the functional is equal to zero. By looking at the optimized currents in Figure 5.2, the one obtained by

	$f_{act}$	$f_{imp}^L$	$f_{imp}^U$	$f_{scal}$	$f_{ref}$	$f_{co}^L$	$f_{co}^U$	$f_{cx}$	$f_{tot}$
St	$6 \cdot 10^{-4}$	0	$4 \cdot 10^{-4}$	$10^{-4}$	0	0	0.13	$2 \cdot 10^9$	0
1	$2 \cdot 10^{-9}$	$10^{-8}$	$3 \cdot 10^{-10}$	$10^{-7}$	$9 \cdot 10^6$	0	16.5	0	$3 \cdot 10^3$
2	$10^{-8}$	$2 \cdot 10^{-8}$	$2 \cdot 10^{-13}$	$9 \cdot 10^{-6}$	$3 \cdot 10^6$	0	8.15	0	$10^2$
3	$6 \cdot 10^{-6}$	$4 \cdot 10^{-6}$	$10^{-17}$	$10^{-6}$	0	0	6.52	0	0
4	$10^{-7}$	$3 \cdot 10^{-9}$	$10^{-15}$	$10^{-7}$	0	0	0.03	0	0

**Table 5.2:**  $10\lambda_0$  - pencil beam - circular polarization: functionals values during the optimization performed with 4 weight updates.

	$w_{act}$	$w_{imp}^L$	$w_{imp}^U$	$w_{scal}$	$w_{ref}$	$w_{co}^L$	$w_{co}^U$	$w_{cx}$	$w_{tot}$
1	0.85	$\times$	0.14	0.49	$\times$	$\times$	$3 \cdot 10^{-7}$	$2 \cdot 10^{-15}$	$\times$
2	0.03	0.02	0.9	0.01	$6 \cdot 10^{-14}$	$\times$	$2.3 \cdot 10^{-9}$	$2 \cdot 10^{-15}$	$2 \cdot 10^{-11}$
3	0.94	0.3	0.04	0.17	$10^{-11}$	$\times$	$5.7 \cdot 10^{-10}$	$2 \cdot 10^{-15}$	$3 \cdot 10^{-12}$
4	0.48	0.01	0.3	0.8	$2 \cdot 10^{-11}$	$\times$	$8 \cdot 10^{-10}$	$2 \cdot 10^{-15}$	$3 \cdot 10^{-12}$

**Table 5.3:**  $10\lambda_0$  - pencil beam - circular polarization: assigned weights during the optimization performed with 4 weight updates.

the method described in this work (Figure 5.2b) is cleaner and smoother than the one obtained by the NLCG (Figure 5.2a). The same can be told about the surface impedance distribution (Figure 5.3): the one in Figure 5.3b exhibits a clear spiral

shape, as also obtained by [20] on the basis of theoretical considerations.

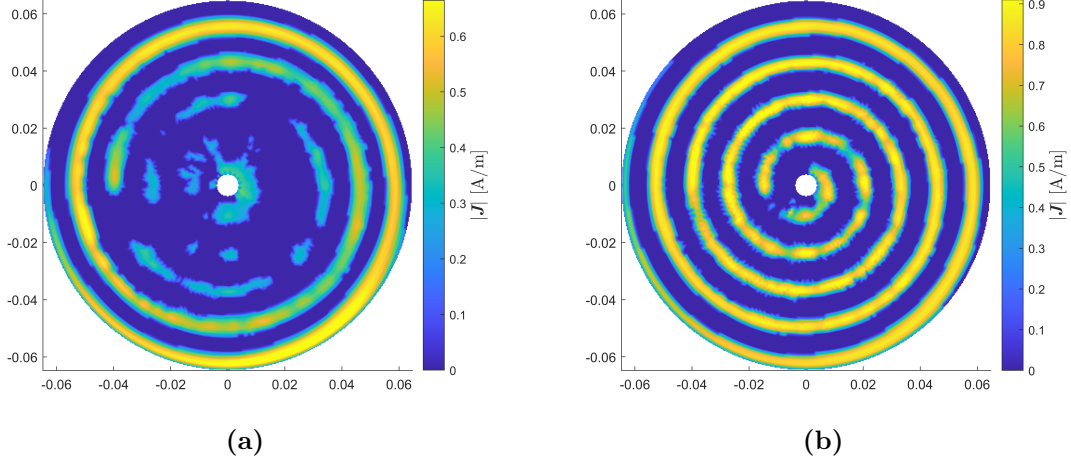


**Figure 5.2:**  $10\lambda_0$  - pencil beam - circular polarization: optimized surface current using (a) NLCG and (b) NLCG-HAW.

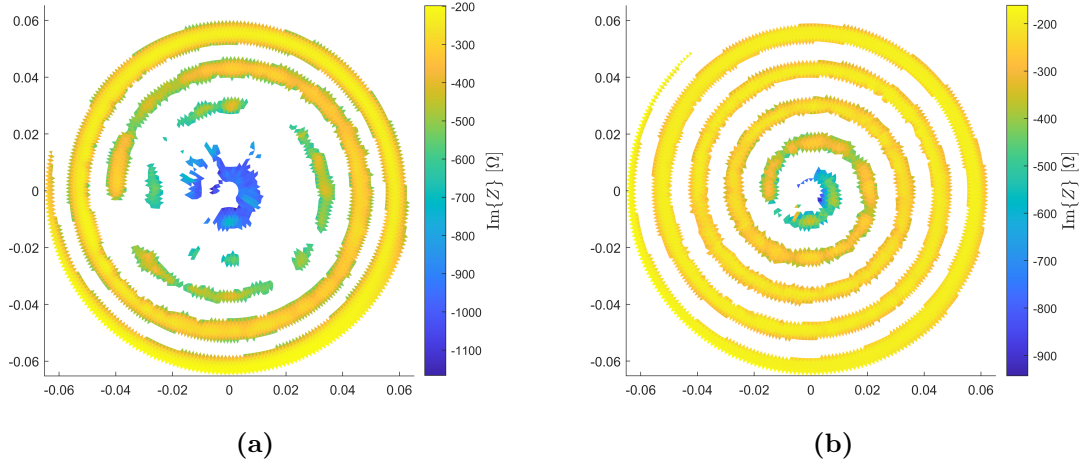


**Figure 5.3:**  $10\lambda_0$  - pencil beam - circular polarization: regularized surface impedance distribution using (a) NLCG and (b) NLCG-HAW.

About the radiated field, the directivity is proposed in Figure 5.4-5.5: blue dashed lines represent the main lobe level and the side lobes mask, solid magenta line represents the cross-polarization mask (whose requirement is referred in the region of the main lobe), vertical arrows are the relative levels. As can be seen in both planes, the requirements regarding side lobes are not fully met using

only NLCG (Figure 5.4a-5.5a), whereas they are when using the version with the re-weight algorithm (Figure 5.4b-5.5b). The obtained cross-pol. level is, instead, almost fully met using both approaches.

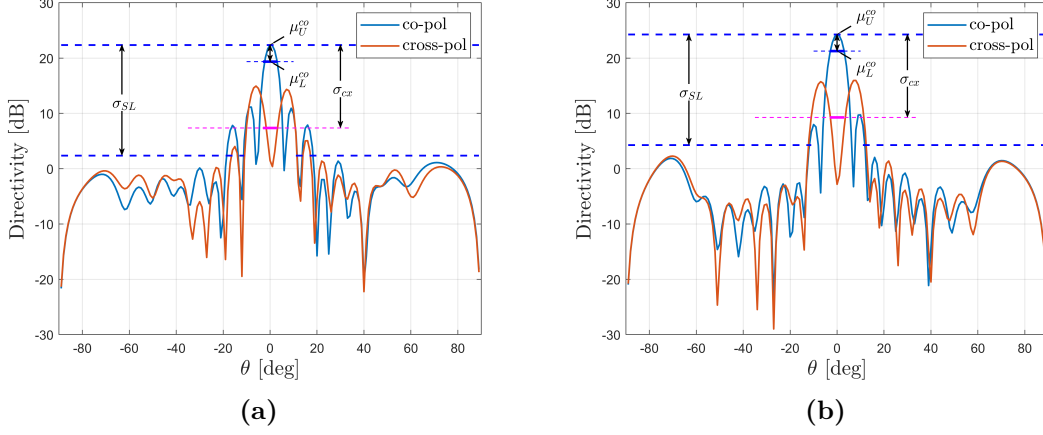


**Figure 5.4:**  $10\lambda_0$  - pencil beam - circular polarization: co- and cross- pol., cut for  $\phi = 0$ . (a) NLCG result, (b) NLCG-HAW result.

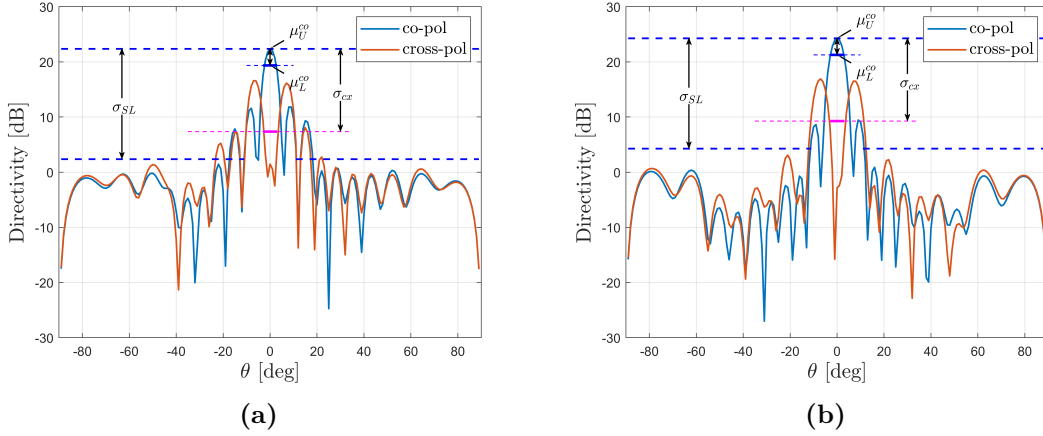


**Figure 5.5:**  $10\lambda_0$  - pencil beam - circular polarization: co- and cross- pol., cut for  $\phi = 90$ . (a) NLCG result, (b) NLCG-HAW result.

The achieved maximum directivity  $D_{max}$  (computed in the broadside direction  $\theta = 0^\circ$ ) and the aperture efficiency  $\eta_{ap}$  are respectively 22.35 dB and 17% for the NLCG-only and 24.26 dB and 27% for the hybrid implementation.

The same antenna has been further optimized with the NLCG only and the same set of weights. After 1000 iterations, the algorithm quits, since a local minimum

is reached. The final results after 1000 iterations are now comparable with those obtained by the hybrid approach performed over 400 iterations:  $D_{max} = 23.85$  dB,  $\eta_{ap} = 24\%$  and the radiated field now complies with the masks (Figure 5.7). As can be seen from Figure 5.6, the optimized current and the regularized impedance now have a clean spiral shape, as theoretical results suggest.

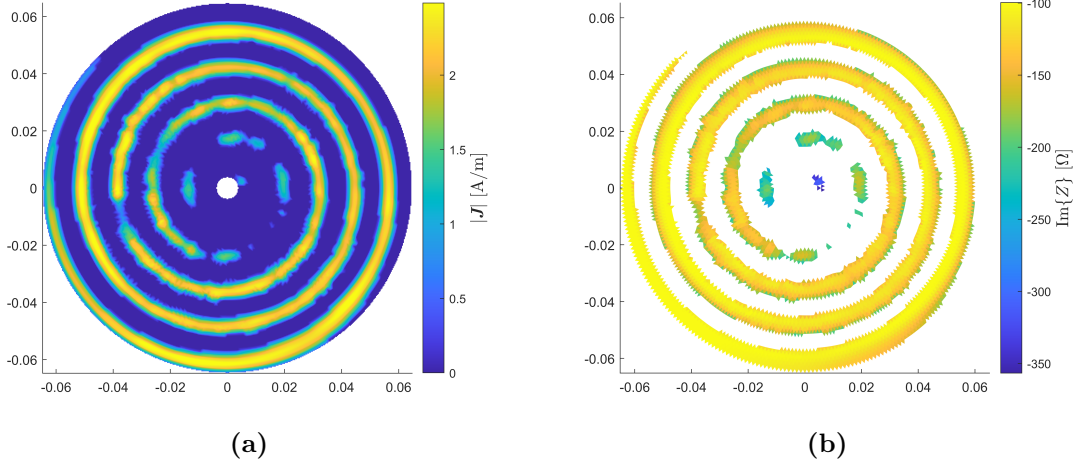


**Figure 5.6:**  $d = 10\lambda_0$  - pencil beam - circular polarized field - NLCG only: (a) optimized surface current and (b) regularized surface impedance distribution.

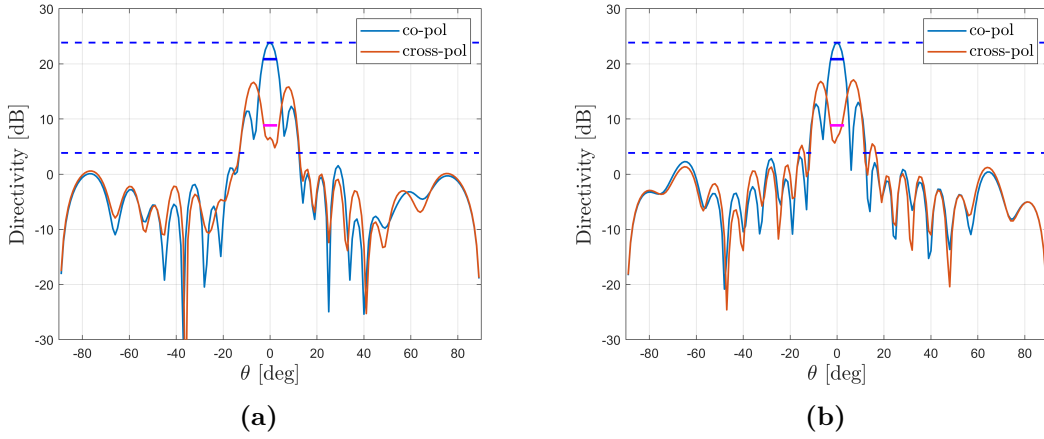


**Figure 5.7:**  $d = 10\lambda_0$  - pencil beam - circular polarized field - NLCG only: co- and cross-pol., (a) cut for  $\phi = 0$  and (b)  $\phi = 90$ .

This first result aims to demonstrate how the design of a metasurface antenna could be penalized by an irrational weights selection. The method shown in this

work, on the other hand, is capable of fully recovering from an inaccurate initial set of weights and can produce a respectable result after a limited number of iterations.

### 5.2.2 Linear polarization

Using the design parameters of Table 5.1, the same  $10\lambda$  circular MTS antenna has been designed using only the NLCG-HAW algorithm, requiring a linear polarized field. The number of total iterations is still 400. This time  $N_w = 8$ , as it has been experimentally observed that a larger number of re-weighting leads to better results for linear polarized antennas. Figure 5.8 illustrates how the impedance profile

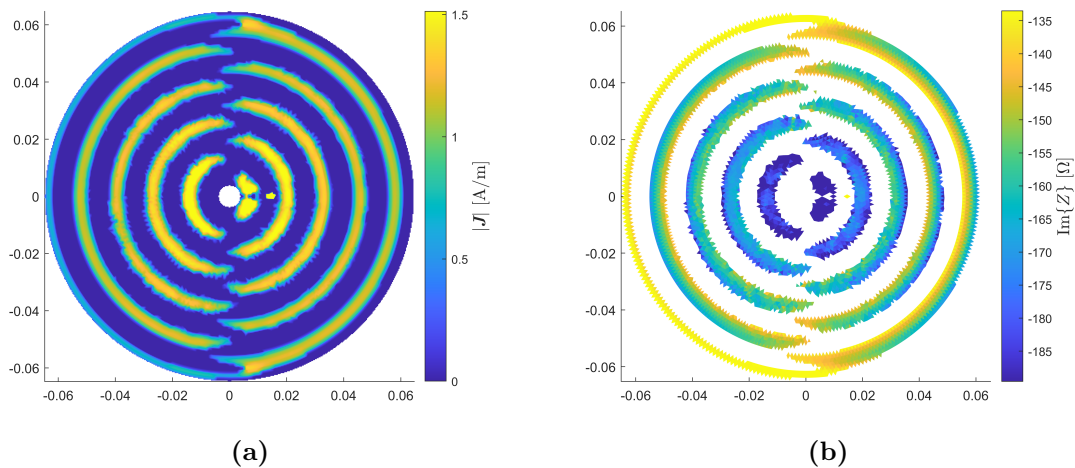


**Figure 5.8:**  $d = 10\lambda_0$  - pencil beam - linear polarized field: (a) optimized surface current and (b) regularized surface impedance distribution.

and consequently the optimum current differ from the spiral-shaped of circular polarized antennas. Theoretical results back up this conclusion [21]. As can be seen, the range of the reactance is between  $-185\Omega$  and  $-135\Omega$  with decreasing values close to the feeding. Regarding the radiated field, the cut for  $\phi = 0^\circ$  exhibits two symmetric "shoulders" next to the main beam. This characteristic is shared by all antennas designed in this work and it is partly caused by the choice of the incident field. Despite being linear polarized, the incident surface wave has a radial direction, making the design of circular polarized field simpler and the radiation pattern clearer in both cuts.

The maximum directivity for this  $10\lambda_0$  antenna with linear polarized field (Figure 5.9) is equal to 23.5 dB, with an aperture efficiency of 24%, so not too far from the performance of the same antenna with circular polarized field.

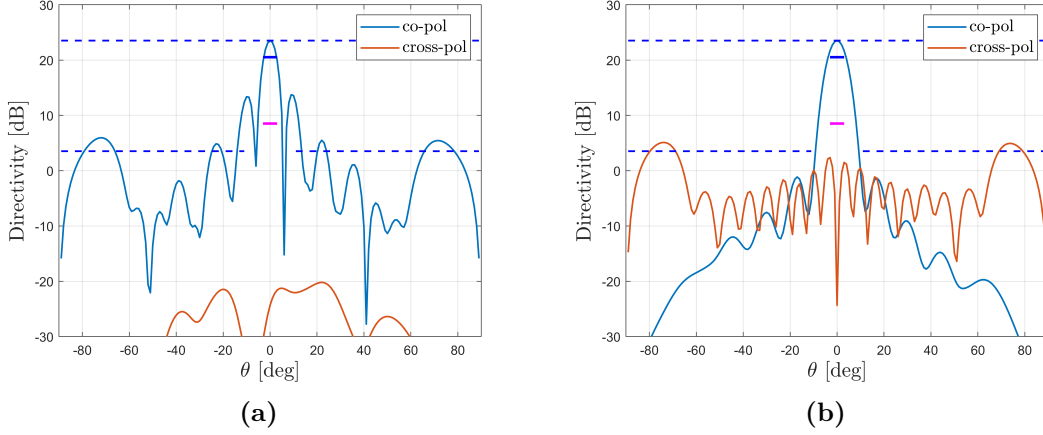


**Figure 5.9:**  $d = 10\lambda_0$ . Pencil beam - linear polarized field: co- and cross-polarization. Cut for (a)  $\phi = 0^\circ$  and (b)  $\phi = 90^\circ$ .

### 5.2.3 Full-wave solution

In order to validate the result of the optimization, the surface impedance distribution obtained for the  $10\lambda_0$ -antenna with circular polarization employing the NLCG-HAW algorithm has been subjected to realization by means of unit cells. The database employed is made by  $l = \lambda_0/8$  square unit cells and the pattern is obtained by mapping the values of the impedance distribution sampled over squared cells with those realized by the unit cells. Actually, the correspondent value of the side of the single unit cell is found varying  $l$  from 20% to 98% and looking for those that best approximate the value of the surface impedance. Databases are in general constructed through direct simulation of the geometry employing a full-wave solvers, but this aspect will not be discussed further, as it does not represent the topic of this work.

Once the impedance has been synthesized with the geometry, the radiated field can be computed with a full-wave periodic solver. In Figure 5.10, one can appreciate the realized surface impedance with the unit cell and the magnitude of the current density over each cell, while Figure 5.11 shows a comparison between the optimized radiated field and the realized one: as can be seen, the two plots do not differ by a significant amount, which is index of the good quality of the solution.

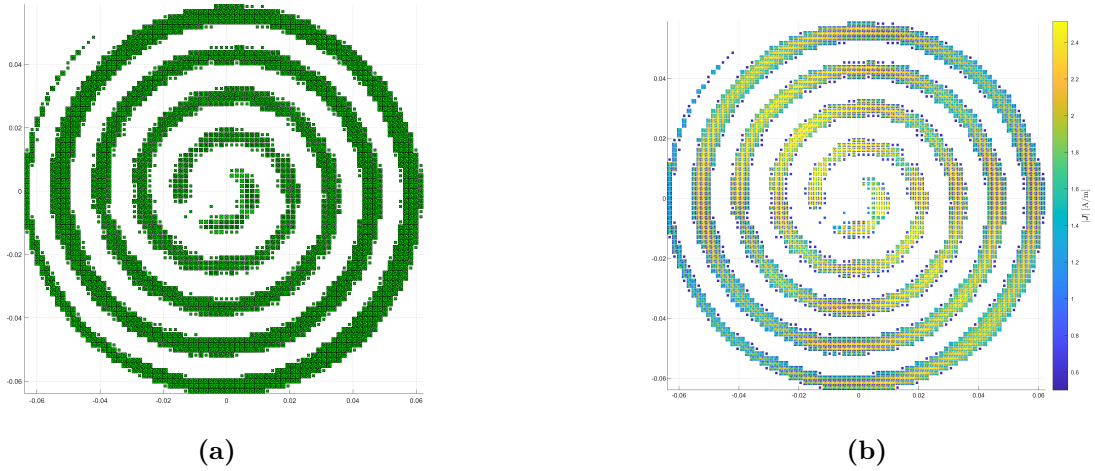


**Figure 5.10:**  $d = 10\lambda_0$  - pencil beam - circular polarized field: (a) unit cells and (b) current distribution over unit cells.

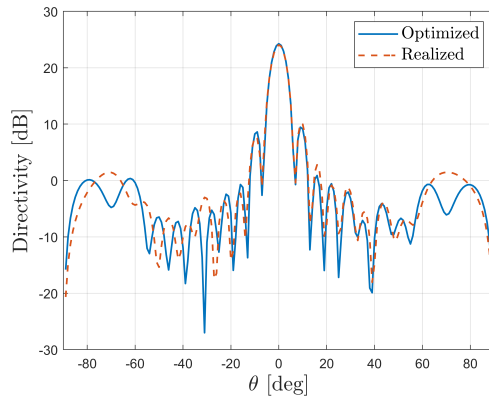


**Figure 5.11:**  $d = 10\lambda_0$  - pencil beam - circular polarized field: co- and cross-polarization. Cut for  $\phi = 0$ , comparison between the optimized radiated pattern and the realized one.

### 5.3 Large sized antenna

In this section, results of the design of a large sized antenna ( $d = 20\lambda_0$ ) are reported. For this geometry, the simulation involves a number of cell  $N_c = 61594$  and  $N = 92096$  RWG basis function. The chosen substrate is the same of the  $d = 10\lambda_0$  antenna, so  $\epsilon_r = 3.34$ ,  $h = 0.508$  mm and  $\mu_r = 1$  and the central frequency is  $f_0 = 23$  GHz. Thanks to the large size of the antenna it is possible to obtain a very directive pattern with very tight beam, therefore the requirement

for this design are  $\Omega_{ML} = 3^\circ$ , so  $\theta_{ML}$  goes from  $-1.5^\circ$  to  $1.5^\circ$  and the side lobes starts from  $\pm 5^\circ$ . Relative levels for side lobes and cross-polarization component are not changed from the previous design. All the simulation constraints are listed in Table 5.4. Results for the same antenna using the NLCG are reported in [7], therefore this section reports only those obtained with the employing of the re-weighting algorithm.

$f_0$	23 GHz
Size	$d = 20\lambda_0$
$\text{Im}\{Z\}[\Omega]$	$-1000 \div -100$
$\theta_{ML}$	$1.5^\circ$
$\theta_{SL}$	$5^\circ$
$\mu_L^{co}$	-3 dB
$\sigma_{SL}$	-20 dB
$\sigma_{cx}$	-15 dB

**Table 5.4:** Design parameters for a large sized antenna with pencil beam radiation pattern.

### 5.3.1 Circular polarization

For the circular polarized field the simulation has been carried out performing four times the re-weighting scheme over a total number of iteration equal to 800. The size of the antenna and thus the number of RWG employed needed more iteration with respect to the  $10\lambda$ -antenna to obtain satisfactory results in terms of surface impedance distribution and radiated field pattern. Results in Figure 5.12 show a clear spiral shape for both optimized current and realized surface impedance, with the latter varying in a range between  $-400\Omega$  and  $-200\Omega$  and values progressively decreasing close to the feeding point. The resulting radiated field pattern is shown in Figure 5.13: as can be seen, all the constraints are satisfied and the directivity in the broadside direction is equal to 30.3 dB, with an aperture efficiency of 29%. Almost identical radiation performance can be found in [7], which means that maybe for this substrate characteristics and radiation specifics a design limit has been reached.

It is worth mentioning that results in Figure 5.12-5.13 has been obtained at first attempt and without any *simulation background*. Later on, further simulations

were performed with various numbers of re-weighting and iterations, but all yielded comparable (or worse) solutions to those shown and therefore they are not reported.

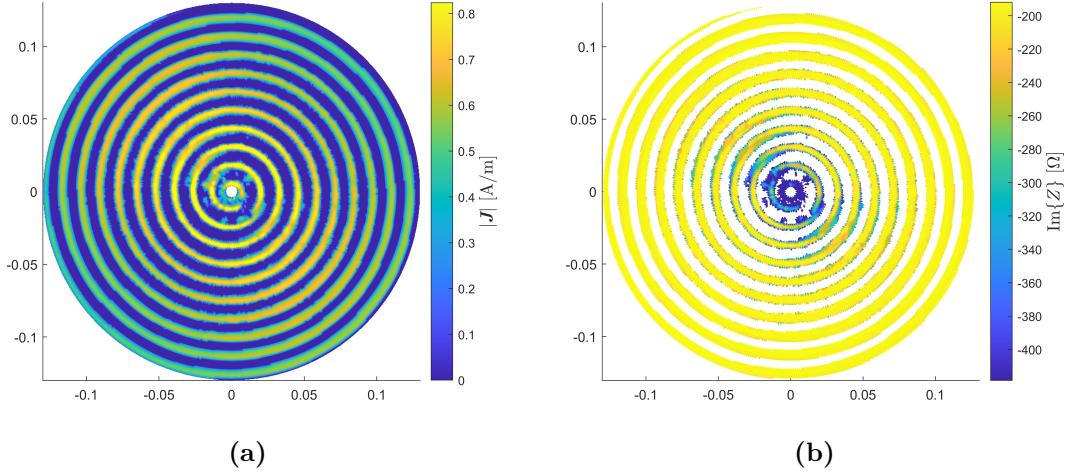


**Figure 5.12:**  $d = 20\lambda_0$ . Pencil beam - circular polarized field: (a) optimized surface current and (b) regularized surface impedance distribution.

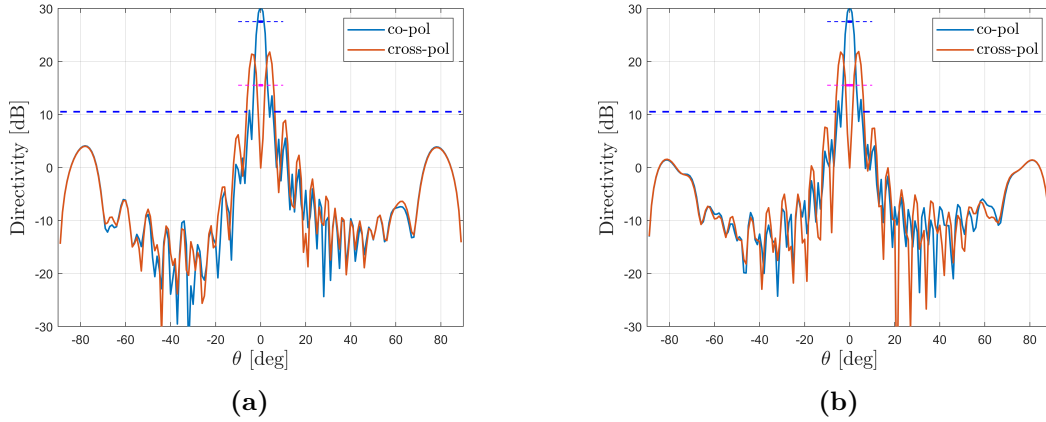


**Figure 5.13:**  $d = 20\lambda_0$ . Pencil beam - circular polarized field. Cuts for (a)  $\phi = 0^\circ$  and (b)  $\phi = 90^\circ$ .

### 5.3.2 Linear polarization

For the linear polarized field specifications, the NLCG-HAW algorithm has been performed for 800 iterations, with a weight update each 100 iterations. As can be

seen from Figure 5.14, the realized surface impedance is clearly within the desired ranges and exhibits a smooth behaviour, as well as the optimized current. The radiated pattern in Figure 5.15 complies with the specifications in both plane cuts and the directivity in the broadside direction is equal to 29.8 dB, which is 1 dB more than the value obtained in [7]. Also in this case, it is worth mentioning that this result has been obtained at first attempt and with a naive set of starting weights.

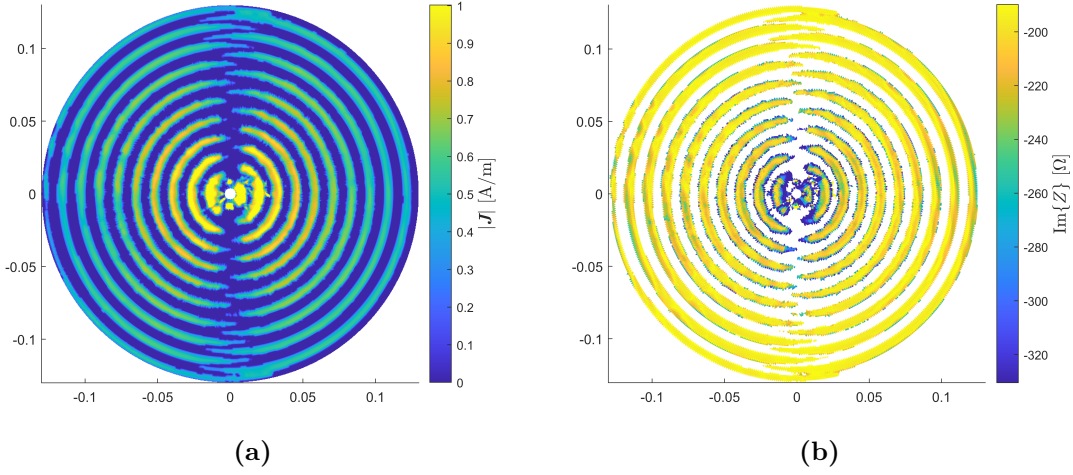


**Figure 5.14:**  $d = 20\lambda_0$ . Pencil beam - linear polarized field: (a) optimized surface current and (b) impedance after regularization.

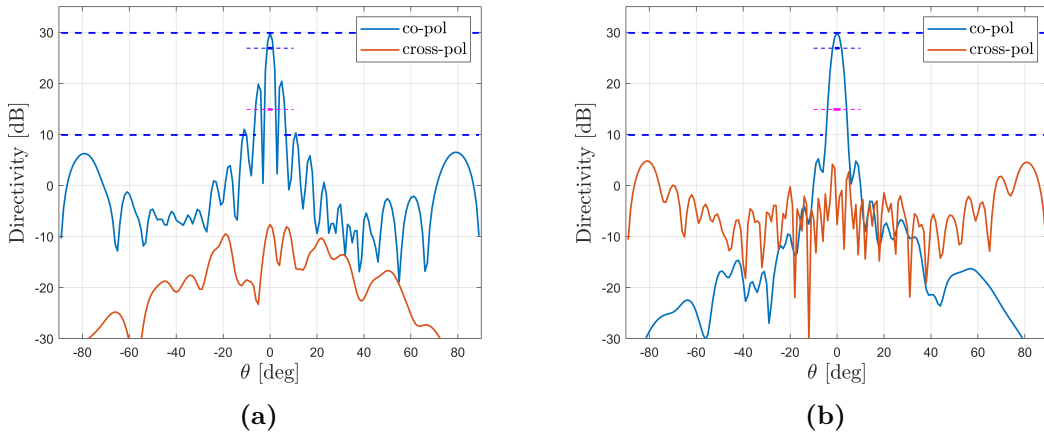


**Figure 5.15:**  $d = 20\lambda_0$ . Pencil beam - linear polarized field: co- and cross-polarization. Cuts for (a)  $\phi = 0^\circ$  and (b)  $\phi = 90^\circ$ .

### 5.3.3 Full-wave solution

The  $20\lambda_0$ -antenna with linear polarized field optimized in the previous section has been subjected to realization with the same database employed for the  $10\lambda_0$ -antenna circularly polarized. As can be seen from Figure 5.16, the unit cell pattern and the current density magnitude over the cells complies with the distribution obtained in Figure 5.14 and the realized radiated pattern (Figure 5.17) overlaps the optimized one, at least in the neighborhood of the main lobe.

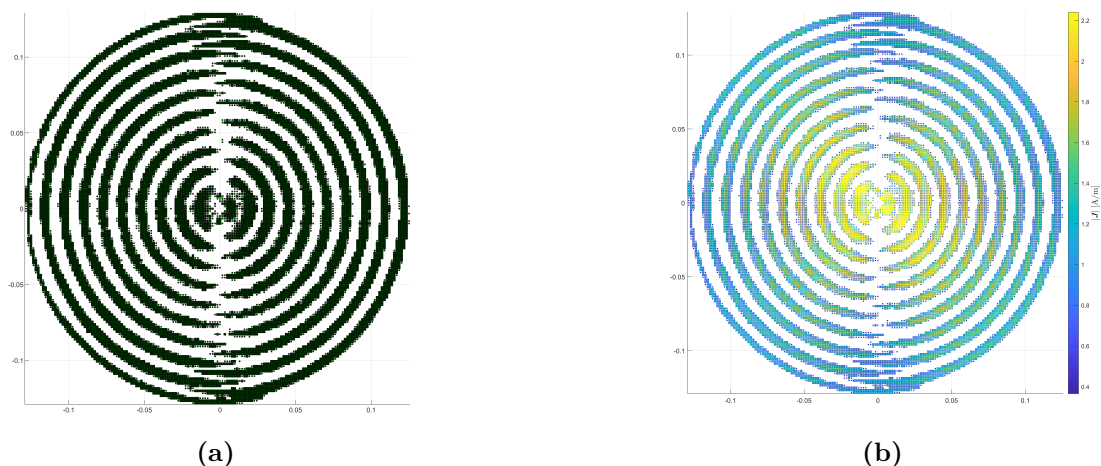


**Figure 5.16:**  $d = 20\lambda_0$  - pencil beam - circular polarization: (a) unit cells and (b) current distribution over unit cells.

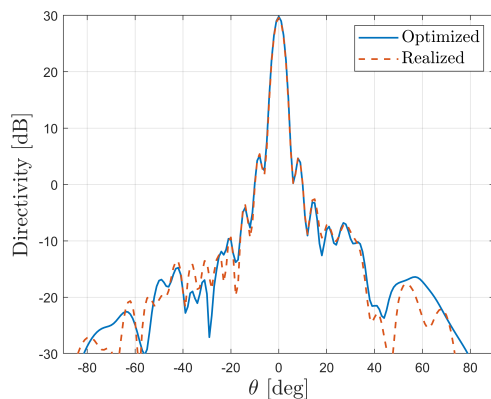


**Figure 5.17:**  $d = 20\lambda_0$  - pencil beam - linear polarization: co- and cross- polarization. Cut for  $\phi = 0$ , comparison between the optimized radiated pattern and the realized one.

## 5.4 Small sized antenna

This section shows the design of a small sized antenna with  $d = 6\lambda_0$ . For this geometry the number of cells is  $N_c = 2047$  and  $N = 4812$  RWG basis function are involved. The chosen substrate is made by a dielectric thickness  $h = 0.76$  mm,  $\epsilon_r = 3$  and the central frequency is 32 GHz. These specifications allow a range of reactance between  $-600\Omega$  and  $-100\Omega$ . The desired pattern shape is still pencil beam but, for this structure, a larger  $\Omega_{ML}$  has been chosen and the same has been done for the side lobe region. The chosen relative levels does not changes from previous design. All the simulation parameters are listed in Table 5.5. The simulations have been carried out both with circular and linear polarization.

$f_0$	32 GHz
Size	$d = 6\lambda_0$
$\text{Im}\{Z\}[\Omega]$	$-600 \div -100$
$\theta_{ML}$	$5^\circ$
$\theta_{SL}$	$20^\circ$
$\mu_L^{co}$	-3 dB
$\sigma_{SL}$	-20 dB
$\sigma_{cx}$	-15 dB

**Table 5.5:** Design parameters for a small sized antenna with pencil beam radiation pattern.

### 5.4.1 Circular polarization

For this  $6\lambda_0$ -diameter antenna the NLCG-HAW algorithm has been performed over 400 iterations with 4 weight updates. As can be seen from Figure 5.18, the current exhibits a clean spiral shape. The surface impedance distribution has a spiral shape too with smooth values, but the reactance upper bound is exceeded by a small amount. From Figure 5.19 it can be seen that the radiated field complies with almost all the required specifications in both plans. The directivity in the broadside direction is equal to 20.2 dB and the aperture efficiency is equal to 32%. The obtained directivity value is rather low both because the required main lobe is wider and because, given the dimensions of the MTS, it is difficult to realize high directive antennas.

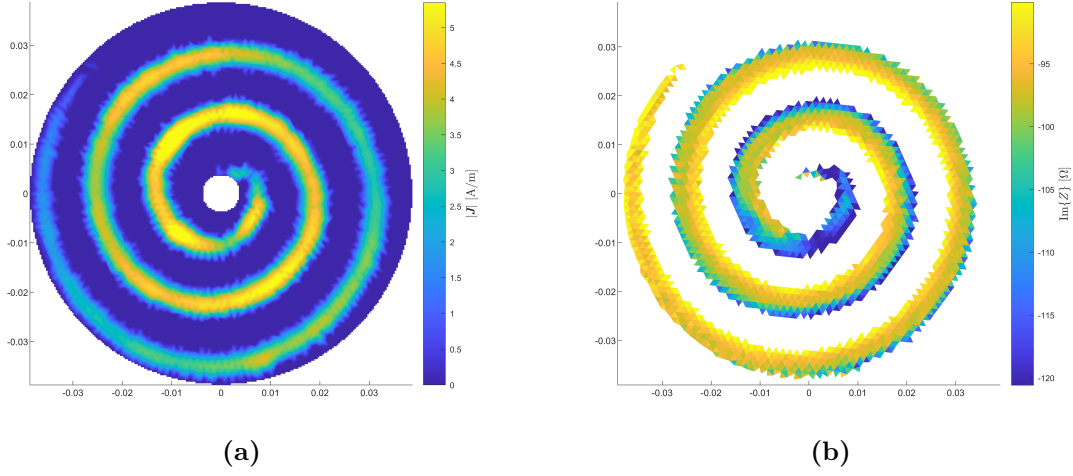


**Figure 5.18:**  $d = 6\lambda_0$ . Pencil beam - circular polarized field: (a) optimized surface current and (b) regularized surface impedance distribution.

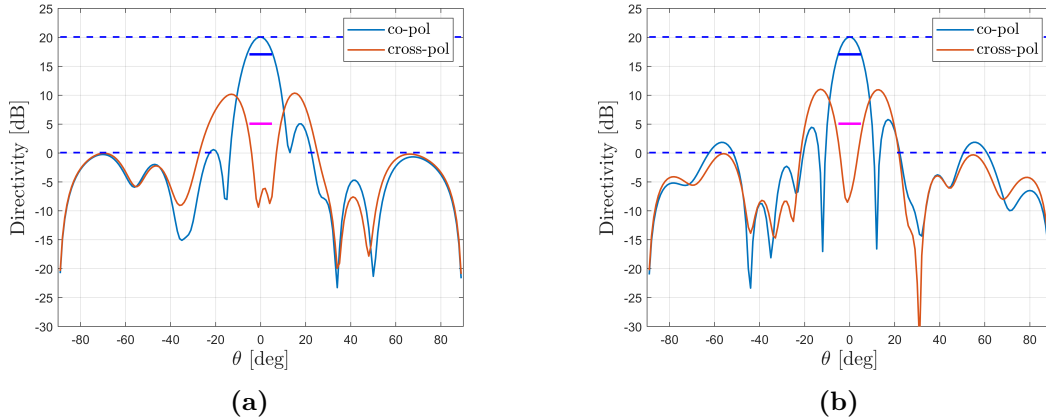


**Figure 5.19:**  $d = 6\lambda_0$ . Pencil beam - circular polarized field: co- and cross-polarization. Cuts for (a)  $\phi = 0^\circ$  and (b)  $\phi = 90^\circ$ .

## 5.4.2 Linear polarization

For the  $6\lambda_0$ -antenna with linear field requirement, the simulation has been carried out still over 400 iterations, but with 8 weight updates (one each 50 iterations), since it shows slightly better results with respect to the previous choice. The current distribution and the surface impedance (Figure 5.20) shows a shape similar to the one obtained with other antenna size. The radiated field (Figure 5.21) shows a maximum directivity of 21.2 dB, while the aperture efficiency is 31%. However, the field pattern in the  $\phi = 0$  plane cut does not comply with the side lobes

specification. The small size of this antenna, together with the chosen substrate, makes difficult the realization of good-directive radiators with low side lobe levels.

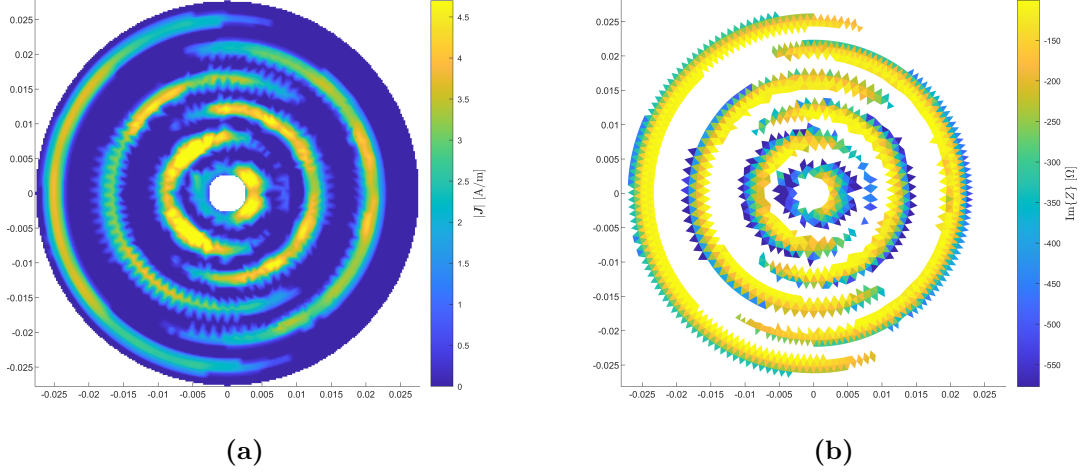


**Figure 5.20:**  $d = 6\lambda_0$ . Pencil beam - linear polarized field: (a) optimized surface current and (b) regularized surface impedance distribution.

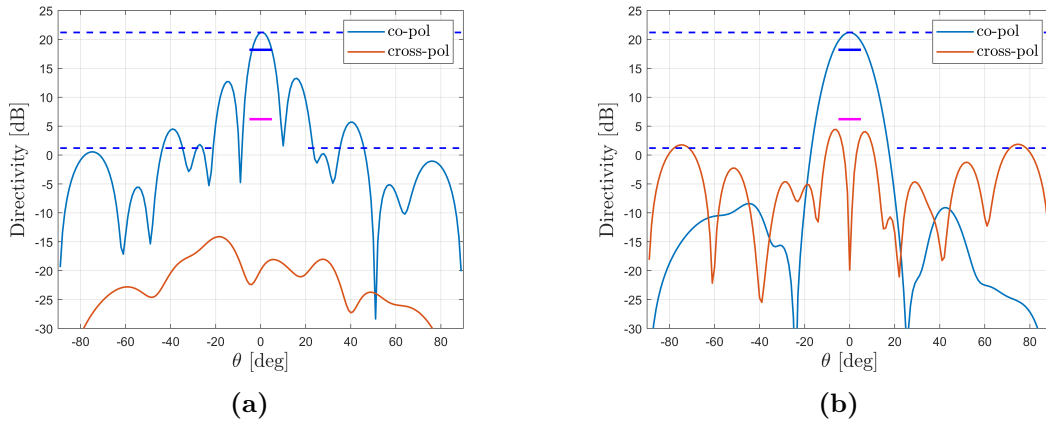


**Figure 5.21:**  $d = 6\lambda_0$ . Pencil beam - linear polarized field: co- and cross-polarization. Cuts for (a)  $\phi = 0^\circ$  and (b)  $\phi = 90^\circ$ .

### 5.4.3 Full-wave solution

The  $6\lambda_0$ -antenna with circular polarized field designed in the previous section has been realized with the squared unit cell database and the full-wave solution is

then computed. As can be seen from Figure 5.22, the unit cell pattern and the magnitude of the current density over the cells basically complies with results in Figure 5.18. However, as can be seen from Figure 5.23, the realized pattern does not completely overlap the optimized one: this is probably due to the fact that the attained surface impedance distributions (Figure 5.18b) exceeds the upper bound value. It cannot be excluded that employing a different unit cell database it would be possible to synthesize that impedance and reach a more consistent result in terms of radiated field pattern.

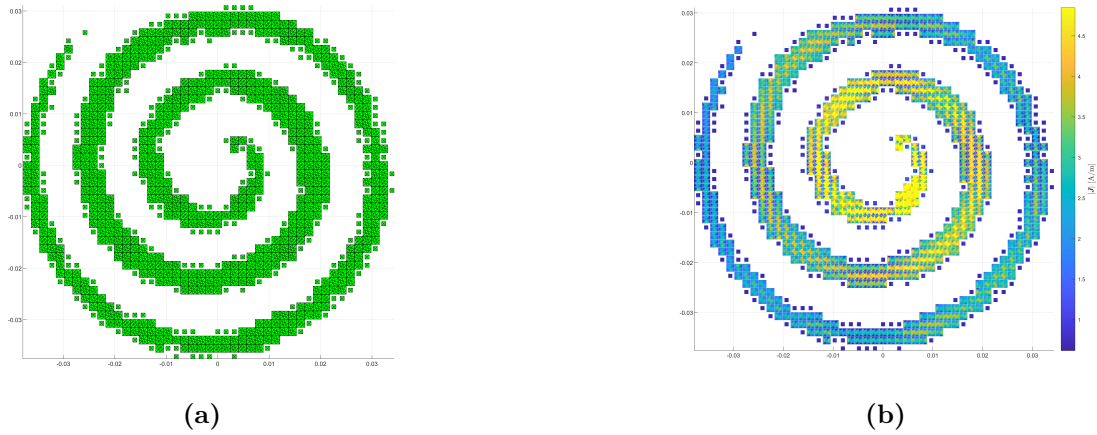


**Figure 5.22:**  $d = 6\lambda_0$  - pencil beam - circular polarized field: (a) unit cells and (b) current distribution over unit cells.

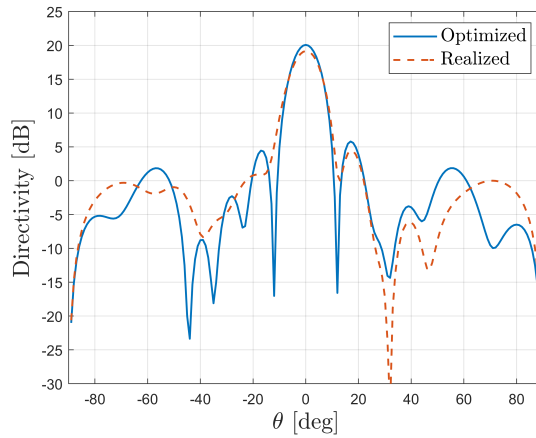


**Figure 5.23:**  $d = 6\lambda_0$  - pencil beam - circular polarized field: co- and cross-polarization. Cuts for  $\phi = 0$ , comparison between the optimized radiated pattern and the realized one.

## 5.5 Medium sized, squinted beam

This result shows the design of a medium sized antenna with  $d = 12\lambda_0$  with circular polarized radiated field and squinted beam radiated pattern. This geometry involves a number of cells  $N_c = 27984$  and  $N = 41776$  RWG basis function. The employed substrate is made by a dielectric thickness  $h$  equal to 1.27 mm with a dielectric constant  $\epsilon_r$  equal to 3. The central frequency  $f_0$  is 23 GHz. The allowed reactance range goes between  $-1000\Omega$  and  $-100\Omega$ . The main lobe is located in the  $\phi = 0^\circ$  plane cut, i.e.  $\phi_0 = 0^\circ$  and it is centered at  $\theta_0 = 30^\circ$ . It extends from  $26.7^\circ$  to  $33.3^\circ$ , i.e. the main lobe region  $\Omega_{ML}$  is equal to  $6.6^\circ$ . The side lobes region starts from  $44.42^\circ$  up to  $90^\circ$  and from  $17.45^\circ$  up to  $-90^\circ$ . The reference level is the directivity obtained in the main lobe, i.e.  $F_{ref} = F(\theta = 30^\circ)$ , while the lower bound is  $\mu_L^{co} = -3$  dB. Side lobes,  $\sigma_{SL}$ , and cross-polarization,  $\sigma_{cx}$ , are respectively equal to -20 dB and -15 dB. All the requirements are listed in Table 5.6. The

$f_0$	23 GHz
Size	$d = 12\lambda_0$
$\text{Im}\{Z\}[\Omega]$	$-1000 \div -100$
$\theta_0$	$30^\circ$
$\phi_0$	$0^\circ$
$\Omega_{ML}$	$6.6^\circ$
$\theta_{SL}^U$	$44.42^\circ$
$\theta_{SL}^L$	$17.45^\circ$
$\mu_L^{co}$	-3 dB
$\sigma_{SL}$	-20 dB
$\sigma_{cx}$	-15 dB

**Table 5.6:** Design parameters for a medium sized antenna with squinted beam radiation pattern.

optimization has been carried out employing the NLCG-HAW algorithm over 1000 iterations with 4 weight update (one each 250 iterations). The optimized surface current and the surface impedance in Figure 5.24 shows the typical squinted beam with circular polarization pattern behaviour, as also reported in [22] based on theoretical considerations. From Figure 5.25, one can appreciate that the main

lobe is effectively centered at  $\theta = 30^\circ$  and the radiated pattern specifications are basically satisfied.

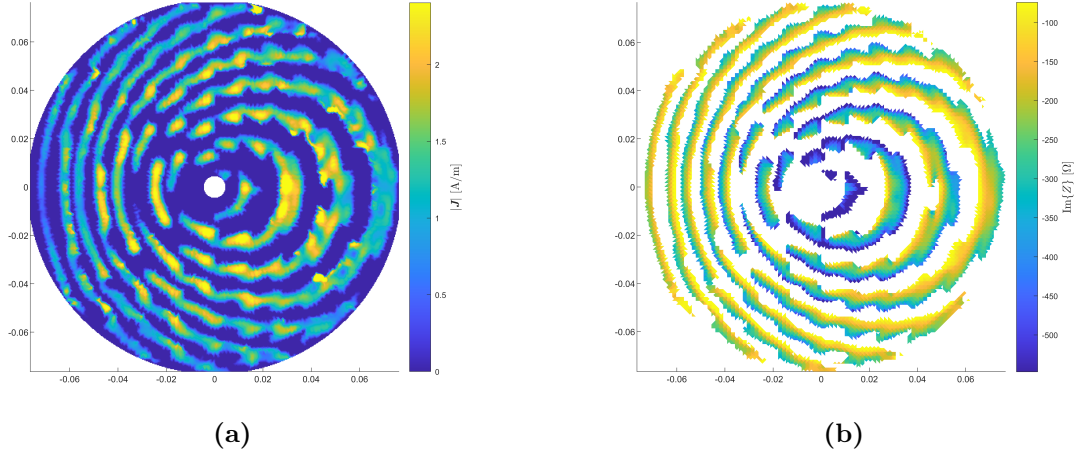


**Figure 5.24:**  $d = 12\lambda_0$ . Squinted beam - circular polarized field: (a) optimized surface current and (b) regularized surface impedance distribution.

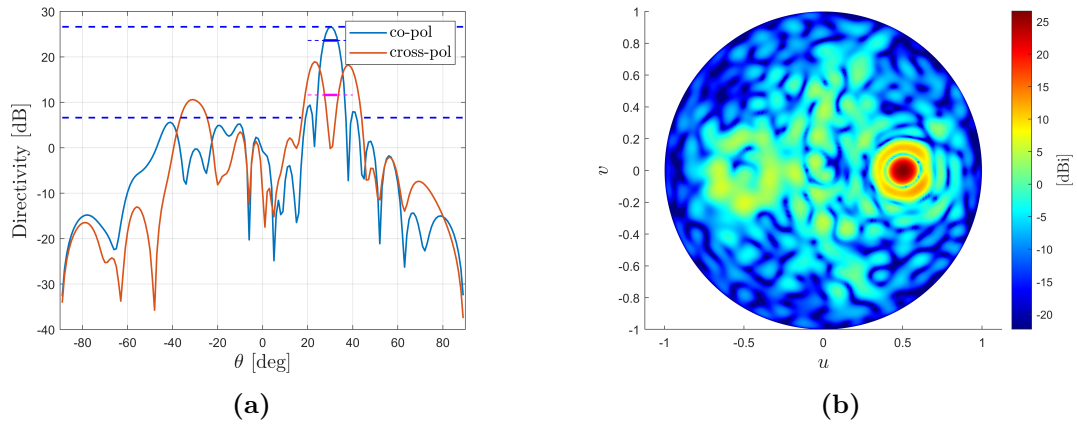


**Figure 5.25:**  $d = 12\lambda_0$ . Squinted beam - circular polarized field: (a) directivity in the plane cut  $\phi = 0$  and (b) top view of the pattern in the  $u - v$  plane.

# Chapter 6

## Conclusions

In this work, optimization strategies for the design of MTS antennas have been described. The aim of the proposed techniques was to improve the convergence performance of the current-based approach without modifying in a significant way the original algorithm and especially without increasing its numerical complexity.

Two different approaches have been considered. The introduction of slack variables makes the objective function purely polynomial. However, the large number of extra optimization variables, as it has been shown, slows down the convergence of the optimization. Therefore, continuing to work with an objective function that employs ramp functions for the inequality constraints seems to be the wisest choice, at least until further developments.

The hyperplane adaptive weighting method has been introduced to free the user from an accurate choice of the starting weights. It has been observed that, without any preliminary analysis, and therefore without any knowledge of the orders of magnitude of optimal weights, it is possible to achieve results comparable with those attained by the standard algorithm after thorough manual research on the optimal set of weights. The proposed re-weighting scheme thus makes the current-based optimization algorithm more robust and reliable, even managing to improve results presented in literature that were already considered at the limit of capability. Of course, the proposed algorithm has room for improvements. Managing the potential near-singular matrices of anchor points could be the key to make the algorithm even more reliable. Similarly, developing a general criterion to balance the number of weight updates and the total number of iterations could further enhance its performance.

The intrinsic non-convexity of the objective function remains an insurmountable problem to date. Regarding possible future developments, the path of convexification is worth pursuing, enabling us to fully leverage the well-established properties of existing minimization algorithms. At last, results in terms of current density and surface impedance distribution could be potentially further improved through

techniques like smoothing or filtering.

# Appendix A

## Antenna generalities

### A.1 Field polarization

In most applications, electromagnetic field sources have a sinusoidal waveform. Therefore, in the presence of a linear and stationary propagation medium, the resulting field will be sinusoidal in time. This time-harmonic electromagnetic field (i.e. sinusoidal) is made by a pair of vectors assigned for any time and point in space:

$$\begin{aligned}\mathcal{E}(\mathbf{r}, t) &= \text{Re}\{\mathbf{E}(\mathbf{r})e^{j\omega t}\}, \\ \mathcal{H}(\mathbf{r}, t) &= \text{Re}\{\mathbf{H}(\mathbf{r})e^{j\omega t}\},\end{aligned}$$

where  $\mathbf{r}$  is the position vector,  $\omega$  incorporates the frequency of the electromagnetic field and  $\mathbf{E}$  and  $\mathbf{H}$  are complex vectors.

Focusing only on the electric field, one can write the complex vector  $\mathbf{E}(\mathbf{r})$  as:

$$\mathbf{E} = E_x\hat{\mathbf{x}} + E_y\hat{\mathbf{y}} + E_z\hat{\mathbf{z}},$$

where the spatial dependency has been suppressed for the sake of brevity. The components of  $\mathbf{E}$  are complex numbers called phasors.

Another common expression for  $\mathbf{E}$  is in terms of in-phase and in-quadrature components,

$$\mathbf{E} = \mathcal{E}(t = 0) - j\mathcal{E}(t = T/4) = \mathbf{E}' + j\mathbf{E}'',$$

with  $\mathbf{E}'$  and  $\mathbf{E}''$  time invariant real vectors that define the plane where the electric field  $\mathcal{E}(\mathbf{r}, t)$  describes a locus. It can be demonstrated that, in general, this locus is an ellipse, and so will be the *polarization of the field*.

Therefore, the polarization can be defined as the oscillation direction of the electric field while the electromagnetic wave is propagating. Since the electromagnetic wave is made by a couple of vectors ( $\mathcal{E}$  and  $\mathcal{H}$ ), always orthogonal to each other, the magnetic field will be polarized in the orthogonal direction to the one of the

electric field and to the propagation direction.

When the polarization is *linear*, the electric field oscillates in a single direction while propagating, while when the polarization is *circular* or *elliptical* the field rotates and it depends on the spatial orientation of the in-phase and in-quadrature components and on their amplitudes. Here, the main conditions are summarized:

$ \mathbf{E}'  = 0,  \mathbf{E}''  \neq 0$ or $ \mathbf{E}'  \neq 0,  \mathbf{E}''  = 0$ or $\mathbf{E}' \times \mathbf{E}'' = 0$	Linear polarization
$ \mathbf{E}'  =  \mathbf{E}'' $ and $\mathbf{E}' \cdot \mathbf{E}'' = 0$	Circular polarization

A common way to describe the polarization of the field is by means of the polarization unit vector, defined as

$$\hat{\mathbf{p}} = \frac{\mathbf{E}}{|\mathbf{E}|} = \frac{\mathbf{E}' + j\mathbf{E}''}{\sqrt{|\mathbf{E}|^2}} = \hat{\mathbf{p}}' + j\hat{\mathbf{p}}'' \quad (\text{A.1})$$

Most of elementary antennas, for instance, those composed of a metallic wire (dipoles), radiate a linearly polarized field, while circular polarized field can be obtained combining two of them (e.g. turnstile antenna). Designing a metasurface antenna with the method described in chapter 3 allows also to obtain the desired polarization.

It is worth mentioning that generally the overall polarization of the field is elliptical, but in practice all antennas have a nominal one, which is the one in the direction of maximum radiation. The nominal polarization, also known as co-polarization, is affected by a spurious radiation or cross-polarization: to quantify this unwanted effect one can compute separately the co- and cross-polarization components,

$$\begin{aligned} E^{co} &= \mathbf{E} \cdot \hat{\mathbf{p}}^* \\ E^{cx} &= \mathbf{E} \cdot \hat{\mathbf{q}}^*. \end{aligned} \quad (\text{A.2})$$

In (A.2),  $\hat{\mathbf{p}}$  and  $\hat{\mathbf{q}}$  are respectively the co- and cross-polarization unit vectors; they are orthogonal to each other and their definition can be given in different ways.

## A.2 Directivity, gain and efficiency

This section provides the description of the most common parameters for evaluating the quality of an antenna design.

The Poynting vector  $\mathbf{S} = \frac{1}{2}Re\{\mathbf{E} \times \mathbf{H}^*\}$  describes the power density associated with the electromagnetic field and can be written in far field condition as

$$\mathbf{S}(r, \theta, \phi) = \frac{1}{2\zeta_0}Re\{\mathbf{E} \times \hat{\mathbf{r}} \times \mathbf{E}^*\} = \frac{1}{2\zeta_0}\mathbf{E} \cdot \mathbf{E}^* \hat{\mathbf{r}}, \quad (\text{A.3})$$

obtained considering the expression  $\mathbf{H} = \frac{1}{\zeta_0}\hat{\mathbf{r}} \times \mathbf{E}$ , where  $\zeta_0$  is the free space impedance.

The *directivity* represents a normalized distribution function of the power density over angular directions and it is defined as:

$$d(\theta, \phi) = \frac{S(r, \theta, \phi)}{S_{av}(r)}, \quad (\text{A.4})$$

where  $S_{av}(r)$  is the average power density over a sphere of radius  $r$ ,

$$S_{av}(r) = \frac{1}{4\pi r^2} \iint_{sphere} S(r, \theta, \phi) d\Sigma = \frac{P_{rad}}{4\pi r^2}, \quad (\text{A.5})$$

where  $P_{rad}$  is the power radiated by the antenna. Therefore, the expression of the directivity function is:

$$d(\theta, \phi) = \frac{S(r, \theta, \phi)}{P_{rad}/4\pi r^2}. \quad (\text{A.6})$$

Without any other specifications, the term "directivity" refers to the maximum of the function, so

$$D = \max_{\theta, \phi} d(\theta, \phi) \quad (\text{A.7})$$

The same definition holds for the *gain*, but, instead of the radiated from the antenna, the power delivered (or accepted) is considered. The amount of power radiated is a fraction of the accepted power equal to the *ohmic efficiency*:

$$\eta = \frac{P_{rad}}{P_{in}} < 1, \quad (\text{A.8})$$

as a consequence, the gain function can be written as

$$g(\theta, \phi) = \frac{S(r, \theta, \phi)}{P_{in}/4\pi r^2} = \eta d(\theta, \phi). \quad (\text{A.9})$$

Without any other specifications, the gain refers to the maximum of the gain function

$$G = \max_{\theta, \phi} G(\theta, \phi). \quad (\text{A.10})$$

The *effective area* (or *equivalent area*) is an antenna parameter referred to the reception mode and allows to transform an electromagnetic quantity (power density) into an electric one (power). It is defined as the quantity that, multiplied by the incident power density, gives the available output power of the antenna:

$$A_{eff} = \frac{P_{av}}{S_{inc}} \quad (\text{A.11})$$

which is valid supposing that there is no polarization mismatch between the Tx and Rx antenna, i.e.  $|\hat{\mathbf{p}}_{TX} \cdot \hat{\mathbf{p}}_{RX}|^2 = 1$ . The effective area allows to define another important figure of merit for the performance of aperture antennas, thus MTS antennas, which is the *aperture efficiency*  $\eta_{ap}$ :

$$\eta_{ap} = \frac{A_{eff}}{A_{geom}}, \quad (\text{A.12})$$

where  $A_{geom}$  is the geometric area of the aperture.

## Appendix B

# Source field for circular metasurface

The feeding for circular metasurface antennas designed in this work is provided through the electromagnetic field radiated by a vertical dipole placed in the centre of the structure. Since the MTS is basically made by a ground plane (modelled as a PEC), a dielectric substrate and air, the source field will be the surface wave generated by the dipole in the dielectric slab.

It can be demonstrated that the most excited mode by a feed with vertical dipole is

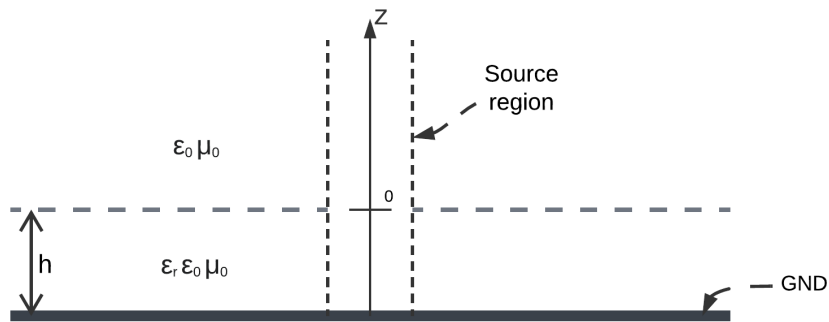


**Figure B.1:** Slab geometry.

the  $TM_z$ , where subscript  $z$  means *transversal to the  $z$  direction*. High-order modes are also excited, but their amplitude is negligible for the purpose of MTS design. The geometry of the problem (see Figure B.1) suggests to employ a cylindrical coordinates system, where clearly the source dipole is oriented along the  $\hat{z}$  axis.

Since the sought solution is the  $TM_z$ , the magnetic vector potential can be written as  $\mathbf{A}(\rho, \phi, z) = A(\rho, \phi, z)\hat{\mathbf{z}}$ . It must satisfy the Helmholtz's equation:

$$\nabla^2 A_z + k^2 A_z = 0, \quad (\text{B.1})$$

where  $k = \omega\sqrt{\epsilon\mu}$  is the wave number. Once the magnetic vector potential is obtained solving (B.1), the electric and magnetic field components in cylindrical coordinates can be simply derived by using:

$$E_\rho = \frac{1}{j\omega\mu\epsilon} \frac{\partial^2}{\partial\rho\partial z} A_z \quad H_\rho = \frac{1}{\mu\rho} \frac{\partial}{\partial\phi} A_z, \quad (\text{B.2})$$

$$E_\phi = \frac{1}{j\omega\mu\epsilon} \frac{1}{\rho} \frac{\partial^2}{\partial\phi\partial z} A_z \quad H_\phi = -\frac{1}{\mu} \frac{\partial}{\partial\rho} A_z, \quad (\text{B.3})$$

$$E_z = \frac{1}{j\omega\mu\epsilon} \left( \frac{\partial^2}{\partial z^2} + k^2 \right) A_z \quad H_z = 0. \quad (\text{B.4})$$

Thanks to the symmetry of the geometric problem with respect to  $\phi$ , which implies  $\partial/\partial\phi = 0$ ,  $A_z(\rho, \phi, z) = A_z(\rho, z)$ ,  $E_\phi = 0$  and  $H_\rho = 0$ .

One is interested in the solution travelling towards positive  $\rho$  direction, so then the radial dependency of the magnetic field vector is expressed with the Hankel's function of order zero. The general solution of (B.1) is:

$$A_z(\rho, z) = H_0^{(2)}(k_\rho\rho) \begin{cases} Ae^{-jk_z z} + Be^{jk_z z} & z > 0 \\ C\sin(k_z z) + D\cos(k_z z) & -h \leq z \leq 0, \end{cases} \quad (\text{B.5})$$

which represents a plane wave travelling along the  $\hat{\mathbf{z}}$  axis in the free space ( $z > 0$ ), while inside the dielectric ( $-h \leq z \leq 0$ ), the electromagnetic field is confined. The (B.5) must be completed by the dispersion relation:

$$k^2 = k_\rho^2 + k_z^2 \quad (\text{B.6})$$

It is trivial to understand from the very beginning that  $B = 0$ , since one is interested only in a wave propagating towards the positive  $z$ -direction. Then, in order to find the constant terms  $A$ ,  $C$  and  $D$ , one must enforce the boundary conditions to the electric and magnetic field.

## Ground plane

The presence of the ground plane at  $z = -h$  implies:

$$\mathbf{E}_t = 0 \longrightarrow E_\rho^d = 0, \quad (\text{B.7})$$

where superscript  $d$  means that the considered component is the one in the dielectric. From (B.2), together with (B.5), the obtained expression is <sup>1</sup>:

$$E_\rho^d(\rho, z = -h) = \frac{k_\rho k_z^d}{j\omega\mu\epsilon} H_1^{(2)}(k_\rho\rho)[-C\sin(k_z^d h) - D\cos(k_z^d h)] = 0 \quad (\text{B.8})$$

$$\longrightarrow D = -C\tan(k_z^d h). \quad (\text{B.9})$$

## Air-dielectric interface

At  $z = 0$  of the electric field tangential components must be enforced:

$$\mathbf{E}_t^+ = \mathbf{E}_t^- \longrightarrow E_\rho^a(\rho, z = 0) = E_\rho^d(\rho, z = 0), \quad (\text{B.10})$$

where superscript  $a$  is used to represents the in-air component. This implies:

$$jk_z^a A - \frac{k_z^d}{\epsilon_r} \tan(k_z^d h) C = 0. \quad (\text{B.11})$$

Moreover, also the continuity of the tangential magnetic field is imposed:

$$\mathbf{H}_t^+ = \mathbf{H}_t^- \longrightarrow H_\phi^a(\rho, z = 0) = H_\phi^d(\rho, z = 0), \quad (\text{B.12})$$

$$\longrightarrow A - C = 0. \quad (\text{B.13})$$

It is clear that the constants  $A$  and  $C$  must satisfy simultaneously (B.11) and (B.13). The resulting homogeneous linear system provides non trivial solution if the determinant is null, therefore another condition must be enforced:

$$jk_z^a - \frac{k_z^d}{\epsilon_r} \tan(k_z^d h) = 0 \quad (\text{B.14})$$

Since the field must be evanescent in the free space, the wave number  $k_z^a$  is purely imaginary and it can be written  $\alpha_z = jk_z^a$ , where  $\alpha_z$  is the attenuation constant along the  $z$ -direction. Therefore, by using (B.6):

$$\begin{aligned} k_z^d &= \sqrt{k^2 - k_\rho^2} \\ \alpha_z &= \sqrt{k_\rho^2 - k_0^2}, \end{aligned} \quad (\text{B.15})$$

the (B.14) can be solved in order to find  $k_\rho$ .

The expressions of the electric field in air and dielectric are:

$$E_\rho^a = \frac{\beta_{sw}\alpha_z}{j\omega\mu_0\epsilon_0} A H_1^{(2)}(\beta_{sw}\rho) e^{-\alpha_z z}, \quad (\text{B.16})$$

---

<sup>1</sup>The derivative of  $H_0^{(2)}$  is  $H_1^{(2)}$

$$E_\rho^d = \frac{\beta_{sw} k_z^d}{j\omega\mu_0\epsilon_0\epsilon_r} A H_1^{(2)}(\beta_{sw}\rho) [\sin(k_z^d z) + \tan(k_z^d h) \cos(k_z^d z)], \quad (\text{B.17})$$

where  $\beta_{sw} = k_\rho$ , as the dielectric substrate is considered lossless. Since one is interested in the surface wave exciting the MTS, only the components along  $\hat{\boldsymbol{\rho}}$  are reported.

The value of the constant A can be chosen such that the expression of the field, e.g. the (B.16), simplifies in:

$$E_\rho^a = E_0 H_1^{(2)}(\beta_{sw}\rho) e^{-\alpha_z^a z}, \quad (\text{B.18})$$

where  $E_0$  is chosen such that the power is normalized to 1W. At last, the expression of the incident electric field exciting the MTS is simply obtained by forcing  $z = 0$  in (B.18):

$$\mathbf{E}_{inc} = E_0 H_1^{(2)}(\beta_{sw}\rho) \hat{\boldsymbol{\rho}} \quad (\text{B.19})$$

## Appendix C

# Linear and non-linear conjugate gradient algorithms

The linear conjugate gradient (LCG) method is one of the most employed technique for solving large linear systems [9]. It is proposed as an iterative method for solving equations like:

$$\mathbf{Ax} = \mathbf{b}, \quad (\text{C.1})$$

where  $\mathbf{A} \in \mathbb{R}^{N \times N}$  is symmetric and positive definite and  $\mathbf{x}, \mathbf{b} \in \mathbb{R}^N$  are column vectors. This problem can be equivalently written as a quadratic form to be minimized:

$$\min_{\mathbf{x}} f(\mathbf{x}) = \frac{1}{2} \mathbf{x}^\top \mathbf{Ax} - \mathbf{b}^\top \mathbf{x}. \quad (\text{C.2})$$

The gradient of (C.2) corresponds to the residual of the system defined in (C.1), i.e:

$$\nabla f(\mathbf{x}) = \mathbf{r}(\mathbf{x}) = \mathbf{Ax} - \mathbf{b}. \quad (\text{C.3})$$

The LCG incorporates line search methods in order to obtain the final solution, in fact, given the  $\mathbf{x}_k$  at the  $k$ -th iteration, the next step of the iterative algorithm is computed through:

$$\mathbf{x}_{k+1} = \mathbf{x}_k + \alpha_k \mathbf{p}_k, \quad (\text{C.4})$$

where  $\mathbf{p}_k$  is the search direction, in general chosen as gradient descent, and the scalar  $\alpha_k$  is the step length. The line search procedure can be basically considered as a minimization of the  $f$  function with respect to  $\alpha$ , which defines how far one is moving from the point  $\mathbf{x}_k$  in the direction dictated by  $\mathbf{p}_k$ .

When the objective function are in the form of (C.2), the value of  $\alpha_k$  can be computed analitically. Starting from the expression of  $f(\alpha_k)$ :

$$\begin{aligned} f(\alpha) = f(\mathbf{x} + \alpha_k \mathbf{p}) &= \frac{1}{2}(\mathbf{x} + \alpha_k \mathbf{p})^\top \mathbf{A}(\mathbf{x} + \alpha_k \mathbf{p}) + \mathbf{b}^\top (\mathbf{x} + \alpha_k \mathbf{p}) = \\ &= \frac{1}{2}(\mathbf{x}^\top \mathbf{A} \mathbf{x} + \alpha \mathbf{x}^\top \mathbf{A} \mathbf{p} + \alpha \mathbf{p}^\top \mathbf{A} \mathbf{x} + \alpha^2 \mathbf{p}^\top \mathbf{A} \mathbf{p}) - \mathbf{b}^\top \mathbf{x} - \alpha \mathbf{b}^\top \mathbf{p} = \\ &= \frac{1}{2} \alpha^2 \mathbf{p}^\top \mathbf{A} \mathbf{p} + \frac{1}{2} \alpha (\mathbf{x}^\top \mathbf{A} \mathbf{p} + \mathbf{p}^\top \mathbf{A} \mathbf{x}) - \alpha \mathbf{b}^\top \mathbf{p} - \mathbf{b}^\top \mathbf{x} + \frac{1}{2} \mathbf{x}^\top \mathbf{A} \mathbf{x}, \end{aligned} \quad (\text{C.5})$$

where the subscript  $k$  has been dropped for the sake of simplicity, one can compute the derivative with respect to  $\alpha$  and imposes it equal to zero:

$$\alpha \mathbf{p}^\top \mathbf{A} \mathbf{p} + \frac{1}{2} (\mathbf{x}^\top \mathbf{A} \mathbf{p} + \mathbf{p}^\top \mathbf{A} \mathbf{x}) - \mathbf{b}^\top \mathbf{p} = 0. \quad (\text{C.6})$$

Considering that  $(\mathbf{p}^\top \mathbf{A} \mathbf{x})^\top = \mathbf{x}^\top \mathbf{A} \mathbf{p}$ , as  $\mathbf{A}$  is symmetric, one obtains:

$$\alpha = -\frac{(\mathbf{x}^\top \mathbf{A} - \mathbf{b}^\top) \mathbf{p}}{\mathbf{p}^\top \mathbf{A} \mathbf{p}}, \quad (\text{C.7})$$

which, using the (C.3), is equivalent to:

$$\alpha_k = -\frac{\mathbf{r}_k^\top \mathbf{p}_k}{\mathbf{p}_k^\top \mathbf{A} \mathbf{p}_k}. \quad (\text{C.8})$$

The update direction  $\mathbf{p}_k$ , is obtained through:

$$\mathbf{p}_k = -\mathbf{r}_k + \beta_k \mathbf{p}_{k-1}, \quad (\text{C.9})$$

where the scalar term  $\beta_k$  can be computed by imposing a property called *conjugacy* of the vectors  $\mathbf{p}_k$  with respect to  $\mathbf{A}$  [9, p. 108]:

$$\beta_k = \frac{\mathbf{r}_k^\top \mathbf{r}_k}{\mathbf{r}_{k-1}^\top \mathbf{r}_{k-1}}. \quad (\text{C.10})$$

All the steps described above are summarized in the pseudocode Alg. 3.

In order to generalize the LCG algorithm, making it suitable for minimizing objective functions like those described in chapter 3, the non-linear conjugate gradient (NLCG) version is derived. Basically, few changes are made with respect to the previous procedure:

- $\alpha_k$  is computed such as it minimize a generic non-linear function with respect to the search direction  $\mathbf{p}_k$ .

- $\mathbf{p}_k$  is the gradient descent direction, so it can be computed from the knowledge of the gradient of the objective function at the  $k$ -th iteration.
- The expression of  $\beta_k$  is not the one described in (C.10) anymore and its definition is given in different ways, depending on the versions of the algorithm proposed in literature over the years.

The NLCG algorithm is summarized in the pseudocode Alg. 4. About the expression of the scalar  $\beta_k$ , several version are proposed, named according to their inventor:

- Fletcher-Rheeves:

$$\beta_k^{FR} = \frac{\nabla f^\top(\mathbf{x}_k)\nabla f(\mathbf{x}_k)}{\nabla f^\top(\mathbf{x}_{k-1})\nabla f(\mathbf{x}_{k-1})} \quad (\text{C.11})$$

- Polak-Ribière:

$$\beta_k^{PR} = \frac{\nabla f^\top(\mathbf{x}_k)(\nabla f(\mathbf{x}_k) - \nabla f(\mathbf{x}_{k-1}))}{\|\nabla f(\mathbf{x}_{k-1})\|^2} \quad (\text{C.12})$$

- Hestenes-Stifel

$$\beta_k^{HS} = \frac{\nabla f^\top(\mathbf{x}_k)(\nabla f(\mathbf{x}_k) - \nabla f(\mathbf{x}_{k-1}))}{(\nabla f(\mathbf{x}_k) - \nabla f(\mathbf{x}_{k-1}))^\top \mathbf{p}_{k-1}} \quad (\text{C.13})$$

The choice of the formula for  $\beta_k$  may depend on the application and in general requires a bit of experimentation.

---

**Algorithm 3** Linear conjugate gradient algorithm

---

**Input:**  $\mathbf{x}_0$   
**Output:**  $\mathbf{x}^*$   
**Compute**  $\mathbf{r}_0$   
 $\mathbf{p}_0 \leftarrow -\mathbf{r}_0$   
**for**  $k = 0 : K_{max} - 1$  **do**  
    **Compute**  $\alpha_k$  ▷ with (C.8)  
     $\mathbf{x}_{k+1} \leftarrow \mathbf{x}_k + \alpha_k \mathbf{p}_k$   
    **Compute**  $\beta_{k+1}$  ▷ with (C.10)  
     $\mathbf{p}_{k+1} \leftarrow -\mathbf{r}_{k+1} + \beta_{k+1} \mathbf{p}_k$   
**end for**  
 $\mathbf{x}^* \leftarrow \mathbf{x}_{k_{max}}$

---

---

**Algorithm 4** Non-linear conjugate gradient algorithm

---

**Input:**  $x_0$   
**Output:**  $x^*$   
**Compute**  $\nabla f(x_0)$   
 $p_0 \leftarrow -\nabla f(x_0)$   
**for**  $k = 0 : K_{max} - 1$  **do**  
    **Compute**  $\alpha_k$  by minimizing  $f(x_k + \alpha_k p_k)$   
     $x_{k+1} \leftarrow x_k + \alpha_k p_k$   
    **Compute**  $\nabla f(x_{k+1})$   
    **Compute**  $\beta_k$  ▷ with (C.11)-(C.12)-(C.13)  
     $p_{k+1} \leftarrow -\nabla f(x_{k+1} + \beta_k p_k)$   
**end for**  
 $x^* \leftarrow x_{k_{max}}$

---

# Notation

Notation	Description
$a$	Scalar in $\mathbb{R}$ or $\mathbb{C}$
$\mathbf{E}$	Geometric vector in $\mathbb{R}^3$ or $\mathbb{C}^3$
$\hat{\mathbf{u}}$	Unit vector in $\mathbb{R}^3$ or $\mathbb{C}^3$
$\mathbf{a}$	1-D array, column vector in $\mathbb{R}^N$ or $\mathbb{C}^N$
$a_n$	$n$ -th element of the array $\mathbf{a}$
$\mathbf{A}$	2-D array, matrix in $\mathbb{R}^{N \times M}$ or $\mathbb{C}^{N \times M}$
$\mathbf{A}_{nm}$	$(n, m)$ element of the matrix $\mathbf{A}$
$a^*, \mathbf{a}^*, \mathbf{A}^*$	Conjugate
$\mathbf{a}^\top, \mathbf{A}^\top$	Transpose
$\mathbf{a}^H, \mathbf{A}^H$	Hermitian, conjugate-transpose
$\mathbf{f} \cdot \mathbf{g}$	Dot product
$\mathbf{f} \times \mathbf{g}$	Cross product
$\langle \mathbf{f}, \mathbf{g} \rangle$	Bilinear product
$\mathbf{a}^\top \mathbf{b}$	Row-column product
$\mathbf{a} \odot \mathbf{b}$	Element-wise product
$\nabla f$	Gradient
$\tilde{\nabla} f$	Complex gradient

# Bibliography

- [1] O. Quevedo-Teruel, H. Chen, A. Díaz-Rubio, G. Gok, and A. Grbic et al., «Roadmap on metasurfaces», *Journal of Optics*, vol. 21, no. 7, Jul. 2019.
- [2] E. Kuester, M. Mohamed, M. Piket-May, and C. Holloway, «Averaged transition conditions for electromagnetic fields at a metafilm», *IEEE Transactions on Antennas and Propagation*, vol. 51, no. 10, pp. 2641–2651, 2003.
- [3] F. Marzano and N. Pierdicca, *Fondamenti di antenne. Radiazione elettromagnetica e applicazioni*. Carocci, 2011.
- [4] C. A. Balanis, *Advanced Engineering Electromagnetics, 2nd Edition*. Wiley, 2012, ch. 7 - Electromagnetic Theorems and Principles.
- [5] W. Gibson, *The Method of Moments in Electromagnetics* (A Chapman & Hall book). CRC Press, Taylor & Francis Group, 2021.
- [6] S. Rao, D. Wilton, and A. Glisson, «Electromagnetic scattering by surfaces of arbitrary shape», *IEEE Transactions on Antennas and Propagation*, vol. 30, no. 3, pp. 409–418, 1982.
- [7] M. Zucchi, F. Vernì, M. Righero, and G. Vecchi, «Current based automated design of realizable metasurface antennas with arbitrary pattern constraints», *IEEE Transactions on Antennas and Propagation*, vol. 71, no. 6, pp. 4888–4902, 2023.
- [8] K. Michalski and J. Mosig, «Multilayered media green’s functions in integral equation formulations», *IEEE Transactions on Antennas and Propagation*, vol. 45, no. 3, pp. 508–519, 1997.
- [9] J. Nocedal and S. J. Wright, *Numerical Optimization*, 2e. New York, NY, USA: Springer, 2006.
- [10] R. Denysiuk, «Evolutionary multiobjective optimization: Review, algorithms, and applications», Ph.D. dissertation, 2014. [Online]. Available: [https://www.researchgate.net/publication/305409038\\_Evolutionary\\_Multiobjective\\_Optimization\\_Review\\_Algorithms\\_and\\_Applications](https://www.researchgate.net/publication/305409038_Evolutionary_Multiobjective_Optimization_Review_Algorithms_and_Applications).

- [11] R. Wildman and A. Gaynor, «11 - topology optimization for robotics applications», in *Robotic Systems and Autonomous Platforms*, S. M. Walsh and M. S. Strano, Eds., Woodhead Publishing, 2019, pp. 251–292.
- [12] M. Akbari, P. Asadi, M. Besharati Givi, and G. Khodabandehlouie, «13 - artificial neural network and optimization», in *Advances in Friction-Stir Welding and Processing*, M. K. B. Givi and P. Asadi, Eds., Woodhead Publishing, 2014, pp. 543–599.
- [13] L. Jiao, R. Shang, F. Liu, and W. Zhang, «Chapter 3 - theoretical basis of natural computation», in *Brain and Nature-Inspired Learning Computation and Recognition*, L. Jiao, R. Shang, F. Liu, and W. Zhang, Eds., Elsevier, 2020, pp. 81–95.
- [14] D. Simon, *Evolutionary Optimization Algorithms*. Wiley, 2013, ch. 20 - Multi-Objective Optimization.
- [15] P. Mergos and A. Sextos, «Multi-objective optimum selection of ground motion records with genetic algorithms», 2018.
- [16] X.-S. Yang, «Chapter 14 - multi-objective optimization», in *Nature-Inspired Optimization Algorithms*, Oxford: Elsevier, pp. 197–211.
- [17] R. Marler and J. Arora, «The weighted sum method for multi-objective optimization: New insights», *Structural and Multidisciplinary Optimization*, vol. 41, pp. 853–862, Jun. 2010.
- [18] X. Gu, G. Sun, G. Li, L. Mao, and Q. Li, «A comparative study on multiobjective reliable and robust optimization for crashworthiness design of vehicle structure», *Struct Multidisciplinary Optim*, Aug. 2014.
- [19] N. Ryu and S. Min, «Multi-objective optimization with an adaptive weight determination scheme using the concept of hyperplane: Multi-objective optimization with an adaptive weight», *International Journal for Numerical Methods in Engineering*, vol. 118, Dec. 2018.
- [20] G. Minatti, F. Caminita, M. Casaletti, and S. Maci, «Spiral leaky-wave antennas based on modulated surface impedance», *IEEE Transactions on Antennas and Propagation*, vol. 59, no. 12, pp. 4436–4444, 2011.
- [21] S. Pandi, C. A. Balanis, and C. R. Birtcher, «Design of scalar impedance holographic metasurfaces for antenna beam formation with desired polarization», *IEEE Transactions on Antennas and Propagation*, vol. 63, no. 7, pp. 3016–3024, 2015.
- [22] M. Bodehou, D. Gonzalez-Ovejero, C. Craeye, and I. Huynen, «Method of moments simulation of modulated metasurface antennas with a set of orthogonal entire-domain basis functions», *IEEE Transactions on Antennas and Propagation*, vol. 67, no. 2, pp. 1119–1130, Nov. 2018.